Revealing Star Formation Activity and Feedback Mechanisms in Nearby Merging Galaxies

道山　知成

博士（理学）

総合研究大学院大学
物理科学研究科
天文科学専攻

平成３０（２０１８）年度

Revealing Star Formation Activity and Feedback Mechanisms in Nearby Merging Galaxies

Tomonari MICHIYAMA

SOKENDAI

(The Graduate University for Advanced Studies)

January 2019

Supervisors: Daisuke Iono

Kouichiro Nakanishi & Masatoshi Imanishi

ABSTRACT

A galaxy-galaxy merger is a fundamental process for galaxy evolution since it is a common event in the universe. The ultimate question in this thesis is "what happens during a galaxy-galaxy merger". Astronomers have been studying a merger process theoretically and observationally. It is obvious that collisions affect the morphology of galaxies. Furthermore, many studies have addressed that a merger process affects activities of galaxies, i.e., triggering starburst and/or active galactic nucleus (AGN) activities. However, it remains unknown how such activities are enhanced by a galaxy-galaxy merger and subsequently affect galaxy evolution (feedback process). I approach these issues by using sub/millimeter telescopes; Atacama Submillimeter Telescope Experiment (ASTE) and Atacama Large Millimeter/submillimeter Array (ALMA). I performed a series of separate projects as follows.

1st project

At first, I investigated “global” properties of merging galaxies through survey observations. The main goal of the first project is to reveal the evolution of the merging galaxies in terms of star formation relation. Star formation relation is a global relation between properties of star formation activity (i.e., star formation rate: SFR) and material for star formation (i.e., molecular gas mass: $M_{\rm H_2}$). The relation has been studied over $\sim$50 years and still be a big issue in astronomy since the relation is essential to understand and model the galaxy evolution. Several investigations have demonstrated that there is a bimodal sequence for isolated disk galaxies and starburst galaxies; long-lasting

star formation in disk galaxies and rapid mode in starburst galaxies. This means that star formation efficiency ($SFE = SFR/M_{H_2}$) is higher in starburst galaxies than disk galaxies. My working hypothesis is that a galaxy-galaxy merger can explain the bi-modality, which means that merging galaxies fill the gap between two sequences. In order to confirm this idea, it is necessary to investigate the exact location of interacting galaxies through systematic observations along the merger sequence from early stage (before coalescence) to late stage (after coalescence) with a various SFR range. However, previous studies are biased to late stage mergers that have intense starburst activity. In my project, I conducted ASTE CO (3–2) survey observations for merging galaxies (total observation time 120 hours). I increase the number of early stage merging galaxies without intense starburst activities. I investigated the relation between the CO (3–2) luminosities ($L_{CO} \propto M_{H_2}$) and the far-infrared luminosity ($L_{FIR} \propto$ SFR) (which is a fundamental relation to determine star formation relation) in a sample of 29 early- and 31 late- stage merging galaxies and 28 nearby isolated spiral galaxies. I found that normal isolated spiral galaxies and merging galaxies have different slopes (α) in the $\log L_{CO}$ – $\log \log L_{FIR}$ plane: $\alpha \sim 0.8$ for disk galaxies and ~ 1.1 for merging galaxies. In addition, I found that the star formation efficiency (SFE$\propto L_{FIR}/L_{CO}$) gradually increases from isolated galaxies, merging galaxies, and to high-z active galaxies. My results support the idea to explain the bi-modality by a merger process.

2nd project

Second, I investigated the details of star formation activity in a merging galaxy. As shown in the first project, a galaxy collision plays an important

role for global star formation activity in galaxies. The goal of the second project is to answer the question of "Where starbursts are triggered in merging galaxies?". In this project, I use both optical integral field units (MUSE mounted on Very Large Telescope) to obtain Hα and Hβ image which can trace diffuse disk-wide starbursts and ALMA to obtain H40α and H42α image which can trace extremely dusty nuclear starbursts. As a kickoff study, I selected one merging galaxy NGC 3256 that consists of two galaxies; one is the northern starburst galaxy and the other is the southern dusty galaxy hosting a low luminosity AGN. First, I use optical integral field units (MUSE mounted on Very Large Telescope) and obtain maps of recombination lines (i.e., Hα and Hβ). I investigate the spatial distribution and properties of star forming regions. I found many star forming blobs outside of nuclear regions, and these regions are categorized as starburst in terms of surface density of SFR and $M_{\rm H_2}$. However, it is difficult to investigate star formation activities in dusty regions by using optical observations. Instead, I use mm/sub-mm recombination lines to investigate "true" star formation activity without dust extinction. I observed H40α and H42α in 3mm resolution by using ALMA. I found that there is a star forming region at the southern nucleus where optical recombination lines are undetected due to strong dust extinction ($A_{\rm V} \sim 18$). The missed SFR in the southern dusty star forming region is 12% of total SFR expected from extinction corrected Hβ map. Including both VLT and ALMA observation, I found that the contribution of SFR from nuclear and spatially extended starburst is $\sim$ 27% and 73% respectively. Therefore, I conclude that disk-wide starbursts are more important than dusty nuclear starbursts in NGC 3256.

3rd project

Finally, I describe the feedback process. Starburst and AGN feedback occur in the form of galactic-scale outflows. The goal of the third project is to answer the question of "What kind of structure and properties do molecular outflows have?". Recently, a number of studies have reported identifications of molecular outflows in CO observations by using ALMA. They measured the mass and velocity of outflows. However, in order to include the feedback process into galaxy evolution model, the other properties of outflows (e.g., structure and physical and chemical properties) should be investigated. The originality of the third project is that I use multi-lines (e.g., CO, HCN and HCO^+) to characterize the structure, density and temperature, and chemistry of the outflows. NGC 3256 is an ideal target since two low J ($J < 3$) CO outflows from the two nuclei (starburst and low-luminosity AGN) have already been reported. Two different types of outflow can be simultaneously investigated. I detected the high-density gas traced in HCN (1–0) and HCO^+(1–0) in AGN triggered southern outflow. On the other hand, the same lines were undetected in the northern outflow triggered by starburst. In terms of the HCO^+(1–0)/CO(1–0) (i.e. dense gas fraction) and the CO(3–2)/CO(1–0) line ratio are larger in the outflow (0.20 ± 0.04 and 1.3 ± 0.2, respectively) than in the nucleus (0.08 ± 0.01, 0.7 ± 0.1, respectively). This means that the outflowing gas has a higher density and temperature compared to the nucleus. It is difficult to understand these results under an assumption of simple mass transportation (i.e., negative feedback). In addition, by investigating these line ratios for each velocity component in the outflow, I found that the dense gas fraction increases and the CO (3–2)/CO (1–0) line ratio decreases toward the largest velocity offset. This means that dense gas tracers and CO lines

trace different part of the outflow; i.e., dense clumps traced by HCN and HCO^+ and diffuse gas traced by CO lines. Such clumps with large velocity offset are detected by high resolution (0.2") follow up CO (2–1) observation. One possible scenario to produce such a two-phase outflow is an interaction between the jet and the interstellar medium (ISM), which is seen in active AGNs (e.g., M51, IC5013).

[Conclusions] Through these three projects, I found mainly two important phenomena to answer the question of "what happens during a galaxy-galaxy merger" as follows.

1. **"nuclear starburst" and "disk wide starbursts" in merging galaxies:** The classical idea of merger induced star formation activity is nuclear starbursts taking place in the central region ($<$ 1 kpc) due to global gas inflow in the late stage. On the other hand, some theoretical models predict disk-wide starbursts ($>$1 kpc) due to the fragmentation of dense gas in the early stage. The enhancement of SFE in merging galaxies seen in our ASTE survey supports the latter case. In addition, a case study of NGC 3256 shows the evidence of the larger contribution of disk-wide starburst than dusty nuclear starburst. The key of my project is that both diffuse disk-wide starbursts and dusty nuclear starbursts are investigated in a consistent manner by using hydrogen recombination lines by optical (MUSE/VLT) and mm wavelength (ALMA). In the future, it is necessary to investigate various types of merging galaxies (e.g., early/late stage, major/minor, wet/dry) with the same method in order to explain the mechanism of enhancement of star formation activity during a merger process. For example, more advanced merging galaxies are expected to have larger contribution of dusty nuclear starbursts than disk-wide star-

bursts.

2. **dense clumps in a molecular outflow:** A case study of NGC 3256 shows the presence of dense clumps in the AGN triggered outflow. This has not been predicted by the typical merger scenario, where gas is simply expelled without any actions (negative feedback). The complex physical mechanisms are necessary to explain the formation of dense clumps in outflows, i.e., jet and ISM interaction by strong AGN feedback. Such clumps in the outflows can possibly become the sites of future star formation ("positive feedback"), affecting the long-term evolution of the host galaxy. However, the expected SFR derived from total dense gas mass in the outflow is not as high as the SFR of host galaxy. The conclusion from this study is that while the degree of star formation is likely small, the existence of "positive feedback" is possible and it is not completely ruled out. As a next step, it is necessary to investigate how outflows affect the star formation activity not only for high-velocity gas but also for the gas in the disk.

[Future prospects] The observational data presented in this thesis provides evidences of previously expected "disk-wide starbursts" and the new idea of "clumpy dense outflows" in merging galaxies, particularly in NGC 3256. The important next step is to expand our observation from individual case studies to a statistically significant sample that includes a wide range of merger stages, star formation rates, and nuclear properties.

ACKNOWLEDGEMENTS

I have many people to thank. First of all, I would like to show my deepest appreciation for my supervisor, Daisuke Iono. He provided me this wonderful research life at SOKENDAI and NAOJ. He has supported me for all my works to write this thesis. His advices for proposals, observations, data analysis and discussion is greatly helpful for me. This thesis had not been achieved without his help. I would like to thank to Kouichiro Nakanishi, Masatoshi Imanishi, and Tadayuki Kodama, who worked with me as a second supervisor. Their advices are always very useful for my works.

I greatly thank Alberto Bolatto, Susanne Aalto, and Eva Schinnerer, who hosted me in the university of Maryland, USA; Onsala observatory, Sweden; Max Planck Institute for Astronomy, Germany. I had a wonderful research life in their institute.

I would like to thank my colleagues, Min Yun, Kazimierz Sliwa, Junko Ueda, Takuji Yamashita, Toshiki Saito, Yuichi Matsuda, Bunyo Hatsukade, Hiroyuki Kaneko, Kenichi Kikuchi, Shinya Komugi, and Takayuki Muto. They provided me very important comments for my papers. I would like to thank Kazuyuki Muraoka and Tomoka Tosaki for kindly providing their published data.

I dare to thank SOKENDAI staffs; Saku Tsuneta, Masahiko Hayashi, Takashi Sekii, Kohji Tomisaka, Yutaka Okuda, Kaori Kano, Mihiro Fujimori, Mizuho Inoue, and Yumiko Omura. They provided me a very nice environment to study. I got great financial supports from SOKENDAI. I hope sincerely to keep abundant SOKENDAI funds for graduate students.

I would like to thank the members of ALMA, ASTE, and Nobeyama, espe-

cially, Satoru Iguchi, Seiichi Sakamoto, Misato Fukagawa, and Alvaro Gonzalez, and Tetsuo Hasegawa.

I am greatly thankful to the scientists, post-docs and grad students at SOKENDAI and NAOJ. I can not list your names because it must be too long. Especially I would like to thank Ken-ichi Tadaki, Andrea Sliva, Yu-ting Wu, Dieu Nguyen, Masumi Shimojo, Hiroshi Nagai, Daniel Espada, Tomofumi Umemoto, Rie Miura, Patricio Sanhueza, Kazuya Saigo, Joten Okamoto, Yusuke Miyamoto, Natsuko Izumi, Yuta Kato, Kazuki Sato, Hiroyuki Ishikawa, Takafumi Tsukui, Jinshi Sai, and Masayuki Yamaguchi. I had wonderful research life with them. I specially thank to, Kanako Momota, Reni Takagi, Momoka Ariyasu, Shiori Tamai and Ayaka Sasaki. They cheered me up anytime.

Finally I would like to thank to my family, Yasuo Michiyama, Mieko Michiyama and Akina Michiyama for spiritual and financial supports during my student life.

TABLE OF CONTENTS

Page

LIST OF FIGURES

FIGURE Page

LIST OF TABLES

TABLE Page

1 | INTRODUCTION

The earth travels around the sun. Thousands of stars like the sun are visible in the night sky by our eyes. Our galaxy contains $\sim$ 200 billions of stars, and the sun is merely one of them. In addition, there are numerous galaxies outside of our galaxy, and the number is said to be $>$ 100 billions. A galaxy is the most important component of the Universe. Therefore, proper understanding of the process of galaxy formation and evolution is essential for disentagling the history of the universe.

Stars are the fundamental unit of the galaxy. Galaxies also have interstellar medium (ISM) containing gas and dust. In addition, galaxies have dark matter, which are invisible and cannot be observed directly. A galaxy is not an eternal system in a cosmic timescale, and all galaxies have characteristics like human beings; e.g., variety of sizes, stellar populations, masses, and morphologies. Astronomers have been trying to reveal their nature, structure, and origin. In this thesis, I challenge the mystery of galaxy evolution.

1.1 Historical Background about Galaxy-galaxy Merger

Edwin Hubble proposed a classification system for nebulae (both galactic and extragalactic) from 1922 to 1926, and produced the diagram called "Hubble sequence" of galaxy morphological types (Hubble , 1926) (Figure 1.1). In this thesis, I focus on the irregular galaxies that do not fit into the Hubble sequence. One of the most common mechanisms to produce such irregular galaxies is a gravitational interaction between galaxy and galaxy. Assuming that galaxies are widely scattered in the universe, collisions between galaxies are unlikely because the spatial density of galaxies is too low. However, galaxies are often in a cluster and the space between

galaxies is much smaller. Erik Holmberg proceeded the first theoretical approach to reconstruct the disturbed morphology at a close encounter between two nebular (Holmberg , 1941). He used 37 light-bulbs as a laboratory model and found that the tidal deformations cause an increase in the attraction between the two objects, i.e., after the passage.

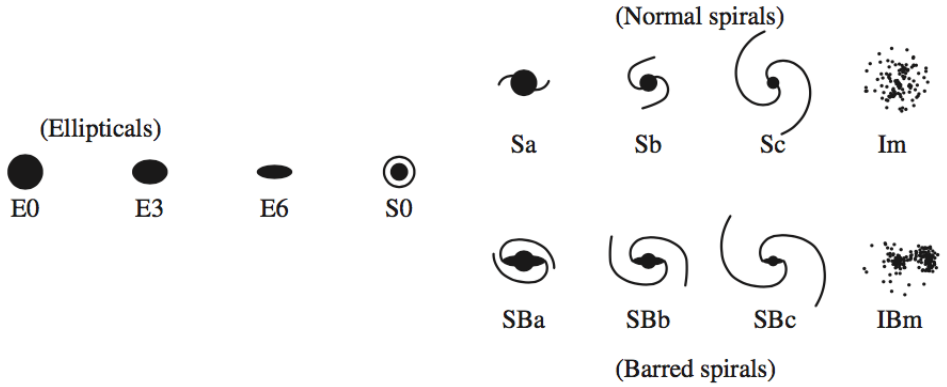

Figure 1.1 A schematic of the morphological classification scheme, Hubble sequence. This figure is reproduced from Mo H. van den Bosch F. C. and White S. 2010, "Galaxy Formation and Evolution" (Mo et al. , 2010)

Vorontsov-Velyaminov published the catalogue of interacting galaxies called "VV catalog" (THE ATLAS AND CATALOGUE OF INTERACTING GALAXIES) in 1959 (Vorontsov-Velyaminov , 1959). Starting with VV catalog, catalogs of galaxies containing many interacting galaxies and galaxies experiencing/experienced interaction and merging were published; e.g., Arp catalog (Arp , 1966) (ATLAS OF PECULIAR GALAXIES), CGCG catalog (Zwicky et al. , 1968) (Catalogue of Galaxies and of Clusters of Galaxies), AM catalog (Arp & Madore , 1987) (Catalogue of Southern Peculiar Galaxies and Associations), ESO catalog (The ES-

O/Uppsala Survey of the ESO (B) Atlas of the Southern Sky), and Mrk catalog (1967-81, 1986, 1989). Figure 1.2 shows the images of the interacting galaxies obtained by Hubble Space Telescope.

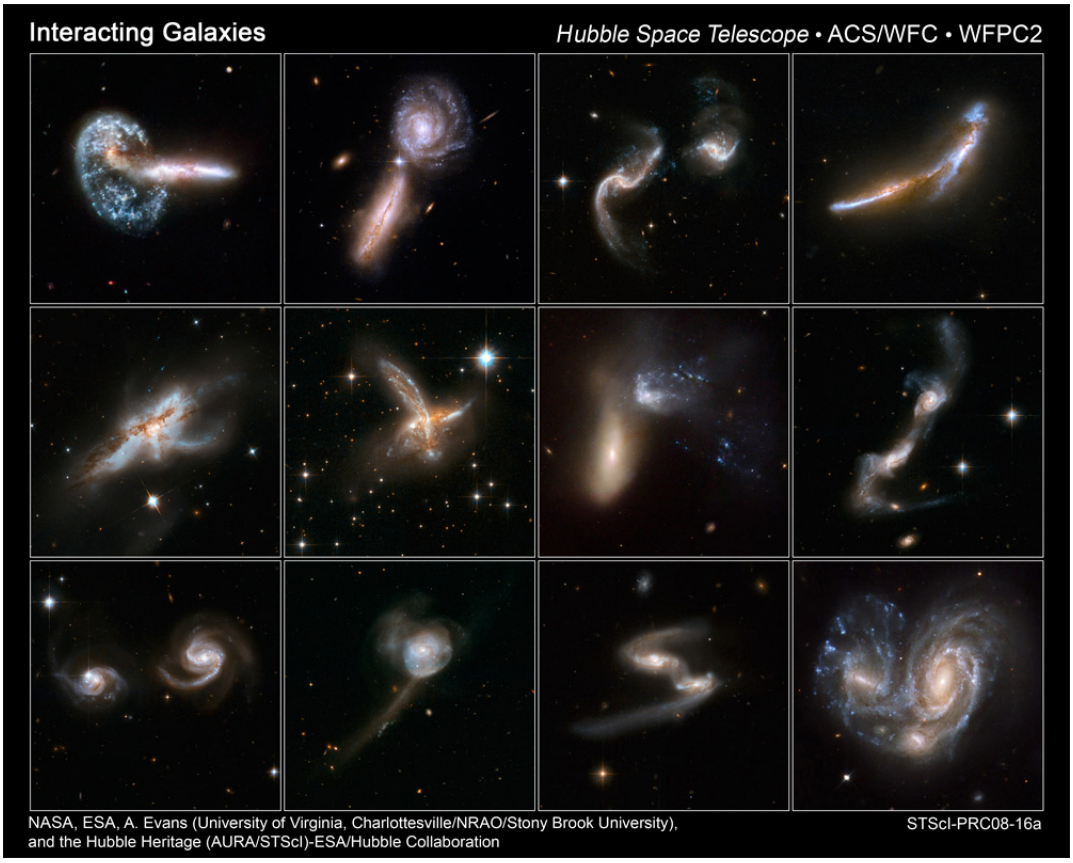

Figure 1.2 The peculiar morphology of interacting galaxies from Hubble Space Telescope observations. ©NASA, ESA, A. Evans (University of Virginia, Charlottesville/NRAO/Stony Brook University), and the Hubble Heritage Team (STScI/AURA)-ESA/Hubble Collaboration

To coincide with releases of the merging galaxy catalogs, Toomre and others carried theoretical works on the dynamical interaction between galaxies expecting the tidal effects in colliding disc systems. One of the finest papers is Toomre &

Toomre (1972). They reproduced the long "bridges" and "tails" seen in the interacting galaxies, and suggest that elliptical galaxies may be the product of past mergers. In particular, they reproduce the orbits and outer shapes of four specific interacting pairs: Arp 295, M51 + NGC 5195, NGC 4676, and NGC 4038/9 (Figure 1.3). Numerous theoretical works including N-body simulations were performed to explain the peculiar morphology of interacting galaxies in the 1970s. The results are reviewed by White (1978).

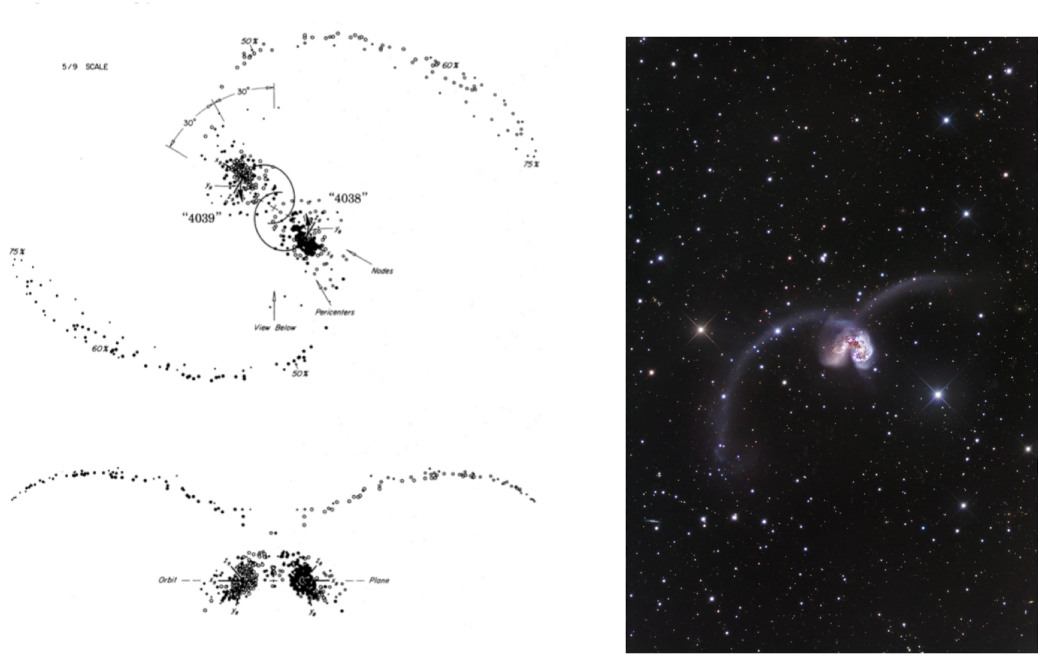

Figure 1.3 (left) The model to reproduce the stellar distribution of Antennae galaxy (NGC 4038/9) based on N-body simulation (Toomre & Toomre , 1972). This figure is reproduced from Toomre A. & Toomre J. 1972, ApJ, 178 623-666. (right) The RGB images of Antennae galaxy obtained by Hubble Space Telescope. (Credit: ESA/Hubble & NASA)

In addition to the morphological evolution, Toomre & Toomre (1972) argue

that an interaction can have a profound impact to the activity in galaxies. One of the most simple benchmarks for activity of galaxies is "how many solar mass stars a galaxy form in one year (star formation rate SFR [$M_\odot$ yr^{-1}])". Star formation in galaxies is a fundamental process that dictates the future evolution and morphology of galaxies. Using *UVB* colors of galaxies as an indicator of the history of star formation, Larson & Tinsley (1978) show an evidence that "bursts" of star formation (starburst) are often caused by the effects of close tidal interactions or collisions between galaxies. A "starburst galaxy" is a galaxy powered by bursts of massive star formation. For example, Milky Way has the global SFR of a few $M_\odot$ yr^{-1} and star formation rate per unit area ($\Sigma_{\rm SFR}$) of a $\sim 10^{-2.5}$ $M_\odot$ yr^{-1} kpc^{-2} (Kennicutt & Evans , 2012). On the other hand, a starburst galaxy shows global SFR of 10-1000 M$_\odot$ yr^{-1} and $\Sigma_{\rm SFR}$ of $>$ 10^{-1} $M_\odot$ yr^{-1} kpc^{-2} (Heckman , 2001). This means that a starburst galaxy would use up the available gas in $\sim$ 1 Myr and this time scale is much smaller than the life time of the typical galaxies $\sim$ 1 Gyr. Moreover, Condon & Dressel (1978) conducted 21-cm radio continuum observation and found that radio continuum fluxes in the interacting galaxies were a factor of 2-3 enhanced compared to isolated spirals. Condon et al. (1982) interpreted this as an evidence for powerful nuclear starbursts triggered by galaxy interactions.

Infrared observation is one of the keys to investigate the star formation activity in merging galaxies since they emit the bulk of their energy as dust reprocessed thermal IR emission powered by embedded star formation. Such IR-luminous galaxies were first discovered by Rieke & Low (1972). The revolutionary telescope, "Infrared Astronomical Satellite (*IRAS*)", launched on 25 January 1983 (Neugebauer et al. , 1984), which was the first space telescope to conduct the all sky survey in infrared. *IRAS* has sufficient sensitivity to detect numerous extragalactic sources in infrared, and produced *IRAS* Point Source Catalog containing $\sim$ 20,000 galax-

ies. Investigations of the optical images of *IRAS* galaxies show that the fraction of objects that are interacting/merging systems appears to increase systematically with increasing infrared luminosity. For example, Sanders et al. (1988); Melnick & Mirabel (1990) show that the fraction of interacting/merging galaxies are ~ 10 % at infrared luminosity $L_{\rm IR}$ of $10^{10.5-11}$ $L_{\odot}$ and ~ 100 % at $> 10^{12}$ $L_{\odot}$. Galaxies hosting such a large luminosity at infrared are called luminous infrared galaxies (LIRGs; 10^{11} $L_{\odot}$ $\leq$ $L_{\rm IR}$ $<$ 10^{12} $L_{\odot}$) and ultra luminous infrared galaxies (ULIRGs; 10^{12} $L_{\odot}$ $\leq$ $L_{\rm IR}$ $<$ 10^{13} $L_{\odot}$). In addition, sub-millimeter telescopes have been rapidly developed since the 1980s (e.g., 12 m NRAO). Mm/sub-millimeter telescopes enable us to investigate the properties of molecular gas in the merging galaxies. Main observational discovery was high concentrations of cold molecular gas in the central regions of some mergers. Sanders & Mirabel (1996) reviewed the studies related to millimeter observations of U/LIRGs. The main conclusion from *IRAS* and sub-mm observations is that strong interactions and gas-rich mergers are responsible for the great majority of U/LIRGs. Subsequently, the merger scenario as the origin of U/LIRGs has been developed by observations and theoretical modelings (e.g., Mihos , 1999; Cui et al. , 2001; Murphy et al. , 2001; Veilleux et al. , 2002), in which the interaction triggers combination of starburst and AGN activity.

In the 1990s, theoretical models of galaxy-galaxy interaction had been successful to explain the mechanism enhancing the star formation. The main difference from the simulations in the 1970s is that they developed new dynamical models with gas, stars, and a live dark matter halo during the interaction. For example, according to the model by Barnes & Hernquist (1992), the angular momentum of gas is transferred to stars due to dynamical friction, allowing the gas to flow rapidly towards the nuclei of merging galaxies. Such dynamical models are widely accepted and become the base of the current simulations, including feedback mechanisms re-

lated to activities of starburst and active galactic nuclei (AGN) (e.g., Hopkins et al. , 2006) (see also Section 1.3.3).

On the observational side, the rapid development of telescopes in the 1990s enabled us to observe numerous numbers of galaxies including distant (high redshift) galaxies. For example, the Sloan Digital Sky Survey (SDSS) statistically characterize the activities of the merging galaxies (Ellison et al. (2008) and following series for "Galaxy pairs in the SDSS") in local Universe (redshift up to z$\sim$0.05). In the rest-frame UV, it is found that distant star forming galaxies show irregular morphologies (e.g., Elmegreen & Elmegreen , 2005). In addition, the redshift evolution of merger fraction has been investigated by various groups (e.g., Bridge et al. , 2010; Steinborn et al. , 2018) These studies show that merger fraction is higher in the higher redshift. This suggests that galaxy-galaxy interaction plays an important role in terms of the galaxy evolution in cosmological timescale.

1.2 Empirical star formation relation

1.2.1 Kennicutt-Schmidt law

In order to understand and model the galaxy evolution, we need simple mathematical formula for star formation in galaxies. The most widely applied formula is the power law relation between the observable surface density of gas ($\Sigma_{\rm gas}$) and star formation rate ($\Sigma_{\rm SFR}$) originally introduced by Schmidt (1959).

$$\Sigma_{\rm SFR} = A\Sigma_{\rm gas}^{N} \tag{1.1}$$

Dozens of studies had investigated the relation between $\Sigma_{\rm SFR}$ and $\Sigma_{\rm gas}$. Kennicutt (1983) summarized the measurements of Hα, HI, and CO distribution, and found a Schmidt law index of 1.4 ± 0.15 over several orders of magnitude in SFR and gas

density (called Kennicutt-Schmidt law). This relation has been used in numerical N-body SPH simulations to convert gas density to SFR (e.g., Springel & Hernquist , 2003).

In the 2000's, targeted surveys with space telescopes *Galaxy Evolution Explore* (*GALEX*; NGS) (Gil de Paz et al. , 2007) in UV and *Spitzer*; SINGS (Kennicutt et al. , 2003) in infrared enable us to investigate the spatial distributions of star formation activity in galaxies. In addition, the developments of radio and sub-mm telescopes enabled us to investigate spatial distributions of the atomic gas and molecular gas in galaxies (BIMA SONG; Helfer et al. 2003, HERACLES; Leroy et al. 2008, and THINGS; Walter et al. 2008). Combining these observations, Bigiel et al. (2008) investigated the properties of molecular associations at sub-kpc resolution in 18 nearby galaxies and expanded the Kennicutt-Schmidt law from scales that include the entire galaxy to local star forming regions. In addition, the Kennicutt-Schmidt law was expanded to high redshift sources (e.g., Solomon & Vanden Bout , 2005). Genzel et al. (2010) investigated the relation including galaxies at $z \sim 1-3$. They found that gas-rich major mergers at both low and high-z produce 4-10 times more FIR luminosity at a given gas mass. After including the galaxies which have high luminosity in submillimeter (submillimeter galaxies; SMGs), Daddi et al. (2010) suggest two different SF regimes: a long-lasting mode for disk galaxies and a more rapid mode for U/LIRGs and SMGs both at low and high redshift. Figure **??** shows the typical examples of the empirical star formation relations. Finally, the current issue is to reveal the background physical mechanisms in order to explain the empirical Kennicut-Schmidt relation (e.g., Tan , 2000; Li et al. , 2005; Onodera et al. , 2010). For example, Krumholz & McKee (2005) explain the Kennicutt-Schmidt relation using turbulence regulated model for environments ranging from normal galactic disks to starbursts and U/LIRGs. Star formation relation is investigated by

using lower-density tracers such as CO (1–0), higher excitation CO transitions, and high-density gas tracers such as HCN and HCO^+. For example, Gao & Solomon (2004) investigate the relation between integrated SFRs and dense molecular gas mass for normal and starburst galaxies. They found a linear relationship, implying a strong coupling between dense gas mass and star formation activity. Additional information about star formation relation (e.g., star formation rate diagnostics, star formation process, molecular and atomic gas tracer) is reviewed by Kennicutt & Evans (2012).

1.2.2 Kennicutt-Schmidt relation for merging galaxies

I mentioned that several investigations have demonstrated that there is bi-modal sequence for isolated disk galaxies and starburst galaxies (e.g., Daddi et al. , 2010). One idea is that galaxy-galaxy merger can explain the bi-modality. This means that SFE gradually increases from early to late stage and merging galaxies fill the gap between two sequences. This is predicted in recent theoretical merger models (e.g., Teyssier et al. , 2010; Bournaud , 2011). In their model, one important phenomenon is global gas inflow which increases the average gas density and the SFR (nuclear starburst). This is a standard process and occurs at a late stage of merger process (after coalescence) effectively. In addition, the gist of their argument is that fragmentation of high-dispersion gas outside the nuclear region due to local shock (which triggers extended starburst) is equally important especially in the early phase (before coalescence). In addition, some other numerical simulations of merging galaxies provided by Powell et al. (2013) have shown that all merging galaxies (not only starburst systems like the Antennae galaxy but also lesser degree ones) are in between the disk sequence and the starburst sequence. The observational confirmation of enhancement of SFE in merging galaxies have still being

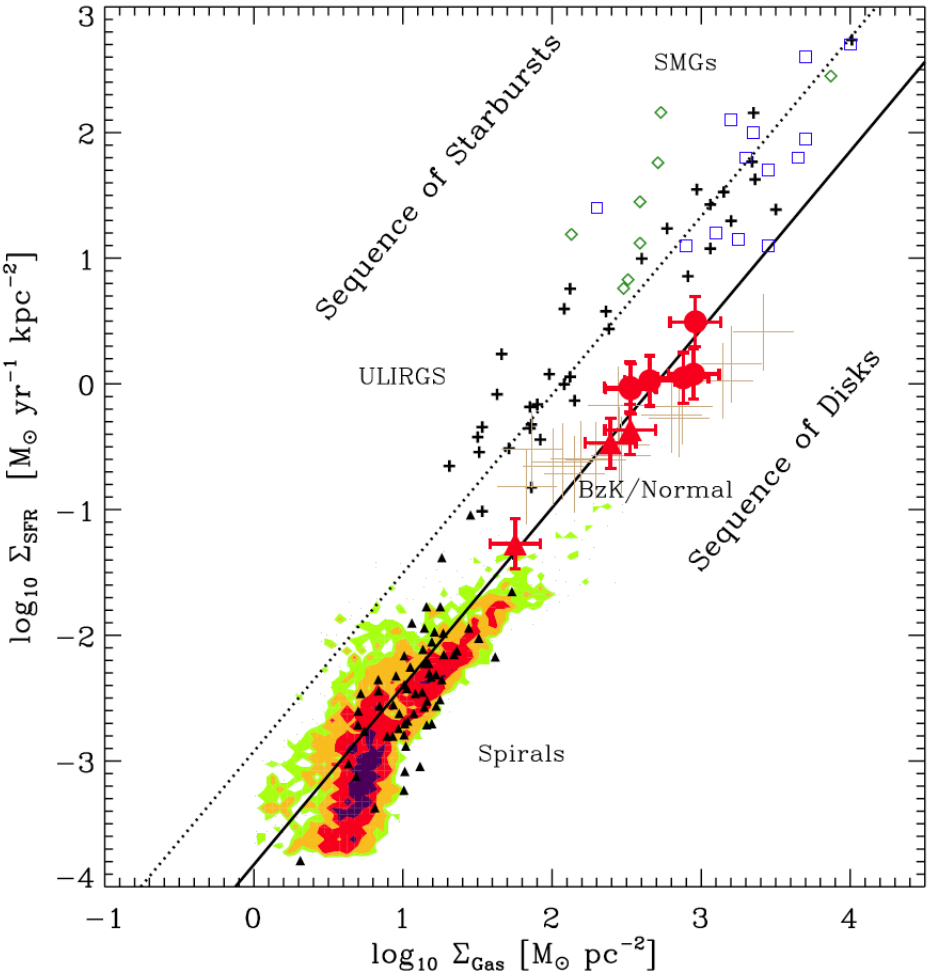

Figure 1.4 The empirical star formation relation called Kennicut-Schmidt relation. Daddi et al. (2010) show that there are two sequences in this relation. One is disk sequence for normal galaxies and the other is starburst sequence for U/LIRGs and SMGs. The detail of the sample selection and galaxies plotted in this figure is explained in Daddi et al. (2010). This figure is reproduced from Daddi et al., 2010, ApJ, 713 686-707.

investigated in recent works (Cheng et al. , 2018; Violino et al. , 2018; Pan et al. , 2018).

1.3 Feedback mechanism during galaxy and galaxy interaction

1.3.1 Galactic Wind

Finally, I describe the feedback process. The lexical meaning of the "feedback mechanism" is "mechanism by which the products of a process can act as regulators of that process". If the regulators activate the process, the mechanism works as "positive feedback", and opposite is "negative feedback". One of the dominant feedback mechanisms in galaxy formation and evolution is galactic wind, which is the gas explosion in galaxies (for review, Veilleux et al. , 2005). For example, when the galactic wind is triggered by starburst and galactic wind regulates the star formation activity, such phenomenon is reffered as negative feedback.

The first observational evidence of a galactic wind was reported by Lynds & Sandage (1963) at the center of M 82. A multi-wavelength approach is necessary to understand complex wind phenomena with various gas phase; optical and UV line emissions (e.g., Heckman et al. , 1990) and blue-shifted absorption (e.g., Heckman et al. , 2000), extended emission in soft X rays (e.g., Read et al. , 1997), and at radio wavelength (e.g., Hummel et al. , 1991). However, reviewing all the properties of galactic wind is beyond the aim of this thesis, and I focus on the molecular part of the galactic wind especially observed by molecular emission lines (molecular outflow) (e.g., CO, see Section 1.3.2).

The key question is what triggers such molecular outflows. This is broadly divided into two mechanisms; starburst or AGN driven. I describe the basic properties for both mechanisms following Veilleux et al. (2005).

[starburst driven] Large collections of both supernova explosions and massive

stellar winds can be the sources of galactic scale molecular outflows. By using the starburst model (e.g., *starburst99*), the mass-loss rate ($\dot{M}_*$ [$M_\odot$ yr^{-1}]) can be scaled with SFR,

$$\frac{\dot{M}_*}{M_\odot \text{ yr}^{-1}} = 0.26 \, \frac{SFR}{M_\odot \text{yr}^{-1}} \tag{1.2}$$

and the corresponding kinetic power is

$$\frac{\dot{E}_*}{\text{erg s}^{-1}} = 7.0 \times 10^{41} \frac{SFR}{M_\odot \text{yr}^{-1}}. \tag{1.3}$$

[AGN driven] The super massive black hole activity at the galactic center can also drive some galactic scale outflow by accretion. Through several processes, huge amounts of energy is released during accretion as outflows. In simple formulae, the mechanical luminosity due to mass accretion can be described as

$$\frac{\dot{E}_*}{L_\odot} \simeq 10^{11} (\epsilon/0.01) \frac{\dot{M}_{\rm acc}}{M_\odot \text{yr}^{-1}} \tag{1.4}$$

where $\dot{M}_{\rm acc}[M_\odot \text{yr}^{-1}]$ is the mass accretion rate and ϵ is the energy conversion efficiency. For example, the mass accretion rate is $\dot{M}_{\rm acc} \lesssim 0.001 \; M_\odot \text{yr}^{-1}$ for low-luminosity AGNs, $\dot{M}_{\rm acc} \sim 1 \; M_\odot \text{yr}^{-1}$ for Seyfert galaxies, and $\dot{M}_{\rm acc} \sim 100 \; M_\odot \text{yr}^{-1}$ for quasars. There are some processes related to the AGN driven outflow, and the formulation is not easy. For instance, radiation in luminous AGNs or quasars can push the surrounding gas (e.g., via electron scattering), and radiative cooling also affects the dynamics of the gas. Finally, magnetic fields in accretion disk power the collimating outflow associated with relativistic jets in powerful radio-loud galaxies (e.g., Zensus , 1997).

Various types of feedback mechanisms are suggested. One is radio-mode feedback. If jets heat the ISM and prevent the fragmentation, it is a negative feedback

(e.g., McNamara & Nulsen , 2007). On the other hand, if jets create shockwaves that facilitate the fragmentation, it is a positive feedback (e.g., Gaibler et al. , 2012). The other is quasar-mode feedback. If powerful outflows remove fuel for star formation from the galaxy, it is a negative feedback (e.g., Di Matteo et al. , 2005). On the other hand, if powerful outflows compress gas and induce star formation, it is a positive feedback (e.g., Zubovas & Nayakshin , 2014).

1.3.2 Molecular Outflows

Molecular gas outflows affect the amount of cold gas for star formation and black hole accretion. For example, in order to explain the observed mass of the massive elliptical galaxies in current Universe (Baldry et al. , 2004), negative feedback by molecular gas outflow is important to prevent the overgrowing of the galaxies. Molecular outflows also play an important role to explain the correlation between black hole mass and bulge properties (co-evolution between black hole and galaxy) (e.g., Magorrian et al. , 1998). Molecular outflows have been discovered in local starburst galaxies, such as NGC 253 (Sakamoto et al. , 2006; Bolatto et al. , 2013a; Krips et al. , 2016; Walter et al. , 2017), M 82 (Walter et al. , 2002; Weiß et al. , 2005; Veilleux et al. , 2009; Salas et al. , 2014; Chisholm & Matsushita , 2016), NGC 3628 (Tsai et al. , 2012), NGC 2146 (Tsai et al. , 2009; Kreckel et al. , 2014), and NGC 1808 (Salak et al. , 2016), and AGN host galaxies, such as NGC 1068 (Krips et al. , 2011; García-Burillo et al. , 2015; Lin et al. , 2016), IC 5063 (Morganti et al. , 2013; Tadhunter et al. , 2014; Morganti et al. , 2015; Dasyra et al. , 2015; Dasyra et al. , 2016) M 51 (Matsushita et al. , 2007; Querejeta et al. , 2016), and Circinus (Zschaechner et al. , 2016). Since both starbursts and AGNs can be triggered during mergers (e.g., Hopkins et al. , 2006; Narayanan et al. , 2008; Debuhr et al. , 2012; Hayward et al. , 2014), nearby merging galaxies are

ideal laboratories to observationally investigate these phenomena (e.g., Feruglio et al. , 2010; Cicone et al. , 2014; Fiore et al. , 2017; Pereira-Santaella et al. , 2018). Molecular outflows have been detected in several merging galaxies, such as Mrk 231 (Feruglio et al. , 2010; Cicone et al. , 2012; González-Alfonso et al. , 2014; Aalto et al. , 2015; Feruglio et al. , 2015; Lindberg et al. , 2016), NGC 6240 (Feruglio et al. , 2013; Saito et al. , 2018), Arp 220 (Sakamoto et al. , 2009; Barcos-Muñoz et al. , 2018), and NGC 1614 (García-Burillo et al. , 2015; Saito et al. , 2016). These observations show that molecular outflows are not rare during galaxy merger. Cicone et al. (2014); Pereira-Santaella et al. (2018) investigate the energy of outflows in several galaxies, and they found that AGN is important to produce massive outflows and pure starburst activities are not enough to completely quench the nuclear starbursts. Observational investigations of molecular outflows have just been developed and this is a hot topic related to galaxy evolution.

1.3.3 Theoretical merger model including feedback

One of the current issues of theoretical models for galaxy-galaxy merger is how feedbacks from starburst and AGN affect the merger evolution. Springel et al. (2005) described techniques to incorporate feedback mechanisms from both the massive stars and black hole accretions into simulations for merging galaxies. Cox et al. (2006); Cox et al. (2008) theoretically investigate the effect of stellar feedback for the merger driven star formation. However, as observations suggest (Cicone et al. , 2014; Pereira-Santaella et al. , 2018), AGN also plays an important role as a feedback mechanism. Newton & Kay (2013) demonstrated that AGN suppresses star formation more efficiently in galaxy mergers than in isolated galaxies. Recently Park et al. (2017) find that the effect of AGNs on star formation is larger in major mergers than in minor mergers. Theoretical merger model including feed-

back is still under development, and the observational evidences of outflows should help the development of theoretical models.

1.4 Current understanding of galaxy merger

Finally, I summarize the curren understandings of the physics that occur during galaxy-galaxy merger (Figure 1.5). I follow Hopkins et al. (2008) as an outline of the typical growth of a galaxy during a gas rich major merger. At first, without gravitational interaction, isolated disks evolve secularly. Once the two galaxies interact, star formation and black hole accretion are enhanced even though the effect is weak. At this stage, the distinct double nuclei can be observationally identified (early stage). During the final coalescence of two galaxies, intense starbursts are triggered by massive inflows (e.g., Iono et al. , 2004) and observed as U/LIRGs and/or SMGs. The rapid mass accretion to the central black hole also enhances AGN. Most of the gas is consumed due to starburst activity, eventually, supernovae and AGN feedback blow out the residual gas (e.g., Veilleux et al. , 2005). At this stage, the merged galaxy is observed as dust-reddened object (late stage). Finally, the starburst and AGN activity decline due to depletion of gas and the remaining galaxy becomes a quiescent elliptical galaxy (remnant).

It is necessary to understand that the model introduced here is just one possible explanation and the models are continuously being improved. There are important parameters to understand a merger process in the context of galaxy evolution; e.g., masses of galaxies, mass ratio (major/minor merger), gas fractions (wet/dry merger), and environment. For example, van Dokkum (2005) show that elliptical galaxies in local universe were assembled at low redshift through mergers of gas-poor and bulge-dominated systems. Tidal fly-bys of minor components also affects the morphology and GMC properties of the galaxies (Pettitt et al. , 2016, 2017;

Pettitt & Wadsley , 2018; Pettitt et al. , 2018). In addition, the future of merging galaxies is being investigated; i.e., whether merger remnant become elliptical or disk galaxy (Ueda et al. , 2014). In this thesis, I focus on the gas-rich major mergers for simplicity. However, we need to keep in mind that it is necessary to investigate both "different stage of the merger process" and "different merger parameter". A large number of merging galaxies should be selected in a different way in order to understand the importance of galaxy mergers to galaxy assembly, star formation, bulge formation, and supermassive black hole growth.

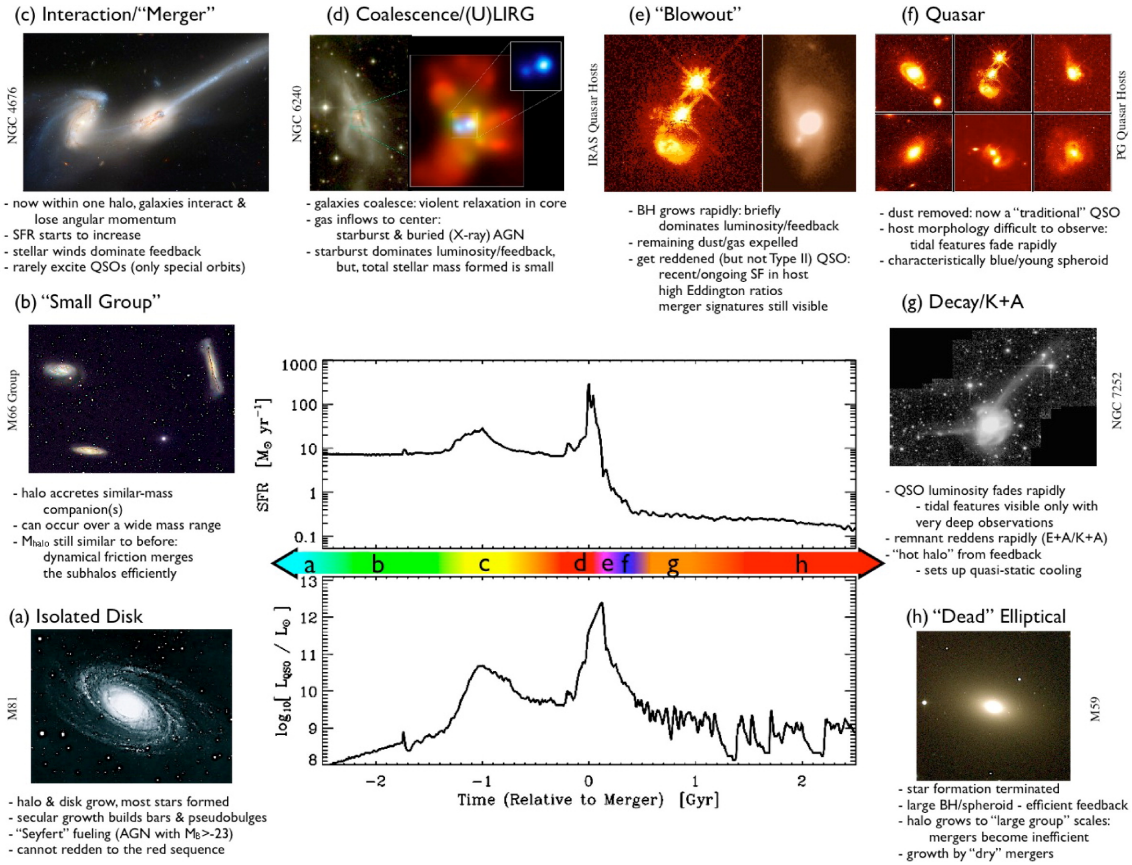

Figure 1.5 The outline of the typical growth of a galaxy during a gas rich major merger (Hopkins et al. , 2008). The central panel shows that star formation activity is enhanced by a merger process and SFR has peak when two galaxies are merged into one galaxy. The enhanced star formation activities rapidly decrease due to massive gas outflow. This figure is reproduced from Hopkins et al. 2008, ApJS, 175, 356.

1.5 This thesis

I introduced the importance of studying a galaxy-galaxy merger. There are mainly two strategies to observationally investigate merging galaxies. One is to investigate the "global" properties through the observations of a statistically significant sample of merging galaxies. However, the information obtained from global properties is limited, and it is difficult to elicit complex phenomena during a merger process. The other strategy is to investigate spatially resolved properties of a smaller sample of merging galaxies. While lacking statistical robustness, individual processes can be studied in more detail. In this thesis, I adopt both strategies and address three key questions, as follows.

- **Is star formation relation universal between normal galaxies and mergers? (Chapter 2)**

  At first, I investigated “global” properties of merging galaxies through our own survey observation. The main goal of the first project is to reveal the evolution of the merging galaxies in terms of star formation relation. As shown in section 1.2, the main conclusion in literature is that star formation in the normal isolated disk galaxies is often regarded as the long-lasting mode, whereas starburst galaxies are experiencing a more rapid mode (higher star formation efficiency) due to galaxies involved in a major merger. In order to confirm this idea, it is necessary to investigate the exact location of interacting galaxies on star formation relation through systematic observations along the merger sequence from early stage (before coalescence) to late stage (after coalescence) with a various SFR range. However, previous studies are biased to late stage mergers that have intense starburst activity. In my project, I conducted ASTE CO (3–2) survey observations for merging galaxies (total

observation time 120 hours). I investigated the relation between the CO (3–2) luminosities ($L_{\rm CO} \propto M_{\rm H_2}$) and the far-infrared luminosity ($L_{\rm FIR} \propto$ SFR) (which is a fundamental relation to determine star formation relation) in a sample of 29 early- and 31 late- stage merging galaxies and 28 nearby isolated spiral galaxies.

- **Where and how much is the starburst triggered during the merger process? (Chapter 3)**

  Second, I investigated the details of star formation activity in a merging galaxy. As shown in Chapter 2, a galaxy collision plays an important role for global star formation activity in galaxies. The goal of second project is to answer the question of "Where are starbursts triggered in merging galaxies". As a kick off study, I selected one merging galaxy NGC 3256 which consists of two galaxies; one is the northern starburst galaxy and the other is the southern dusty galaxy hosting a low luminosity AGN. First, I use optical integral field units (MUSE mounted on Very Large Telescope) and obtain maps of recombination lines (i.e., Hα and Hβ). However, it is difficult to investigate star formation activities in dusty regions by using optical observations. Instead, I use mm/sub-mm recombination lines to investigate "true" star formation activity without dust extinction. I observed H40α and H42α in 3mm waveband by using ALMA.

- **What kind of structure and properties do molecular outflows have?** (Chapter 4)

  Finally, I describe the feedback process. Starburst and AGN feedback occur in the form of galactic-scale outflows. Recently, a number of studies has reported identifications of molecular outflows in CO observations by using

ALMA. They measured the mass and velocity of outflows. However, in order to include the feedback process into galaxy evolution model, the other properties of outflows should be investigated. The detection of outflows by using dense gas tracer is one of the keys to characterize the physical and chemical properties of outflows. The aim of the third project is to identify dense gas in molecular outflow. I use multi-lines (e.g., CO, HCN and HCO^+) to characterize the structure, density and temperature, and chemistry of the outflows. NGC 3256 is an ideal target since two low J ($J < 3$) CO outflows from the two nuclei (starburst and low-luminosity AGN) have already been reported. Based on the physical properties of molecular outflow, I investigate how outflows affect the evolution of host galaxies.

2 | ASTE Merging Galaxy Survey

2.1 Science Goal

The goal of this project presented in this chapter is to reveal the evolution of the merging galaxies in terms of the star formation relation. As shown in section 1.2, star formation relation for normal and starburst galaxies show a bimodal sequence in mass - IR luminosity ($M_{\mathrm{H_2}} - SFR$) , molecular gas mass surface density - SFR surface density ($\Sigma_{M_{\mathrm{H_2}}} - \Sigma_{SFR}$) plane, and fundamentally CO luminosity - FIR luminosity plane ($L'_{\mathrm{CO}} - L_{\mathrm{FIR}}$) (Genzel et al. , 2010; Daddi et al. , 2010). The bimodal sequence means that long-lasting star formation in disk galaxies and rapid mode in starburst galaxies possibly triggered by a major merger process. This means that star formation efficiency (SFE=SFR/M_{H_2}) is higher in starburst galaxies than disk galaxies. This is predicted in recent theoretical merger models (e.g., Teyssier et al. , 2010; Bournaud , 2011). In their model, one important phenomena is global gas inflow which increases the average gas density and the SFR (nuclear starburst). This is a standard process and occurs late stage of merger process (after coalescence) effectively. In addition, the gist of their argument is that fragmentation of high-dispersion gas outer the nuclear region (which triggers extended starburst) is equally important especially in the early phase (before coalescence). On the other hand, (Powell et al. , 2013) show no evidence of a bimodal relationship in the simulated Kennicutt-Shmidt relation by merging galaxies. In addition, some other numerical simulations of merging galaxies provided by Powell et al. (2013) have shown that all merging galaxies (not only starburst systems like the Antennae galaxy but also lesser degree ones) are in between the disk sequence and the

starburst sequence. In order to observationally confirm that merging galaxies are between two sequences, it is necessary to investigate the exact location of interacting galaxies through systematic observations along the merger sequence from early stage (before coalescence) to late stage (after coalescence) with a large FIR range. However, previous studies are biased to late stage mergers that are bright in the FIR luminosity like U/LIRGs (e.g., Downes & Solomon , 1998). In this project, I observed optically selected merging galaxies along the complete merger sequence with a wide FIR range ($10^8 L_\odot < L_{\rm FIR} < 10^{12} L_\odot$).

I note that I use the relation between $L'_{\rm CO(3-2)}$ and $L_{\rm FIR}$ rather than $M_{\rm H_2}$ and SFR in order to avoid the large systematic errors due to the uncertainty of CO-to-H_2 conversion factor. For example, Bolatto et al. (2013b) show that CO-to-H_2 conversion factor is different for ULIRGs ($\sim 0.8\ M_\odot$ (K kms^{-1} pc^2)$^{-1}$) and normal galaxies ($\sim 4.2\ M_\odot$ (K kms^{-1} pc^2)$^{-1}$). Bournaud et al. (2015) suggest CO-to-H_2 conversion factor ($\sim 2\ M_\odot$ (K kms^{-1} pc^2)$^{-1}$) for starburst mergers due to strong ISM turbulence in starburst mergers. Bournaud et al. (2015) suggest CO-to-H_2 conversion factor ($\sim 2\ M_\odot$ (K kms^{-1} pc^2)$^{-1}$) for starburst mergers due to strong ISM turbulence in starburst mergers. On the other hand, their model predicts that higher CO-to-H_2 conversion factor (~ 4) for high-z disk galaxies than star-burst mergers. Narayanan et al. (2012); Renaud et al. (2018) show that the conversion factor varies during the course of a merger evolution. Nevertheless, our current data is insufficient to address this issue at present and deferred to future studies that include the analysis of the CO (1–0) data in the same sources. The $L_{\rm FIR}$-to-SFR conversion can also be uncertain for galaxies with small FIR luminosity where the UV luminosity may be a better indicator of the SFR. Part of this chapter is published in the PASJ, 68, 96, (2016) as Investigating the relation between CO (3–2) and far-infrared luminosities for nearby merging galaxies using ASTE by Tomonari

Michiyama (Michiyama et al. , 2016).

2.2 CO (3–2) observations

Molecular gas is the ingredient for star formation. In Galactic star forming regions, active high-mass star formation is associated with dense molecular gas. Observing dense molecular gas is crucial for understanding star formation process and timescale. There is an empirical linear relation between the luminosity of the FIR and dense gas tracers such as CO (3–2) and HCN (1–0) whose critical densities are $\sim 10^{4-7}$ cm^{-3} (Tielens , 2005) in local galaxies. Theoretical models basically suggest that linear relation is seen because dense gas is likely to be direct fuel for massive star formation (e.g., Krumholz & Thompson , 2007; Narayanan et al. , 2008). Therefore, CO (3–2) emission line can be used as a tracer of the moderately dense and warm gas heated by star formation. As a pilot study, Iono et al. (2009) show the correlation between CO (3–2) luminosities and FIR luminosities based on Submillimeter array (SMA) observations of 14 local Ultra/luminous Infrared Galaxies (U/LIRGs) and high-z sources. Wilson et al. (2012) further investigate the CO (3–2) luminosities of more quiescent disk galaxies in the local universe and find that star formation efficiency in disk galaxies is lower than that of merging U/LIRGs. In addition, Muraoka et al. (2016) show universal CO (3–2) to FIR luminosity relation in different types of galaxies observed at different luminosity, i.e., from spatially resolved giant molecular associations in nearby galaxy disks to starburst ULIRGs.

2.3 Telescopes

2.3.1 ASTE

I use Atacama Submillimeter Telescope Experiment (ASTE) [1] (ASTE: Ezawa et al. , 2008) (Figure 2.1) to observe CO (3–2) emission. ASTE is a 10-m submillimeter telescope. It was installed at Atacama desert, Chile, in 2002 March. Since it is located 4,800 meters above sea level, the observing condition at the telescope site is excellent. We can observe in the 0.1 mm - 1mm wavelength range, which cover the CO (3–2) emission. ASTE is a powerful telescope to investigate the center of our own galaxy, nearby star-forming regions, and distant galaxies, and has brought many new results. Smooth telescope surface (accuracy is within 19 micron) enables us to perform submillimeter observations efficiently. In addition, we can operate the telescope remotely even from Japan (Sekimoto & Lmsa Working Group , 2001). A new cartridge-type side-band separating (2SB) mixer receiver for 350 GHz band, DASH345, is available from 2015. Tunable LO frequency range is 327 GHz to 370 GHz. IF frequency range is 4.0 GHz to 8.0 GHz. Observable frequency range (LO frequency range +/– IF center frequency) is 321 GHz to 376 GHz. We can observe two linear polarization (P0 and P1) with DASH345 (Ezawa et al. , 2008). CATS345 has similar frequency coverage, but we cannot observe polarization. CATS345 was available until 2014. The observational efficiency is twice higher in 2015 than in 2014. Those receivers covers the CO (3–2) emission frequency $\sim$ 345 GHz (Ezawa et al. , 2008). The WHSF is an FX-type spectrometer. Two observing modes, i.e., 4,096 MHz width mode and 2,048 MHz width mode, are available. The wide frequency width enable us to observe the line emission with large velocity dispersion from extra galactic sources. Thanks to the double polarization receiver and wide

[1] see ASTE web page http://alma.mtk.nao.ac.jp/aste/

frequency spectrometer, ASTE is the strong tool to investigate the global molecular gas properties that are traced by CO (3–2) emission from nearby extra galactic sources.

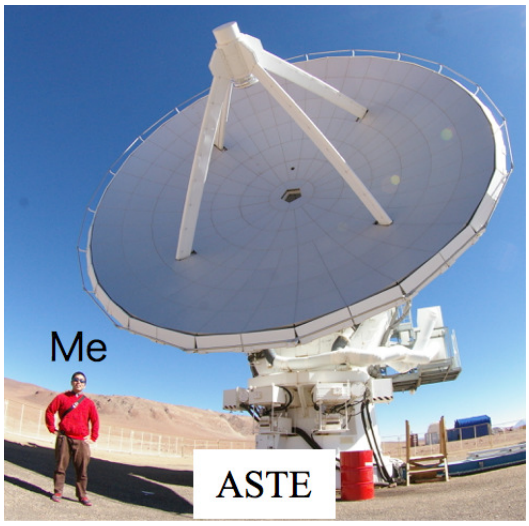

Figure 2.1 The outside appearance of ASTE.

2.3.2 AKARI

I use the AKARI point source catalog (Yamamura et al. , 2010) to measure the total infrared luminosity L_{FIR}. AKARI[1] is the Japanese infrared astronomical satellite launched in 2006 (Figure 2.2). The main objective of the AKARI mission is to perform an all-sky survey at infrared wavelength. AKARI has four bands centered on 65, 90, 140, and 160 μm, and a far infrared all-sky survey was completed by this instrument. AKARI achieved a sensitivity one order of magnitude better and resolution a few times higher (1 to 1.5 arcminutes) than IRAS (Infrared Astronomical Satellite). IRAS is the first infrared astronomical satellite launched in

[1] https://www.ir.isas.jaxa.jp/AKARI/index.html

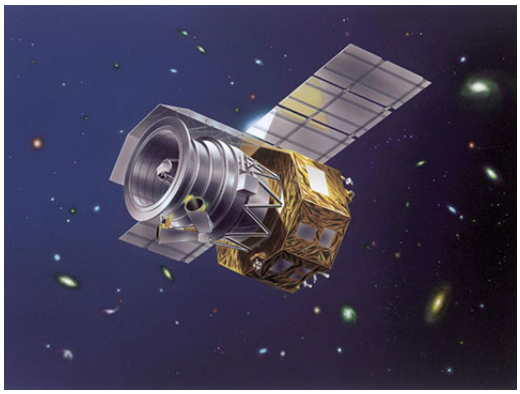

Figure 2.2 The outside image of AKARI. © JAXA

1983, so AKARI made a second-generation survey of infrared astronomy. The L_{FIR} are mostly measured by using IRAS catalog in literature. However there are minor differences between literature when they measure lumonosity. In order to estimate L_{FIR} in the same manner toward all sample, we use the DARTS catalog match system [2] to match our catalog and AKARI point source catalog. I re-measure the L_{FIR} with AKARI data using the equation derived in Takeuchi et al. (2010). I use equation (6) $\sim$ (8) and (11) in Takeuchi et al. (2010).

$$L^{\rm 2band}_{\rm AKARI} = \Delta\nu({\rm WIDE\text{-}S})L_\nu(90\,\mu{\rm m}) + \Delta\nu({\rm WIDE\text{-}L})L_\nu(140\,\mu{\rm m}) \quad (2.1)$$

$$\Delta\nu({\rm WIDE\text{-}S}) = 1.47\times10^{12}\ [{\rm Hz}] \quad (2.2)$$

$$\Delta\nu({\rm WIDE\text{-}L}) = 0.831\times10^{12}\ [{\rm Hz}] \quad (2.3)$$

$$\log L_{\rm FIR} = 0.964\log L^{\rm 2band}_{\rm AKARI} + 0.814 \quad (2.4)$$

The error $L^{\rm err}_{\rm FIR}$ is measured from AKARI 90 μm and 140 μm flux error ($\sim$ 5 % and 10 % respectively). We caution here that this error only contains the photometric

[2] http://www.darts.isas.jaxa.jp/astro/akari/

errors.

2.4 Sample selection

[early stage merger] I selected "early-stage merger" (double nuclei in an optical image) from the VV catalog (Vorontsov-Velyaminov , 1959; Vorontsov-Velyaminov et al. , 2001), using the following criteria: (a) both galaxies have measured B-band magnitudes, and the difference of the B-band magnitude between the two galaxies in a system is < 3 mag (in order to select major mergers); (b) the system is identified in the IRAS Revised Bright Galaxy Sample: IRAS RBGS: (Sanders et al. , 2003); (c) the optical radial velocity is known for both sources; and (d) the declination is $< 30°$. My initial sample selection has 40 systems. However, I have observed only 6 systems (VV 81, VV 217, VV 242, VV 272, VV 352 and VV 729) due to the limited ASTE observation time. In addition to these 6 systems, I observed VV 122, VV 830 and VV731. Even though VV 122 and VV 830 are categorized into Nest and Enigmatic respectively by Vorontsov-Velyaminov (1977), they are merging galaxies with two nuclei. The B-band magnitude for VV 731 is measured as one source, but ASTE can resolve the two nuclei. Additionally, I observed IRAS F16399-0937 as an early-stage merging galaxy: the ASTE 22" beam covers both nuclei separated by 3.4 kpc. The Digitized Sky Survey (DSS) images for these systems are shown in Figure 2.3, and the pointing positions and velocity information are presented in Table 2.1.

[late stage merger] Additionally, I selected three "late-stage merger" (single nucleus in an optical image) from RBGS with a declination $< 30°$(ESO 286-IG019, NGC 1614, and NGC 7252) and four (AM 2038-382, Arp 230, Arp 187, and UGC 6) with $L_{\rm FIR} < 10^{11}$ $L_{\odot}$ from Ueda et al. (2014). The DSS images for these systems are shown in Figure 2.4. The pointing positions and velocity information are

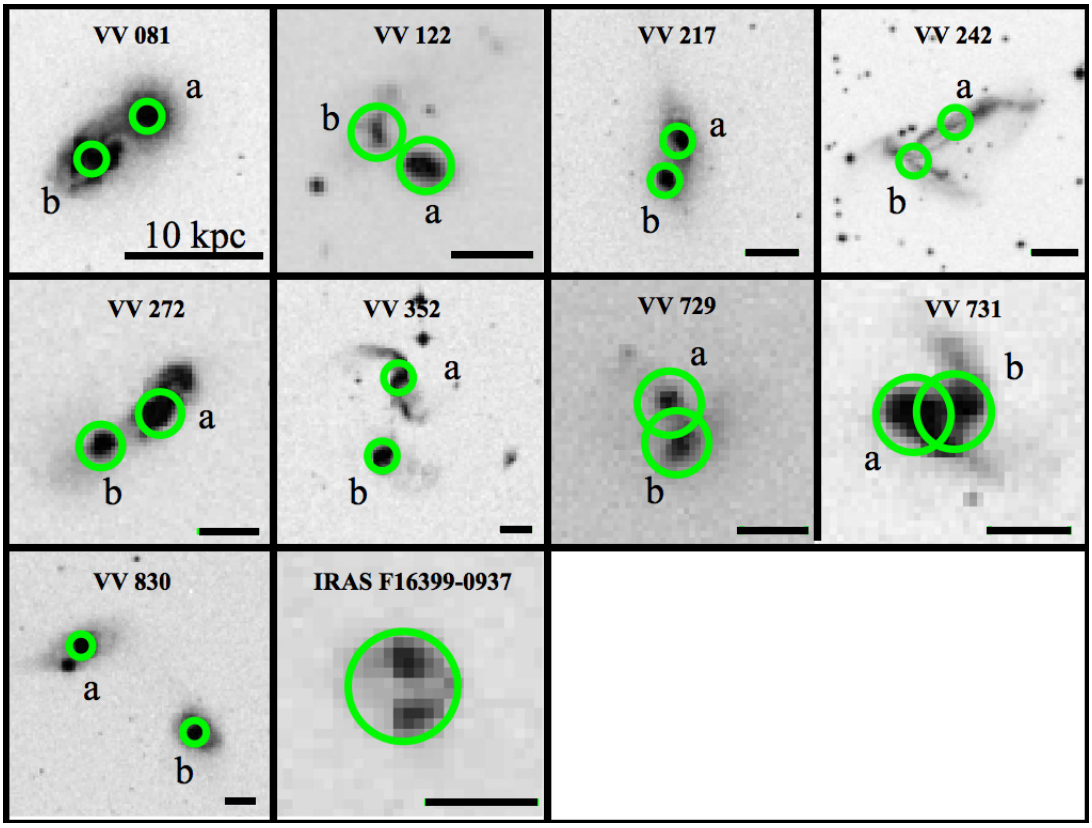

Figure 2.3 The DSS blue band images of the early stage mergers. The green circles show the observing positions with ASTE 22″ beams. The lines on the bottom-right show the 10 kpc scale length.

Table 2.1 Early-stage merging galaxy sample.

Source	RA J2000	DEC J2000	Vel. [km s^{-1}]
(1)	(2)	(3)	(4)
VV 081a	00:51:01.8	-07:03:25	1,750
VV 081b	00:51:04.4	-07:03:56	1,744
VV 122a	01:58:05.3	+03:05:01	5,431
VV 122b	01:58:06.6	+03:05:15	5,589
VV 217a	02:29:09.7	-10:49:43	4,686
VV 217b	02:29:10.3	-10:50:10	4,516
VV 242a	22:19:27.8	+29:23:45	4,569
VV 242b	22:19:30.0	+29:23:17	4,493
VV 272a	00:06:27.0	-13:24:58	5,729
VV 272b	00:06:29.0	-13:25:14	5,717
VV 352a	00:18:50.1	-10:21:42	8,193
VV 352b	00:18:50.9	-10:22:37	8,125
VV 729a	03:41:10.5	-01:18:10	7,750
VV 729b	03:41:10.7	-01:17:56	7,592
VV 731a	23:18:22.6	-04:24:58	7,250
VV 731b	23:18:21.8	-04:24:57	7,380
VV 830a	00:42:52.8	-23:32:28	6,664
VV 830b	00:42:45.8	-23:33:41	6,787
IRAS F16399-0937	16:42:40.2	-09:43:14	8,098

Notes. (1): source name. (2)(3): Observed coordinate. (4) Helio. Radial Velocity from NED.

presented in Table 2.2.

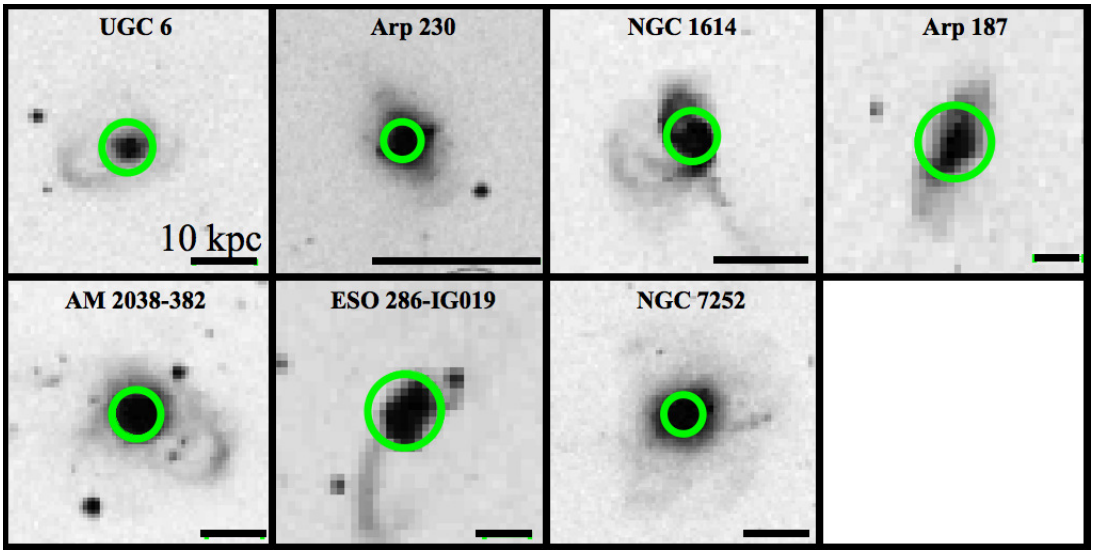

Figure 2.4 The DSS blue band images of the late stage mergers. The green circles show the observing positions with ASTE 22″ beams. The lines on the bottom-right show the 10 kpc scale length.

2.4.1 Supplementary data

I use the CO (3–2) data of nearby galaxies obtained with both single dish telescope and interferometer as supplementary data. Iono et al. (2009) observed the CO (3–2) emission from 14 nearby merging U/LIRGs with SMA (Submillimeter Array) in Hawaii. Leech et al. (2010) observed nearby merging U/LIRGs with JCMT (James Clerk Maxwell Telescope) in Hawaii, and the observed galaxies are small enough for JCMT beam size (14.4"). Three late stage merging galaxies (NGC 828, UGC 5101, NGC 4194) in Ueda et al. (2014) were observed in CO (3–2). Those galaxies yield a combined sample of 29 early stage mergers and 31 late stage mergers with a wide range of FIR luminosity ($L_{\rm FIR} \sim 10^9 - 10^{13} L_\odot$). Wilson

Table 2.2 Late-stage merging galaxy sample.

Source	RA J2000	DEC J2000	Vel. [km/s^{-1}]
(1)	(2)	(3)	(4)
UGC 6	00:03:09.6	+21:57:39	6,579
Arp 230	00:46:24.2	-13:26:32	1,720
NGC 1614	04:34:59.8	-08:34:46	4,778
Arp 187	05:04:53.0	-10:14:51	12,095
AM 2038-382	20:41:13.9:	-38:11:37	6,092
ESO 286-IG019	20:58:26.8	-42:39:02	12,890
NGC 7252	22:20:44.7	-24:40:42	4,792

Notes. (1): source name. (2)(3): Observed coordinate. (4) Helio. Radial Velocity from NED.

et al. (2012) performed CO (3–2) mapping of 28 nearby isolated spiral galaxies by using JCMT. Comparing those sample and mine, I can investigate the difference of star formation efficiency (SFE) in both mergers and non-merging systems. Due to the difference in distance, the observing modes are different for spiral and merging galaxies: single-dish mapping for spiral galaxies, and interferometric or single-point observations for merging galaxies. I note that SMA observations might have missing flux but it is difficult to correct it. Figure 2.5 shows that the number of early stage merging galaxies with low FIR luminosity ($10^9 < L_{\rm FIR} < 10^{11}$) has increased in this work.

The discussions in this chapter are based on the sample sources shown above. I note that there are a few more CO (3–2) observations in the literature toward nearby galaxies. For example, Yao et al. (2003) investigated CO (3–2) emission in various types of galaxies with JCMT. However, unlike the sample sources above, they performed single point observation regardless of the galaxy size. This means

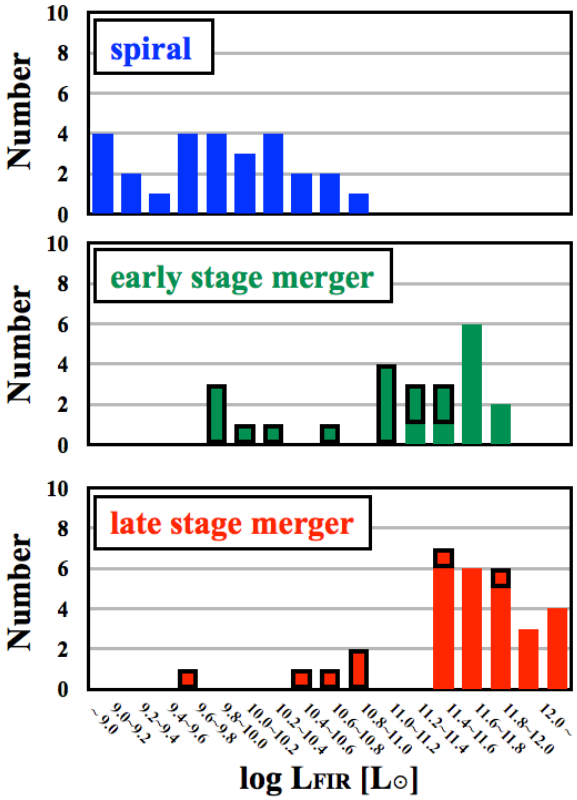

Figure 2.5 Histogram of the FIR luminosities of the three samples. The green, red, and blue bars show early-stage mergers, late stage mergers, and isolated spirals, respectively. The black boxes show sources which we observed with ASTE, and the others are galaxies from the literature (Wilson et al. , 2008; Leech et al. , 2010; Wilson et al. , 2012).

that in some cases they measure the CO emission from the nucleus of the galaxy and a direct comparison with our sample is difficult. Therefore, I don't use sample in Yao et al. (2003) for comparison in this thesis. Mao et al. (2010) performed the largest CO (3–2) survey towards various types of galaxies. They investigate the relationship between $L_{\rm FIR}$ of whole galaxy and $L'_{\rm CO}$ of nuclear region, so I cannot directly compare the sources in Mao et al. (2010) and our project since $L_{\rm CO}$ is measured toward whole galaxy in our work. Therefore, I do not use the galaxies observed in Mao et al. (2010) for comparison. The same problem is seen for the sample of Komugi et al. (2007), Narayanan et al. (2008) and Vila-Vilaró et al. (2003). Papadopoulos et al. (2012) compiled CO(3–2) data for nearby U/LIRGs from various telescope in different projects, so it is hard to determine which observation is applicable for our projects. However, most of the merging galaxies in Papadopoulos et al. (2012) are covered by Iono et al. (2009) and Leech et al. (2010), and thus they are already included in our sample.

2.4.2 FIR Luminosity in The Early Stage Merging Galaxies

The spatial resolution of *AKARI* is too coarse to derive the FIR emission separately for the two galaxies in the early stage mergers. One way to separate the contribution is to scale the FIR luminosity according to the ratio of the radio continuum emission, assuming that the radio to FIR correlation holds true in these galaxies (Yun et al. , 2001). Another way is to scale the FIR emission through the *K*-band flux ratio, again assuming a correlation between the SFR (derived from FIR luminosity) and the stellar mass (derived from *K*-band). By using the 1.5 GHz images obtained from the Karl G. Jansky Very Large Array (VLA) archive, I find that six of the early stage mergers have radio emission only from one galaxy in a system (VV 081, VV 122, VV 242, VV 272, VV 352, and VV 731). For these sources, I

assume that all of the FIR emission arises from the galaxy with radio detection. If the radio emission is detected from both galaxies, I distribute the total FIR luminosity according to the flux ratio of the 1.5 GHz emission ($a : b = 38 : 62$ for VV 731 and $39 : 61$ for VV 830). Finally, I use the flux ratio of 2MASS (Cutri et al. , 2003) 2.2 μm ($a : b = 55 : 45$ for VV 217 and $63 : 37$ for VV 729) for galaxies with no VLA detection from either of the galaxy in the pair.

2.5 ASTE observation

I observed the CO (3–2) line emission toward the sample sources with the Atacama Submillimeter Telescope Experiment (ASTE) during the observing seasons 2014B, 2015A, 2015B, and 2015C. The total observation time was $\sim$120 hours (including overhead) to observe all 26 individual galaxies. I conducted single point observations with the position switch mode. The main beam size is $22''$ at 345 GHz, and I specify the OFF position to be $5'$ away from the target sources. I used two types of receivers; CATS345 (Inoue et al. , 2008) in 2014B and DASH345 in 2015A, 2015B, and 2015C. I used the 2048 MHz mode of WHSF (Iguchi & Okuda , 2008; Okuda & Iguchi , 2008) for the backend spectrometer (velocity resolution and coverage are 0.86 and 1750 km s^{-1} at 350 GHz, respectively). R-sky calibration was carried out every 15 minutes, and the system noise temperature was typically 200–400 K. Absolute flux scales of the obtained spectra were calibrated by observing a standard source at least once a night. The average main beam efficiency is $\eta_{\rm mb} = 0.57 \pm 0.08$. I checked the pointing of the telescope every 60–90 minutes and the errors were typically $< 3''$. The ASTE $22''$ beam corresponds to ~ 2.5 kpc for the nearest target Arp 230 ($D_{\rm L} = 19.3$ Mpc). Since the typical CO (3–2) size of LIRGs is $0.3 - 3.1$ kpc (Iono et al. , 2009), I assume that our ASTE $22''$ beam is large enough (at least comparable) to trace the emission from the bulk of the galaxy.

2.5.1 *Data Reduction and Analysis*

I use NEWSTAR which is the software package developed at the Nobeyama Radio Observatory to process the raw data. Low quality spectra with winding baselines are flagged by eye and only the high quality spectra are integrated. The flag rate ($\sim$ 30 – 70 %) strongly depends on the weather condition. The spectra are then smoothed to a velocity resolution of 30 km s^{-1} (for sources with clear CO (3–2) detection) or 50 km s^{-1} (for non-detection) with a boxcar function in order to improve the signal to noise ratio (S/N). Baselines are fitted with a polynomial function of order one, but we used second and third orders in some cases with large baseline fluctuations. We succeeded to detect CO (3–2) emission ($T_{\rm peak}/\sigma_{\rm r..m.s} > 4$) from 17 sources, and the final spectra are shown in figure 2.6.

I derive the integrated CO (3–2) properties of the sources that show more than three continuous channels with positive $> 3\sigma$ signal. The CO velocity-integrated intensity is derived using the following formula:

$$I_{\rm CO} = \int T_{\rm mb} dV = \int \frac{T_{\rm A}^{\star}}{\eta_{\rm mb}} dV \tag{2.5}$$

where $I_{\rm CO}$ is in the unit of K km s^{-1}, $T_{\rm mb}$ is the main beam temperature in Kelvin, and $\eta_{\rm mb}$ is 0.47 - 0.71. The errors in $I_{\rm CO}$ for the value listed in table 2.3 were calculated using

$$\sigma_{I_{\rm CO}} = \sigma_{\rm R.M.S.} \sqrt{(\Delta V_{\rm CO} \delta V)} \tag{2.6}$$

where $\sigma_{\rm R.M.S.}$ is the R.M.S. noise of $T_{\rm mb}$ in Kelvin, $\Delta V_{\rm CO}$ is the full line width in km s^{-1} (the range between FWZI in table 2.3), and δV is the velocity resolution in km s^{-1} (30 km s^{-1} for detected sources). The derived errors are in the range of 6–20 % of measured $I_{\rm CO}$. The 3σ upper limits of $I_{\rm CO}$ for non-detected sources were

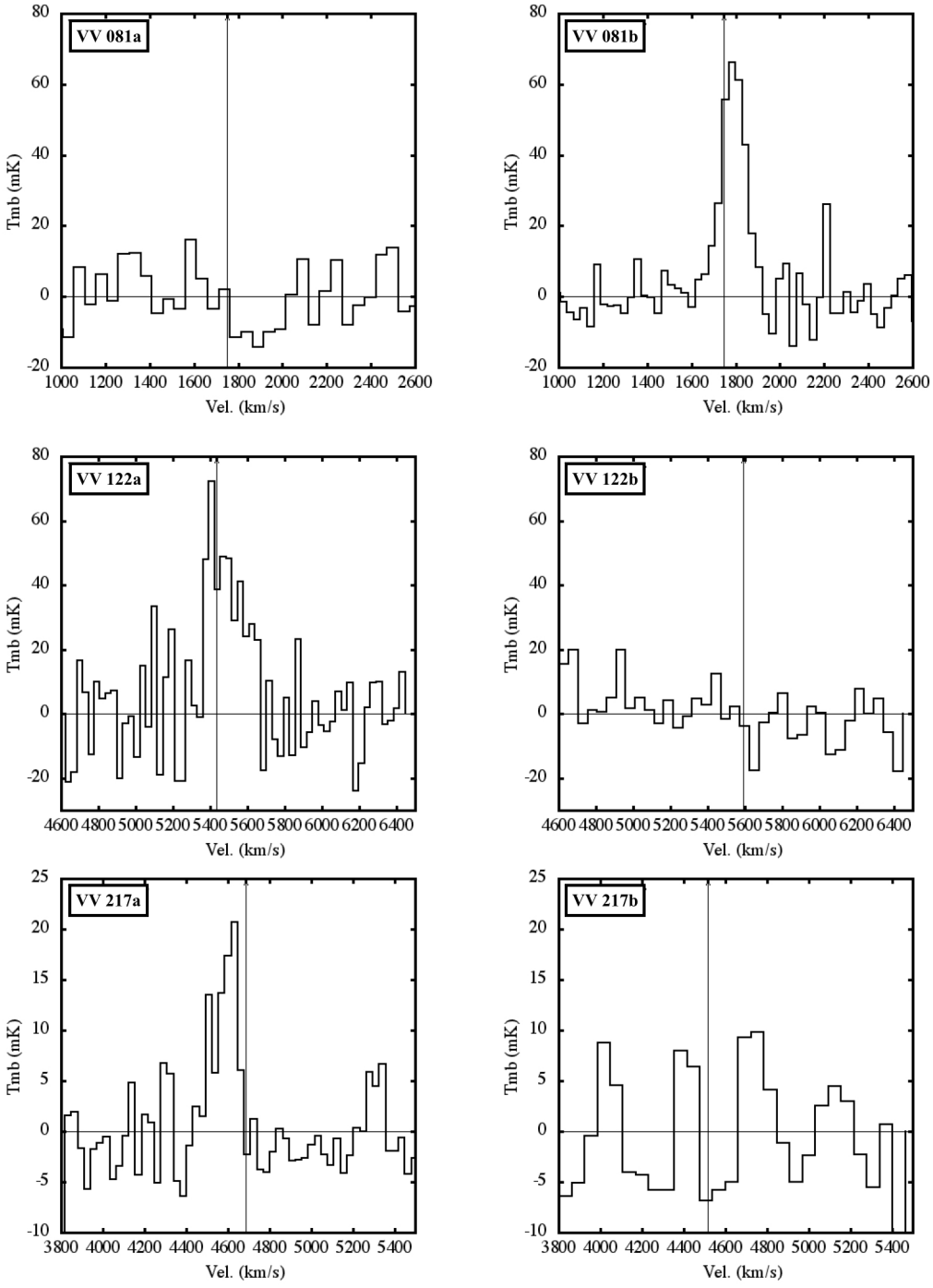

Figure 2.6 CO (3–2) spectrum of our ASTE observation sample. The velocity resolution is 30 km s^{-1} for detected sources and 50 km s^{-1} for non-detected sources. The vertical line represents the systematic velocity from NED.

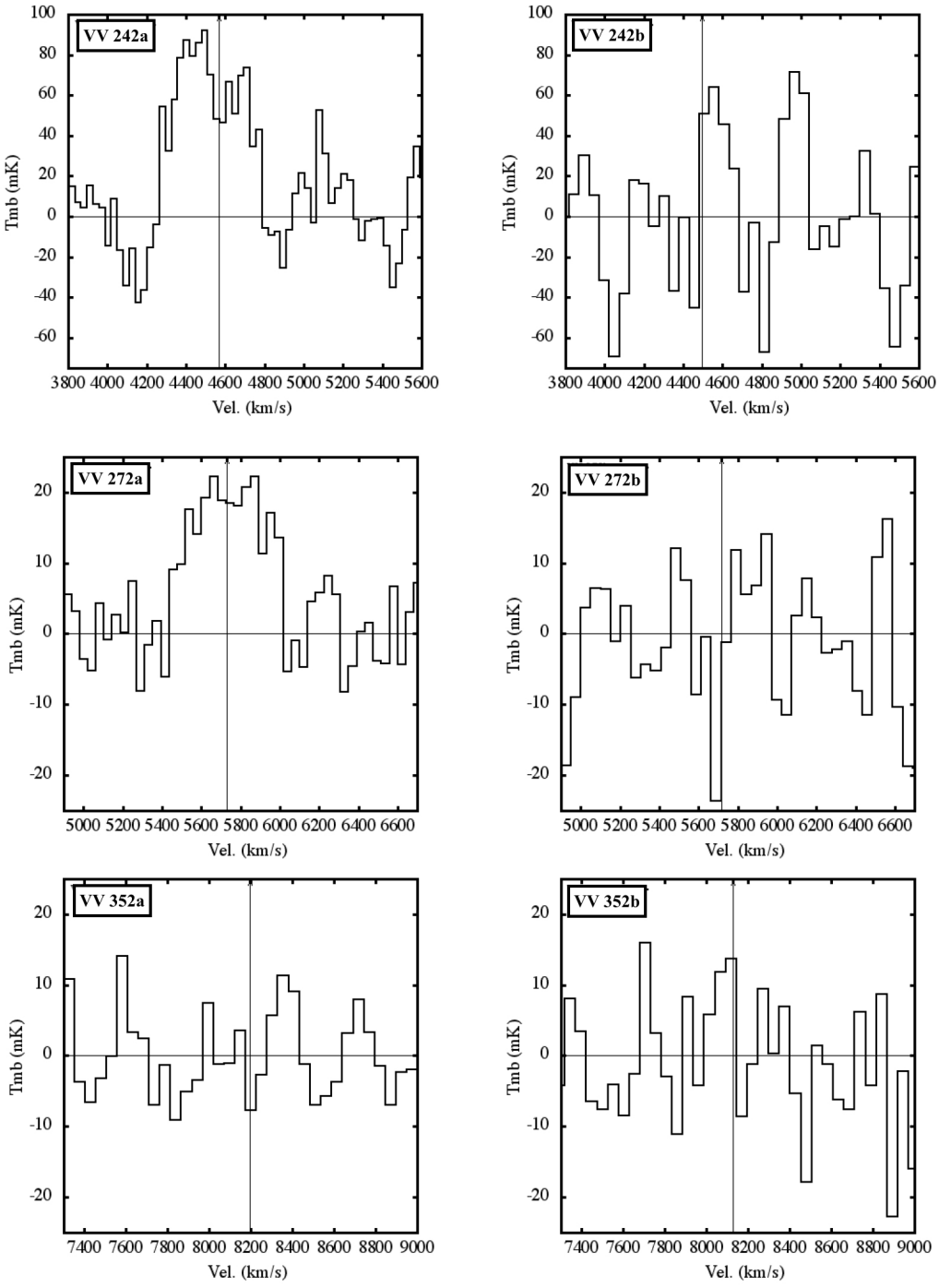

Figure 2.6 continued

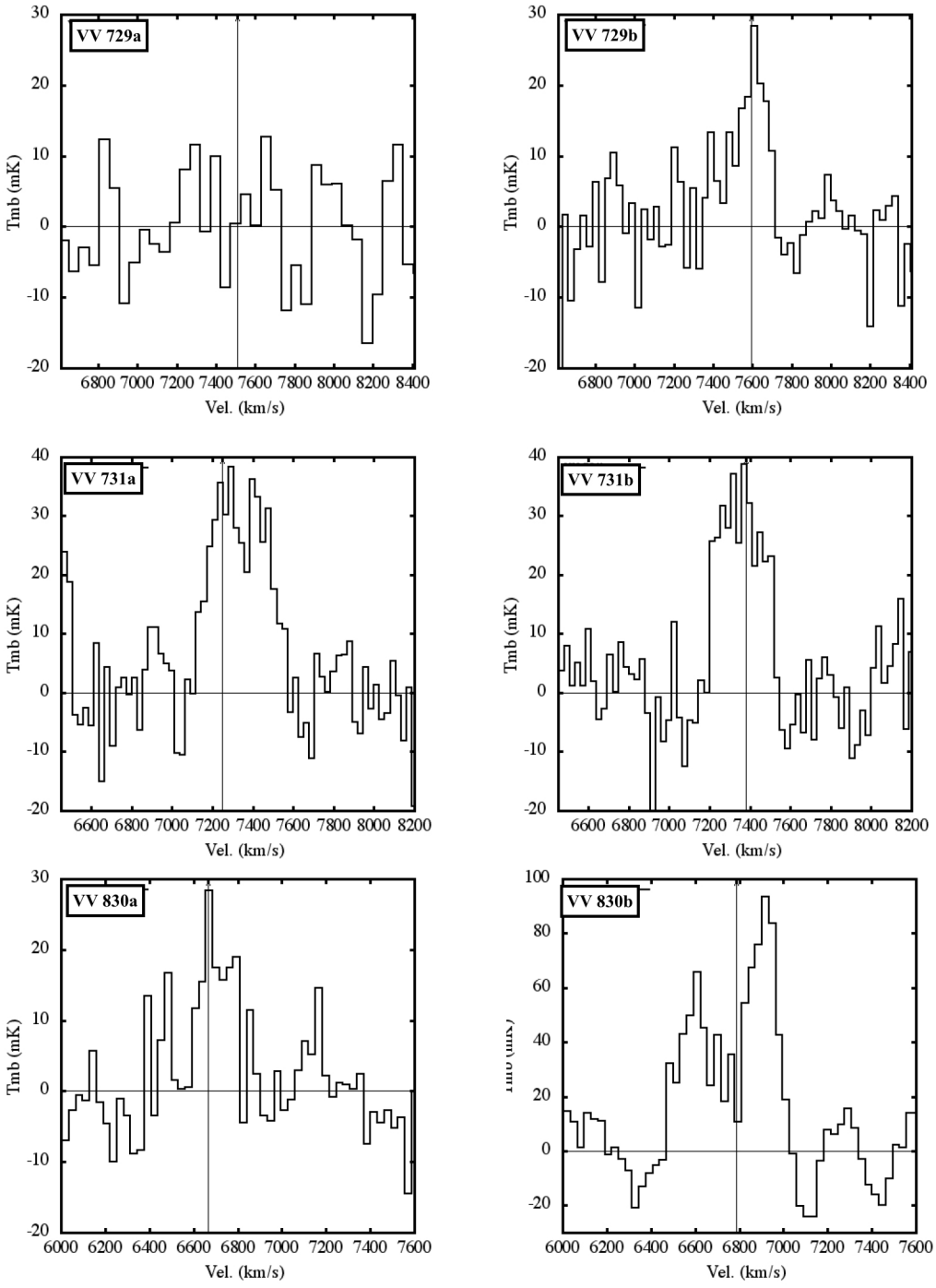

Figure 2.6 continued

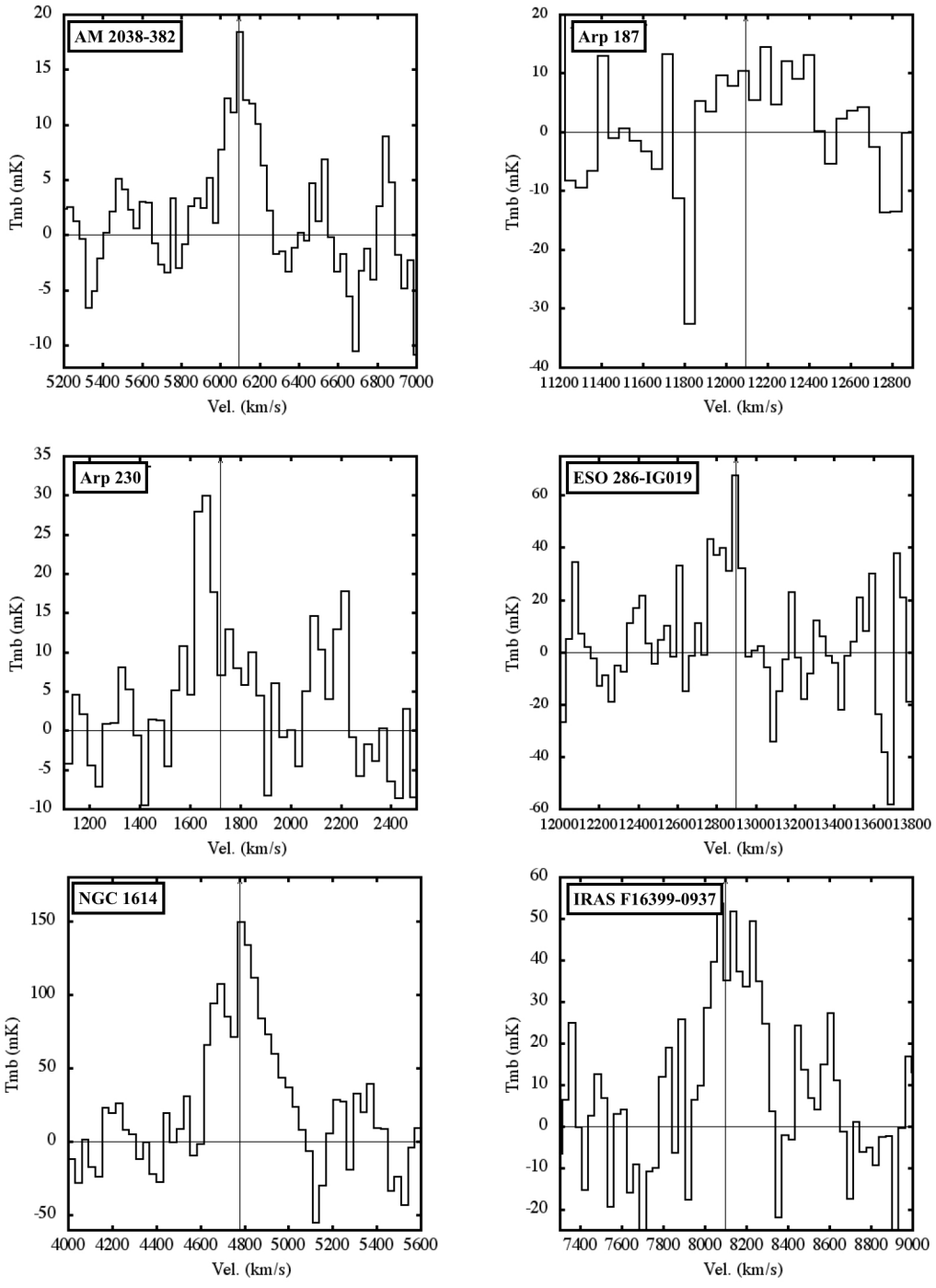

Figure 2.6 continued

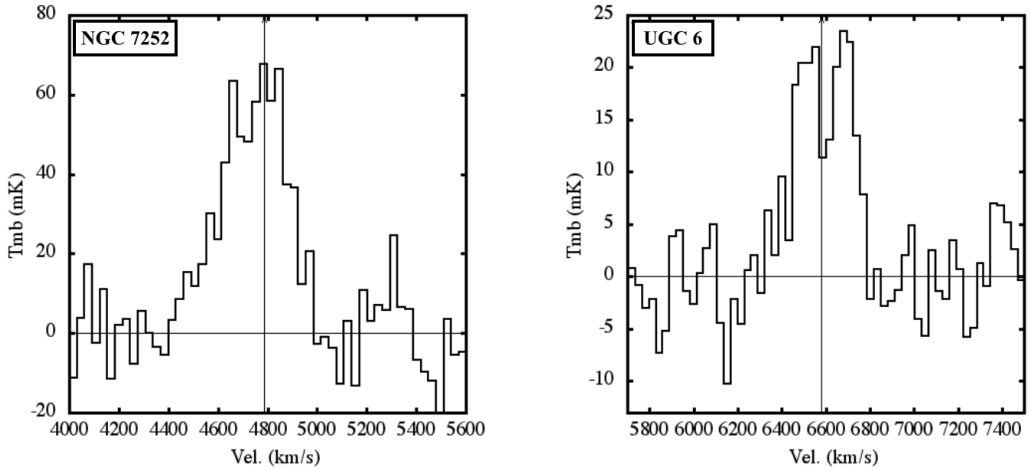

Figure 2.6 continued

measured by assuming gaussian profile,

$$I_{\rm CO}^{\rm upper} = \frac{\sqrt{2\pi}}{2}\sigma_V(\sigma_{\rm R.M.S.} \times 3) \tag{2.7}$$

where σ_V is the velocity dispersion of the emission line which is assumed to be $\sigma_V = 200$ km s^{-1} (FWHM$\sim$ 500 km s^{-1}). The $L'_{\rm CO(3-2)}$ is calculated by using the following equation (Solomon & Vanden Bout , 2005),

$$L'_{\rm CO(3-2)} = 23.5\Omega_{\rm s\star b}D_{\rm L}^2 I_{\rm CO}(1+z)^{-3}. \tag{2.8}$$

The $L'_{\rm CO(3-2)}$ is given in K km s^{-1} pc^2. The $\Omega_{\rm s\star b}$ is the solid angle of the source convolved with the telescope beam in arcsec^2 assuming that CO is uniformly distributed in ASTE beam. The $D_{\rm L}$ is the luminosity distance in Mpc. I summarize the observational information in table 2.3 and 2.4.

Table 2.3 ASTE CO (3–2) observation for early stage mergers

source	t_{integ}	$\sigma_{R.M.S.}$ [mK]	T_{peak} [mK]	S/N	FWZI [km s^{-1}]	FWHM [km s^{-1}]	I_{CO} [K km s^{-1}]	I_{CO}^{err} [K km s^{-1}]
(1)	(2)	(3)	(4)	(5)	(6)	(7)	(8)	(9)
VV 081a	14m20s	8.4	< 25.2	-	-	-	< 6.32	-
VV 081b	28m15s	7.1	66.3	9.3	1,620-1,920	130	9.13	0.67
VV 122a	6m50s	13.0	72.3	5.6	5,360-5,660	150	11.85	1.23
VV 122b	31m30s	6.9	< 20.7	-	-	-	< 5.19	-
VV 217a	129m00s	3.3	20.7	6.3	4,430-4,670	100	2.45	0.28
VV 217b	105m25s	5.6	< 16.8	-	-	-	< 4.21	-
VV 242a	8m50s	20.5	92.3	4.5	4,270-4,780	410	32.83	2.54
VV 242b	24m40s	37.9	< 113.7	-	-	-	< 28.50	-
VV 272a	49m05s	4.7	22.3	4.7	5,440-5,890	500	9.41	0.55
VV 272b	25m10s	8.7	< 26.1	-	-	-	< 6.54	-
VV 352a	29m00s	6.0	< 18.0	-	-	-	< 4.51	-
VV 352b	118m00s	7.9	< 23.7	-	-	-	< 5.94	-
VV 729a	11m30s	7.6	< 22.8	-	-	-	< 5.72	-
VV 729b	37m50s	5.7	28.4	5.0	7,350-7,710	150	4.83	0.59
VV 731a	39m40s	6.3	38.3	6.1	7,120-7,630	330	11.31	0.78
VV 731b	40m50s	8.5	38.9	4.6	7,150-7,600	300	8.96	0.99
VV 830a	17m30s	6.3	28.3	4.5	6,590-6,800	170	3.90	0.50
VV 830b	22m30s	11.7	93.4	8.0	6,470-7,010	160	25.60	1.49
IRAS F16399-0937	25m00s	13.7	53.6	3.9	7,940-8,330	300	12.15	1.48

Notes. (1): source name. (2):Total on-source time after flagging bad baseline spectra. (3): Root mean square noise level measured with `NEWSTAR` in main beam temperature. (4): Peak temperature of CO (3–2) emission in main beam temperature. (5): Signal to noise ratio. $T_{peak}/\sigma_{R.M.S.}$. (6): The full width zero intensity. (7): Full width half maximum for emission spectrum.(8): CO (3–2) intensity in the unit of K km s^{-1}. (9): The error of CO (3–2) intensity in the unit of K km s^{-1}.

Table 2.4 ASTE CO (3–2) observation for late stage mergers

source	t_{integ}	$\sigma_{R.M.S.}$ [mK]	T_{peak} [mK]	S/N	FWZI [km s^{-1}]	FWHM [km s^{-1}]	I_{CO} [K km s^{-1}]	I_{CO}^{err} [K km s^{-1}]
(1)	(2)	(3)	(4)	(5)	(6)	(7)	(8)	(9)
AM 2038-382	90m30s	3.8	18.4	4.8	5,840-6,260	180	2.82	0.43
Arp 187	33m20s	10.2	< 30.6	-	-	-	< 7.67	-
Arp 230	95m40s	6.7	30.0	4.5	1,530-1,890	90	4.25	0.70
ESO 286-IG019	10m10s	14.5	67.4	4.6	12,760-12,940	50	7.89	1.07
NGC 1614	4m30s	22.4	149.5	6.7	4,620-5,120	150	35.30	2.60
NGC 7252	19m50s	9.2	67.7	7.4	4,400-4,970	300	20.51	1.20
UGC 6	55m10s	4.1	23.5	5.7	6,330-6,780	160	6.61	0.48

Notes. (1): source name. (2):Total on-source time after flagging bad baseline spectra. (3): Root mean square noise level measured with `NEWSTAR` in main beam temperature. (4): Peak temperature of CO (3–2) emission in main beam temperature. (5): Signal to noise ratio. $T_{peak}/\sigma_{R.M.S.}$. (6): The full width zero intensity. (7): Full width half maximum for emission spectrum.(8): CO (3–2) intensity in the unit of K km s^{-1}. (9): The error of CO (3–2) intensity in the unit of K km s^{-1}.

2.5.2 *Derivation of the Star Formation Efficiency (SFE)*

I assume that CO (3–2) emission can be a tracer of the total amount of dense gas (direct material of star formation) in a galaxy, and a dusty starburst activity is a dominant source of the FIR luminosities (The effect of AGNs is discussed in section 2.6.3). I can connect the dense gas mass to the current massive star formation by a comparison between $L'_{\rm CO(3-2)}$ and $L_{\rm FIR}$. I define the dense gas star formation efficiency (SFE) by taking the ratio between the FIR luminosity and the CO (3–2) luminosity,

$$\mathrm{SFE}\ [L_\odot\ (\mathrm{K\ km\ s^{-1}\ pc^2})^{-1}] = L_{\rm FIR}/L'_{\rm CO(3-2)}. \tag{2.9}$$

I use $L_{\rm FIR}/L'_{\rm CO(3-2)}$ rather than $SFR/M_{\rm H_2}$ in order to avoid additional ambiguities through the uncertainties of the excitation of the CO (3–2) line and CO to H_2 conversion factor. Table 2.5 show $L_{\rm FIR}$, $L'_{\rm CO(3-2)}$, and SFE for each source.

Table 2.5: $L_{\rm FIR}$, $L'_{\rm CO(3-2)}$, and SFE for nearby galaxies investigated in this project.

Source	$L_{\rm FIR}$	$L'_{\rm CO(3-2)}$	SFE	ref.
(1)	(2)	(3)	(4)	(5)
	$[10^{10}\ L_\odot]$	$[10^8$ K km s^{-1} pc$^2]$	$[L_\odot$ (K km s^{-1} pc$^2)^{-1}]$	
		—— early stage merging galaxies ——		
VV 081a	-	< 0.20	-	This work
VV 081b	0.62±0.03	0.39±0.03	159±14	This work
VV 122a	6.33±0.30	6.55±0.68	97±11	This work
VV 122b	-	< 3.23	-	This work
VV 217a	0.61±0.06	1.02±0.12	60±9	This work
VV 217b	0.46±0.05	< 1.71	> 38	This work
VV 242a	7.06±0.41	12.29±0.95	57±6	This work
VV 242b	-	< 10.92	-	This work
VV 272a	3.27±0.33‡	5.67±0.33	58±7	This work
VV 272b	-	< 4.17	-	This work

Table 2.5 (Continued.)

Source	$L_{\rm FIR}$	$L'_{\rm CO(3-2)}$	SFE	ref.
(1)	(2)	(3)	(4)	(5)
	$[10^{10}\ L_\odot]$	$[10^8$ K km s$^{-1}]$	$[L_\odot$ (K km s^{-1} pc$^2)^{-1}]$	
VV 352a	-	<6.08	-	This work
VV 352b	17.94±0.34	<7.87	>326	This work
VV 729a	1.58±0.16‡	<7.18	>31	This work
VV 729b	0.93±0.09‡	5.51±0.68	29±5	This work
VV 731a	6.78±0.34	11.40±0.79	59±5	This work
VV 731b	11.36±0.58	9.08±1.00	125±15	This work
VV 830a	7.20±0.45	3.26±0.42	221±31	This work
VV 830b	11.72±0.73	22.30±1.30	53±4	This work
IRAS F16399-0937	24.25±0.90	16.58±2.02	146±19	This work
Arp 299	29.99±2.00	12.59±0.28	238±17	Wilson et al. (2008)
NGC 5257/8	13.27±1.27	31.62±1.93	42±5	Wilson et al. (2008)
NGC 5331	35.79±1.42	25.12±0.37	142±6	Wilson et al. (2008)
Arp 236	27.24±1.06	50.12±0.99	54±2	Leech et al. (2010)
UGC 2369	31.73±1.08	15.85±1.78	200±23	Leech et al. (2010)
IRAS 03359+1523	27.18±1.73	12.59±2.56	216±46	Leech et al. (2010)
Arp 55	41.09±1.82	63.10±5.32	65±6	Leech et al. (2010)
Arp 238	39.81±4.04	12.59±2.09	316±61	Leech et al. (2010)
Arp 302	43.37±1.63	50.12±2.04	87±5	Leech et al. (2010)
NGC 6670	26.28±1.54	31.62±2.41	83±8	Leech et al. (2010)
	—— late stage merging galaxies ——			
AM 2038-382	2.31±0.19	2.03±0.31	114±20	This work
Arp 187	2.51±0.25‡	<24.05	>15	This work
Arp 230	0.30±0.02	0.18±0.03	168±31	This work
ESO 286-IG019	57.07±3.05	25.63±3.46	223±32	This work
NGC 1614	24.25±1.19	16.43±1.21	148±13	This work
NGC 7252	4.35±0.33	8.61±0.50	51±5	This work
UGC 6	5.90±0.28	5.29±0.38	111±10	This work
NGC 2623	26.52±1.12	10.00±0.08	265±11	Wilson et al. (2008)
Mrk 231	146.46±4.28	25.12±0.65	583±23	Wilson et al. (2008)
Arp 193	37.13±1.57	25.12±0.42	148±7	Wilson et al. (2008)
Mrk 273	85.47±2.58	31.62±1.00	270±12	Wilson et al. (2008)
NGC 6240	43.92±1.75	79.43±1.70	55±3	Wilson et al. (2008)
IRAS 17208-0014	158.54±10.52	50.12±3.46	316±30	Wilson et al. (2008)
IRAS 00057+4021	24.12±1.35	15.85±0.83	152±12	Leech et al. (2010)
IRAS 01077-1707	34.45±1.53	25.12±2.45	137±15	Leech et al. (2010)
III Zw 35	25.94±0.75	12.59±1.50	206±25	Leech et al. (2010)

Table 2.5 (Continued.)

Source	$L_{\rm FIR}$	$L'_{\rm CO(3-2)}$	SFE	ref.
(1)	(2)	(3)	(4)	(5)
	[10^{10} $L_\odot$]	[10^8 K km s^{-1}]	[$L_\odot$ (K km s^{-1} pc^2)$^{-1}$]	
Mrk 1027	18.17±0.71	50.12±2.04	36±2	Leech et al. (2010)
IRAS 02483+4302	47.03±2.45	12.59±1.54	374±50	Leech et al. (2010)
IRAS 04232+1436	117.76±5.77	100.00±12.00	118±15	Leech et al. (2010)
IRAS 10039-3338	30.74±1.37	15.85±0.62	194±12	Leech et al. (2010)
IRAS 10190+1322	79.00±19.20	50.12±5.35	158±42	Leech et al. (2010)
IRAS 10565+2448	83.43±3.49	39.81±1.26	210±11	Leech et al. (2010)
IRAS 13001-2339	24.01±1.93	15.85±0.54	151±13	Leech et al. (2010)
NGC 5256	20.87±1.27	25.12±2.66	83±10	Leech et al. (2010)
Mrk 673	21.54±1.64	19.95±2.96	108±18	Leech et al. (2010)
IRAS 14348-1447	167.73±13.15	100.00±10.31	168±22	Leech et al. (2010)
Mrk 848	46.69±1.85	25.12±1.39	186±13	Leech et al. (2010)
NGC 6090	20.77±0.85	39.81±1.55	52±3	Leech et al. (2010)
IRAS 17132+5313	53.61±1.97	25.12±5.02	213±43	Leech et al. (2010)
IRAS 20010-2352	37.06±2.13	31.62±2.70	117±12	Leech et al. (2010)
II Zw 96	45.26±1.77	31.62±1.98	143±11	Leech et al. (2010)
		—— spiral galaxies ——		
NGC 0628	0.35±0.07	0.52±0.10	68±19	Wilson et al. (2012)
NGC 0925	0.20±0.04	0.09±0.02	227±68	Wilson et al. (2012)
NGC 2403	0.12±0.02	0.17±0.03	72±19	Wilson et al. (2012)
NGC 2976	0.05±0.01	0.05±0.01	105±27	Wilson et al. (2012)
NGC 3031	0.25±0.05	0.10±0.04	251±109	Wilson et al. (2012)
NGC 3034	3.98±0.80	3.98±0.04	100±20	Wilson et al. (2012)
NGC 3049	0.25±0.05	0.13±0.03	200±58	Wilson et al. (2012)
NGC 3184	0.40±0.08	1.00±0.15	40±10	Wilson et al. (2012)
NGC 3198	0.40±0.08	0.63±0.10	63±16	Wilson et al. (2012)
NGC 3351	0.50±0.10	0.50±0.06	100±23	Wilson et al. (2012)
NGC 3521	1.00±0.20	2.00±0.13	50±11	Wilson et al. (2012)
NGC 3627	1.58±0.32	3.16±0.17	50±10	Wilson et al. (2012)
NGC 3773	0.03±0.01	0.02±0.00	126±40	Wilson et al. (2012)
NGC 3938	0.79±0.16	1.26±0.20	63±16	Wilson et al. (2012)
NGC 4236	0.02±0.00	0.05±0.01	32±11	Wilson et al. (2012)
NGC 4254	3.16±0.63	7.94±0.52	40±8	Wilson et al. (2012)
NGC 4321	2.51±0.50	5.01±0.49	50±11	Wilson et al. (2012)
NGC 4450	0.13±0.03	0.10±0.03	126±43	Wilson et al. (2012)
NGC 4559	0.25±0.05	0.20±0.04	126±37	Wilson et al. (2012)
NGC 4569	1.00±0.20	2.00±0.17	50±11	Wilson et al. (2012)

Table 2.5 (Continued.)

Source	$L_{\rm FIR}$	$L'_{\rm CO(3-2)}$	SFE	ref.
(1)	(2)	(3)	(4)	(5)
	$[10^{10}\ L_\odot]$	$[10^8$ K km s$^{-1}]$	$[L_\odot$ (K km s^{-1} pc$^2)^{-1}]$	
NGC 4579	0.63±0.13	0.79±0.14	79±21	Wilson et al. (2012)
NGC 4625	0.03±0.01	0.01±0.00	200±64	Wilson et al. (2012)
NGC 4631	1.26±0.25	1.58±0.08	79±16	Wilson et al. (2012)
NGC 4736	0.50±0.10	0.50±0.04	100±21	Wilson et al. (2012)
NGC 4826	0.63±0.13	1.00±0.05	63±13	Wilson et al. (2012)
NGC 5033	1.58±0.32	2.51±0.33	63±15	Wilson et al. (2012)
NGC 5055	1.00±0.20	2.00±0.17	50±11	Wilson et al. (2012)
NGC 5194	1.58±0.32	5.01±0.19	32±6	Wilson et al. (2012)

Notes. (2): FIR luminosity based on the *AKARI*/FIS BSC (Section 2.3). The "–" sing means VLA non-detected galaxies of early stage. The "‡" sign means that the galaxy is not listed in the *AKARI*/FIS BSC. We use FIR luminosities in referred paper (ref.) instead. (5):The reference of $L'_{\rm CO(3-2)}$, Wilson et al. (2008), Leech et al. (2010) or Wilson et al. (2012)

2.6 Results and discussions

2.6.1 *Relation between $L_{\rm FIR}$ and $L'_{\rm CO(3-2)}$*

A linear relation (slope $\alpha \sim 1$, $\log L_{\rm FIR} = \alpha \log L'_{\rm CO(3-2)} + \beta$) between $L'_{\rm CO(3-2)}$ and $L_{\rm FIR}$ was suggested in previous studies (e.g.,Greve et al. (2014) and references therein). Here, I investigate the variation in the $L'_{\rm CO(3-2)}$ –$L_{\rm FIR}$ correlation as a function of merger stage, and the results are presented in Figure 2.7. I conducted log-linear fitting and derive the indices α and β.

$$\begin{aligned} &\text{(for all sample sources)} \\ &\log L_{\rm FIR} = 1.10_{\pm 0.07} \log L'_{\rm CO(3-2)} + 1.15_{\pm 0.40} \\ &\mathrm{r} = 0.95 \end{aligned} \tag{2.10}$$

Before determining the weighted sum of squared residuals, the $L^{\rm err}_{\rm FIR}$ and $I^{\rm err}_{\rm CO}$ are reflected on the relative weight of each data point. The correlation coefficient

$r_{xy} = \frac{\Sigma(x_i-\bar{x})(y_i-\bar{y})}{\sqrt{\Sigma(x_i-\bar{x})^2(y_i-\bar{y})^2}}$ (where x is $\log L'_{\rm CO(3-2)}$ and y is $\log L_{\rm FIR}$) evaluates the strength of the correlation between two variables. The slope of $\alpha = 1.10 \pm 0.07$ is slightly larger than the linear relation obtained for U/LIRGs ($\alpha = 0.99 \pm 0.04$, Greve et al. (2014)). The spiral galaxies with low FIR luminosity ($L_{\rm FIR} \sim 10^9 L_\odot$) have systematically lower $L'_{\rm CO(3-2)}$. Since the CO luminosity may systematically underestimate the molecular hydrogen gas mass in lower metallicity galaxies, such systematic offset might be due to lower metallicities in lower mass (i.e., less luminous) galaxy (Wilson et al. , 2012) and/or low excitation condition (i.e., small CO (3–2)/CO (1–0) ratio)

2.6.2 *Evolution of mergers in the* $\log L'_{\rm CO(3-2)}$–$\log L_{\rm FIR}$ *plane*

I independently derive the slope α for late stage mergers, early stage mergers, and spiral galaxies (Figure 2.8).

(for spirals)

$$\log L_{\rm FIR} = 0.79_{\pm 0.04} \log L'_{\rm CO(3-2)} + 3.50_{\pm 0.24} \quad (2.11)$$

$r = 0.95$

(for early stage mergers)

$$\log L_{\rm FIR} = 1.08_{\pm 0.14} \log L'_{\rm CO(3-2)} + 1.18_{\pm 0.61} \quad (2.12)$$

$r = 0.87$

(for late stage mergers)

$$\log L_{\rm FIR} = 1.12_{\pm 0.16} \log L'_{\rm CO(3-2)} + 1.00_{\pm 0.65} \quad (2.13)$$

$r = 0.88$

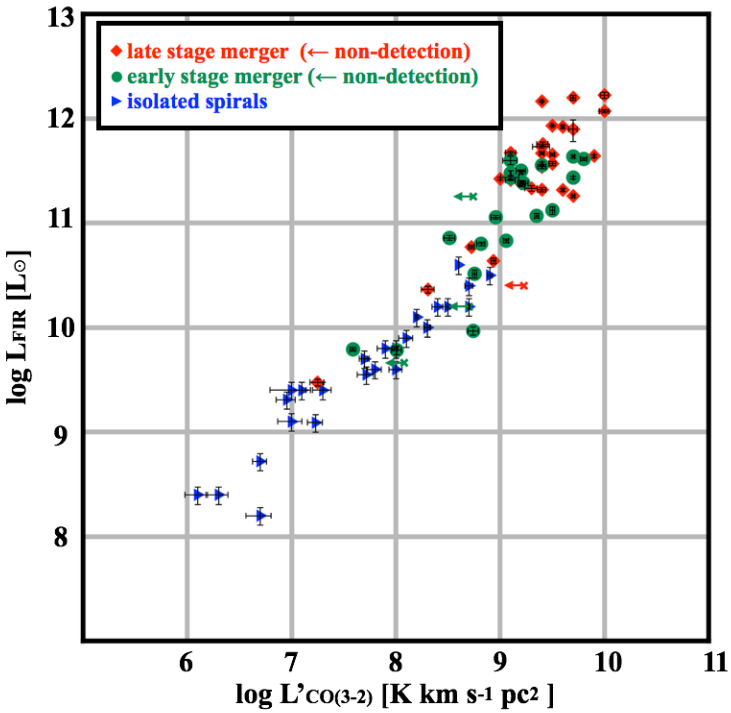

Figure 2.7 Relation between $L_{\rm FIR}$ and $L'_{\rm CO(3-2)}$. The symbols colored in green, red, and blue represent early stage mergers, late stage mergers, and isolated spiral galaxies, respectively. The arrows represent the 3σ upper limit of the CO (3–2) luminosity for the ASTE non-detected sources. Galaxies that are not detected in both the CO (3–2) and 1.5 GHz continuum emission are not shown here.

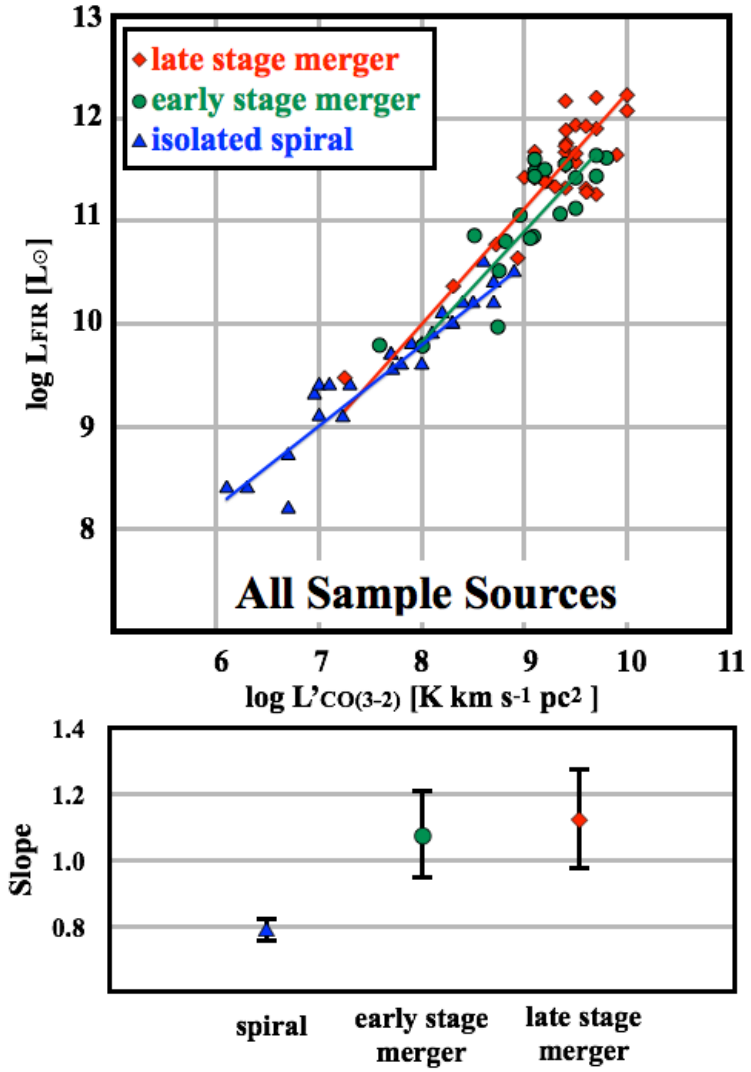

Figure 2.8 (*Top*) Relation between $L'_{\mathrm{CO(3-2)}}$ and L_{FIR}. The best-fit functions are shown in colored lines. (*Bottom*) the difference of slope between early stage mergers, late stage mergers, and isolated spiral galaxies with the fitting errors are presented. Galaxies that are not detected in the CO (3–2) are not shown here.

(for all mergers)

$$\log L_{\rm FIR} = 1.10_{\pm 0.07} \log L'_{\rm CO(3-2)} + 1.15_{\pm 0.40} \qquad (2.14)$$

$$\mathrm{r} = 0.85$$

I find the various slope α between isolated galaxies and mergers (as a whole) (α = $0.79 \pm 0.04,\ 1.08 \pm 0.14,\ 1.12 \pm 0.16$ for spirals and early- and late-stage mergers, respectively). This can also appear in the relation between $L_{\rm FIR}$ and SFE (Figure 2.9), which means that the SFE of spiral galaxies decreases as a function of $L_{\rm FIR}$ whereas merging galaxies show a contrary trend. I note that Iono et al. (2009) show no strong evidence between $L_{\rm FIR}$ and SFE, this should be due to the lack of galaxies with $10^{10} L_{\odot} < L_{\rm FIR} < 10^{11} L_{\odot}$.

2.6.3 *The effect of AGNs to the $L'_{\rm CO(3-2)}$–$L_{\rm FIR}$ relation*

For some U/LIRGs, we can not ignore the contribution of the AGNs to the FIR luminosity (Sanders & Mirabel , 1996), and the exact fraction of the AGN contribution varies from source by source (Armus et al. , 2007). In the case of Mrk 231, the nuclear starburst contributes 25-40% of the bolometric luminosity. On the other hand, Ichikawa et al. (2014) suggest that the AGN contribution of $\sim$ 20% in ULIRGs, which suggests starburst activity is the main power sources of IR luminosities. In this project, we select AGN candidates and measure the star formation relation excluding candidates in order to check the effect of AGN in a discussion. We identify twelve sources based on the classification scheme using *Wide-field Infrared Survey Explorer* (*WISE*, Wright et al. , 2010) 22″aperture photometry color of our sample sources (table 2.6) (Jarrett et al. , 2011; Mateos et al. , 2012; Stern et al. , 2012) (Figure 2.10). Excluding these candidates, the

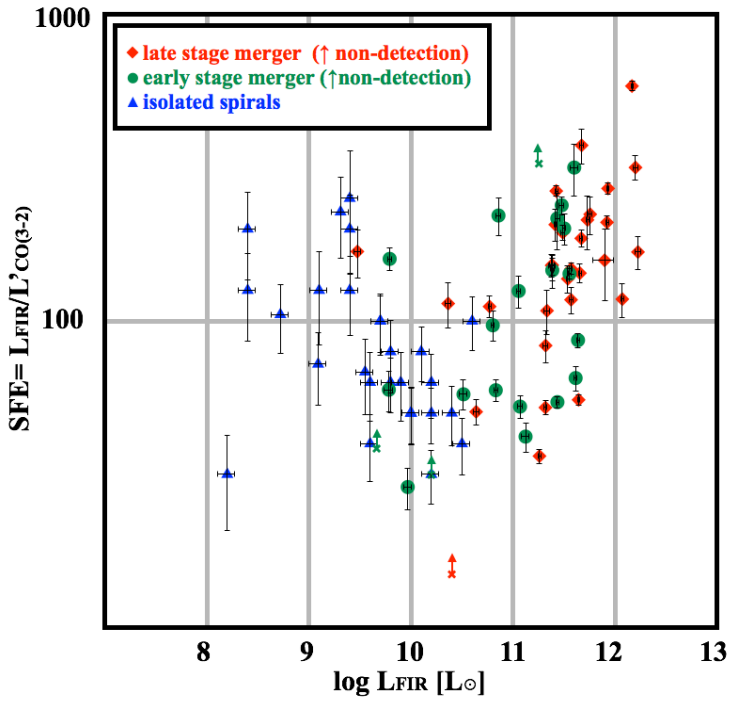

Figure 2.9 Relation between $L_{\rm FIR}$ and SFE.The symbols and the colors are the same as figure 2.7. The arrows represent the lower limit of SFE for the ASTE non-detected sources. Galaxies that are not detected in both the CO (3–2) and 1.5 GHz continuum emission are not shown here.

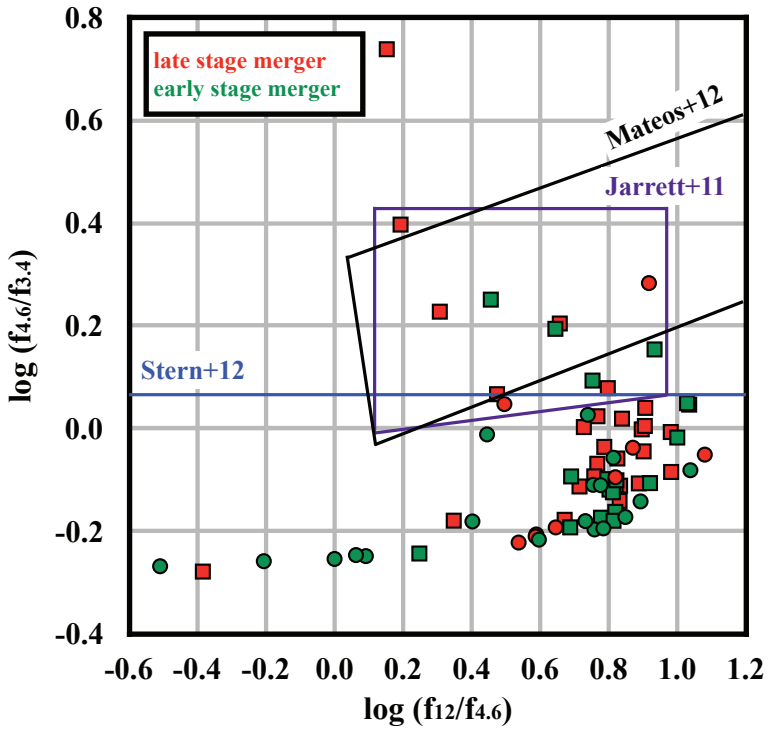

Figure 2.10 WISE color-color diagram. Green and red symbols represent the early and late stage mergers. The region enclosed by the lines show the criteria for AGN candidates; Jarrett et al. (2011) (purple), Stern et al. (2012) (blue), and Mateos et al. (2012) (black).

relation between $L'_{\mathrm{CO(3-2)}}$ and L_{FIR} becomes,

$$\begin{aligned} &\log L_{\mathrm{FIR}} = 1.11_{\pm 0.12}\ \log L'_{\mathrm{CO(3-2)}} + 1.05_{\pm 0.55} \\ &\mathrm{r} = 0.87 \end{aligned} \tag{2.15}$$

for the early stage mergers, and

$$\begin{aligned} &\log L_{\mathrm{FIR}} = 1.10_{\pm 0.15}\ \log L'_{\mathrm{CO(3-2)}} + 1.15_{\pm 0.63} \\ &\mathrm{r} = 0.88 \end{aligned} \tag{2.16}$$

for the late stage mergers (Figure 2.11). There is little difference between the relation here and those derived in section 2.6.2 (Figure 2.8). We conclude that the effect of the AGN is negligible in the FIR luminosity.

Table 2.6: WISE color

Source	$\log(f_{12}/f_{4.6})$	$\log(f_{4.6}/f_{3.4})$
—— early stage merging galaxies ——		
VV 081a	0.31	0.54
VV 081b	5.73	0.64
VV 122a	7.81	0.72
VV 122b	7.05	0.67
VV 217a	1.23	0.56
VV 217b	0.62	0.55
VV 242a	5.68	0.78
VV 242b	3.94	0.61
VV 272a	5.39	0.66
VV 272b	1.15	0.57
VV 352a	6.08	0.64
VV 352b	10.92	0.83
VV 729a	1.00	0.56
VV 729b	2.52	0.66
VV 731a	6.51	0.88
VV 731b	5.48	1.06
VV 830a	2.78	0.97
VV 830b	5.97	0.78
Arp 299W*	0.93	0.15

Source	$\log(f_{12}/f_{4.6})$	$\log(f_{4.6}/f_{3.4})$
Arp 299E*	0.46	0.25
NGC 5257W	0.78	-0.17
NGC 5257E	0.82	-0.16
NGC 5331N	0.69	-0.19
NGC 5331S	0.80	-0.12
Arp 236W*	0.64	0.19
Arp 236E*	0.75	0.09
UGC 2369N	0.25	-0.24
UGC 2369S	1.00	-0.02
Arp 55E	0.80	-0.10
Arp 55W	0.82	-0.11
Arp 238E	1.03	0.05
Arp 238W	0.81	-0.12
Arp 302N	0.69	-0.09
Arp 302S	0.81	-0.18
NGC 6670E	0.92	-0.11
NGC 6670W	0.82	-0.10
—— late stage merging galaxies ——		
AM 2038-382	0.54	-0.22
Arp 187	0.59	-0.21
Arp 230	0.59	-0.21
ESO 286-IG019*	0.92	0.28
IRAS F16399-0937	0.82	-0.09
NGC 1614	1.08	-0.05
NGC 7252	0.65	-0.19
UGC 6*	0.50	0.05
NGC 2623	0.77	0.02
Mrk 231*	0.31	0.23
Arp 193	0.90	-0.00
Mrk 273*	0.66	0.20
NGC 6240	0.73	0.00
IRAS 17208-0014	0.84	0.02
IRAS 00057+4021	0.78	-0.19
IRAS 01077-1707	0.89	-0.11
III ZW35	0.79	-0.04
Mrk 1027	0.83	-0.11
IRAS 02483+4302	0.35	-0.18
IRAS 04232+1436	0.77	-0.07
IRAS 10039-3338*	0.15	0.74
IRAS 10190+1322	0.82	-0.06

Source	$\log(f_{12}/f_{4.6})$	$\log(f_{4.6}/f_{3.4})$
IRAS 10565+2448	0.91	0.04
IRAS 13001-2339	0.71	-0.11
NGC 5256	0.76	-0.09
Mrk 673	0.67	-0.18
IRAS 14348-1447*	0.80	0.08
Mrk 848	0.98	-0.01
NGC 6090	0.98	-0.08
IRAS 17132+5313	0.90	-0.04
IRAS 20010-2352*	0.47	0.07
II ZW 96	1.03	0.05
NGC 828	0.83	-0.14
UGC 5101*	0.19	0.40
NGC 4194	-0.38	-0.28

2.6.4 Global star formation relation from GMA scale to high-z galaxies

Using the molecular gas observations in distant galaxies (Carilli & Walter , 2013; Casey et al. , 2014), I investigate the $L'_{\rm CO}$ and $L_{\rm FIR}$ relation for different star forming environments (e.g., normal star formation in isolated spirals and extreme starburst in SMGs). I use CO (3–2) information of normal high-z star forming galaxies from Tacconi et al. (2013) and SMGs/QSOs from Solomon & Vanden Bout (2005); Bothwell et al. (2013). For the giant molecular association (GMA; sub-kpc) scale star forming region, I use the ASTE on-the-fly CO (3–2) images of NGC 628, NGC 7793 (Muraoka et al. , 2016), and M 83 (Muraoka et al. , 2007). Figure 2.12 show the comparison with GMAs, high-z sources, and our sample sources. I obtained a linear relation ($\log L_{\rm FIR} = 1.0\ \log L'_{\rm CO(3-2)} + 2.0$) across six orders of magnitude in the CO (3–2) luminosity, which is consistent with the global linear relation in previous studies (e.g., Greve et al. , 2014). However, I find relationships which are different among the population. For example, nearby late stage mergers (red diamonds) and high-z SMG/QSOs (gray triangles) are systematically higher than the global fit, and the high-z normal star forming galaxies (Tacconi et al.

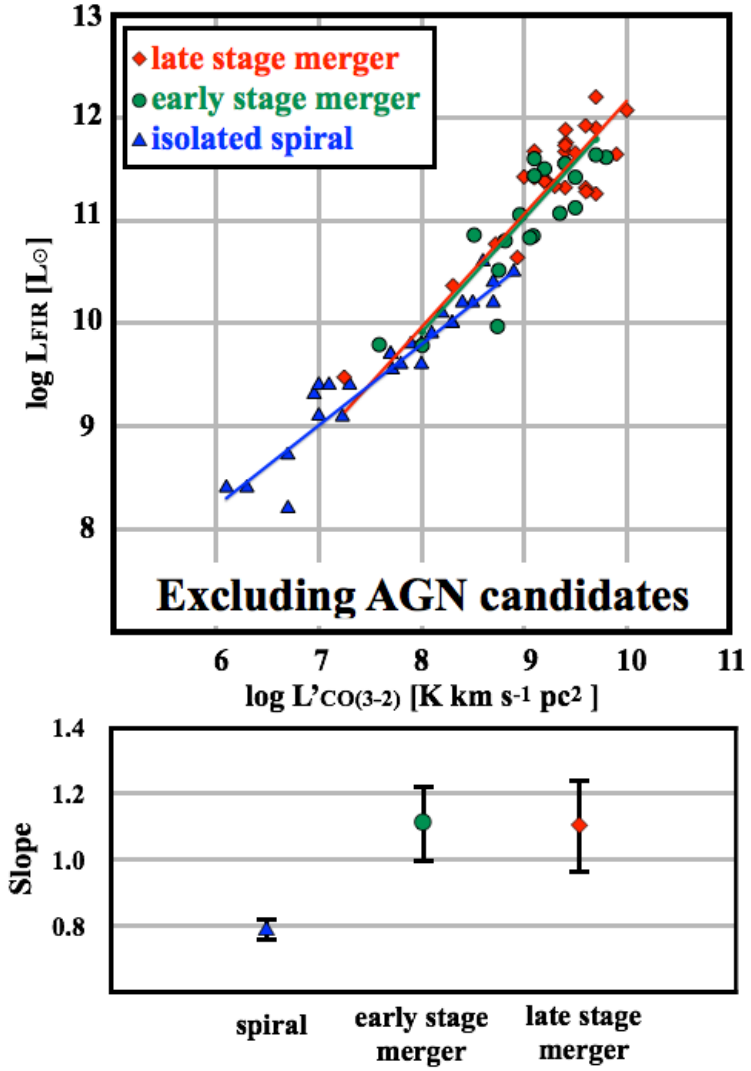

Figure 2.11 (*Top*) Relation between $L'_{\mathrm{CO(3-2)}}$ and L_{FIR} excluding AGN candidates. The best-fit functions are shown in colored lines. Galaxies that are not detected in the CO (3–2) are not shown here. (*Bottom*) the difference of slope between early stage mergers, late stage mergers, and isolated spiral galaxies with the fitting errors are presented.

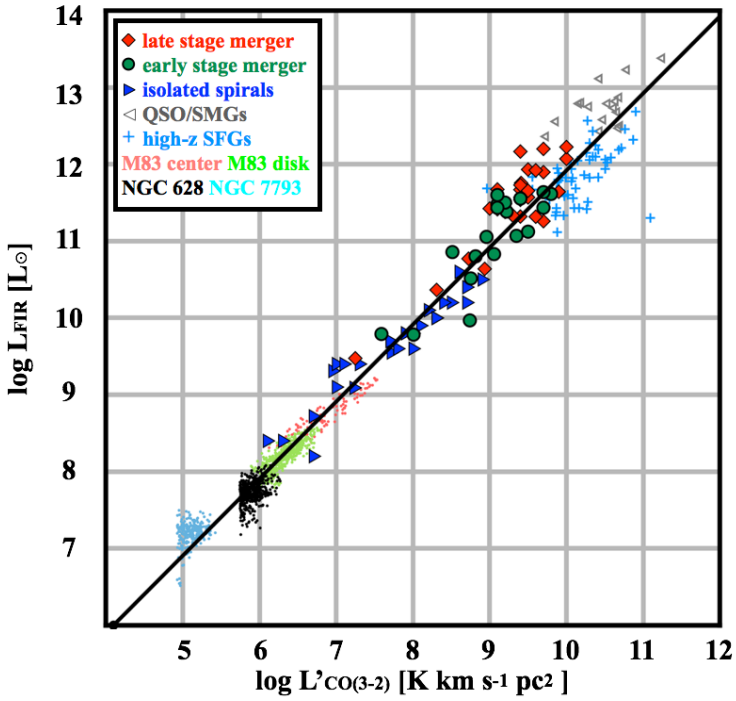

Figure 2.12 Comparison of high-z normal star forming galaxies (cyan crosses; Tacconi et al. , 2013) and SMGs/QSOs (grey triangles; Bothwell et al. , 2013; Solomon & Vanden Bout , 2005) in FIR-CO plane. The GMAs in (Muraoka et al. , 2016) are shown as small dots. The line shows the non-weighted least-square results for all sources ($L_{\rm FIR} = 1.0\ \log L'_{\rm CO(3-2)} + 2.0$). We note the possibility of a systematic uncertainty for deriving FIR luminosity of sample sources. For example, we derived FIR luminosity of sample sources in Tacconi et al. (2013) from their SFR by assuming SFR $[M_\odot\ {\rm yr}^{-1}] = 4.5 \times 10^{44}\ L_{\rm FIR}$ (Mo et al. , 2010). In addition, the FIR luminosity of sample sources in Muraoka et al. (2016) is measured by assuming $L_{\rm IR} = 1.3 L_{\rm FIR}$.

, 2013) are lower on average. This possibly suggests that a single global relation cannot explain the star formation from GMA scale to high-z galaxies. I note that FIR luminosities for high-z normal star forming galaxies possibly have systematical error since the FIR luminosity is derived from SFR measured by various tracers (e.g., Hα, UV, 24 μm). Tacconi et al. (2013) mention that systematic error is $\pm$35%.

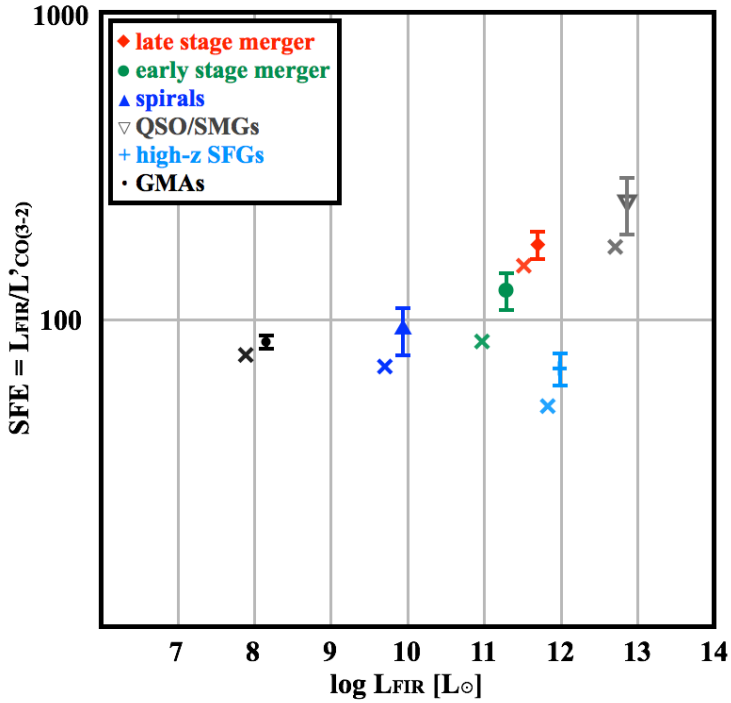

Figure 2.13 The relation between FIR-SFE for average value (median values are plotted as crosses). The error bars are calculated as a standard error.

In addition, I found the gradual increase of the average SFE from isolated galaxies, merging galaxies, and to high-z SMG/QSOs (Figure 2.13). This suggests ongoing efficient star formation in high-z SMG/QSOs possibly due to gas rich major mergers. I note that evolution of the SFE seen in Figure 2.13 might be due to the enhancement of FIR luminosity by AGN, especially, in high-z SMG/QSOs. It is necessary to quantify the AGN contribution for the high-z sources in the future. On the other hand, the smaller SFE in high-z normal star forming galaxies (light blue) might suggest a long lasting star formation like nearby isolated spiral galaxies.

Finally, I mention issues about CO excitation and CO to H_2 conversion factor. It is said that merging galaxies have higher CO (3–2)/CO(1–0) ratio than normal

spiral galaxies and the ratio increase as a merger process proceeds (Leech et al. , 2010). In addition, Bolatto et al. (2013b) show that CO-to-H_2 conversion factor is different for merging ULIRGs ($\sim 0.8\ M_\odot$ (K kms^{-1} pc^2)$^{-1}$) and normal galaxies ($\sim 4.2\ M_\odot$ (K kms^{-1} pc^2)$^{-1}$). This means that the conclusions based on $L'_{\rm CO} - L_{\rm FIR}$ plane become more robust on $M_{\rm H_2} - SFR$ plane.

2.6.5 *Suggestions for merger induced star formation*

The global properties of our observed galaxies support the merger model suggested by Teyssier et al. (2010); Bournaud (2011); Powell et al. (2013) in which mergers fill the gap between disk and starburst sequence. These simulations are consistent with our observation as well as the independent observational results of dense gas tracers (e.g., HCN and HCO^+) toward interacting systems, showing that dense gas is ubiquitous across the merging interface between the two interacting galaxies (e.g., Iono et al. (2013); Saito et al. (2015)). The next step is to understand the small scale physics to characterize the global properties. For example, Teyssier et al. (2010); Bournaud (2011) emphasizes the importance of the fragmentation of high-dispersion gas both around the central nucleus as well as in the extended disk in mid-stage mergers. They also argue that the same process is important in late stage mergers.

2.7 Chapter Summary

I conducted ASTE CO (3–2) observations toward 19 early and 7 late stage merging galaxies. Including supplemental data, we investigate the CO (3–2) and FIR luminosity of 29 early stage merging galaxies, 31 late stage merging galaxies, and 28 isolated spiral galaxies. The main findings are as follows;

- There is correlation between CO (3–2) luminosity and FIR luminosity in the case of both spirals and mergers (figure 2.7). I find that spiral galaxies and

merging galaxies has different slope in the $\log L'_{\mathrm{CO(3-2)}}$–$\log L_{\mathrm{FIR}}$ plane, $\alpha \sim 0.79$ for isolated spiral galaxies and $\alpha \sim 1.12$ for merging galaxies (figure 2.8). An obvious bi-modality is not seen in the $\log L'_{\mathrm{CO(3-2)}}$–$\log L_{\mathrm{FIR}}$ since mergers fill the gap between disk and starburst sequence.

- I find a positive correlation between FIR luminosity and SFE in merging galaxies. This correlation is not seen in previous observation of merging galaxies (e.g., Iono et al. , 2009) due to lack of the FIR faint sources.

- I find the increase of the average SFE from isolated spiral, merging galaxies to active high-z galaxies (SMGs/QSOs).

- Our observations can be explained by the models which predict (1) inefficient starbursts triggered by disk-wide dense clumps formed in the early stage of interaction and (2) efficient starbursts triggered by central global gas inflow occur in the final stage for each galaxies. The next step is to show the evidences of these phenomena in individual galaxies.

3 | True star formation without dust extinction in NGC 3256

3.1 Science Goal

In chapter 2, I investigated the relation between global CO and FIR luminosity in merging galaxies. However, the information obtained from global properties is limited, and it is difficult to elicit complex phenomena during a merger process. Especially, it is necessary to investigate spatial distribution of SFR and molecular gas (e.g., Espada et al. , 2012) in order to understand where starbursts are triggered during a merger process. In this chapter, I focus on the star formation activity in a merging galaxy.

The classical idea of merger induced star formation activity is nuclear starbursts taking place in the central region ($<$ 1 kpc) (e.g., Keel et al. , 1985). Nuclear starbursts are triggered by a massive gas inflow toward the central region. Barnes (2004) recognized the spatially extended star formation activity in a merging galaxy Mice. Subsequently, observational evidences for spatially extended star formation activity were reported in e.g., Antennae galaxy (Wang et al. , 2004), Arp 140 (Cullen et al. , 2007), NGC 2207+IC 2163 (Elmegreen & Elmegreen , 2005). Recently, using optical integral field unit observation, Cortijo-Ferrero et al. (2017) investigated the star formation history of early stage mergers, and showed that extended starbursts arise in the early stages mergers. Nuclear starbursts occur later, in the more advanced stages of the merger. However, the conclusion of "spatially extended starburst" is probably because the unveiling dust-enshrouded nuclear star-

burst. It is necessary to investigate the dusty nuclear starbursts and spatially extended starbursts in a consistent manner .

In order to show a conclusive evidence for the importance of spatially extended starburst against nuclear activity, I use both optical and millimeter/sub- millimeter (mm/sub-mm) hydrogen recombination lines. At first, mapping of nebulae emission line (i.e., Hα and Hβ) by optical integral field unit (IFU) enables us to investigate spatial distribution of star formation activity without strong dust extinction. However, it is difficult to quantify “true" star formation activity in dusty merging galaxies.

One of the best methods to investigate the properties of star forming region in extremely dusty area is the recombination lines in mm/sub-mm (Scoville & Murchikova , 2013). Recently, ALMA has detected recombination lines from nearby galaxies; e.g., NGC 253 (Bendo et al. , 2015), NGC 4945 (Bendo et al. , 2016), and NGC 5253 (Bendo et al. , 2017). By cross-checking SFR measurements from the other wavelength, they demonstrate ALMA is effective to study the starburst activity in a dusty region. I apply this method to investigate the properties of HII regions associated with dusty starburst region in dusty merging U/LIRGs. Little has been reported on the observations of mm/sub-mm recombination lines in U/LIRGs. For example, in the case of Arp 220, Anantharamaiah et al. (2000) have detected H167α, H165α, H92α, H42α, H40α, and H31α by using Very Large Arry (VLA) and IRAM 30m telescope, and they suggest multiple starbursts. In terms of the ALMA study of recombination lines towards merging LIRGs, Scoville et al. (2015) look for the H26α emission from Arp 220, but detection is not clear due to the contamination of nearby HCN(4–3) line. In this chapter, I present observations of Hα, Hβ, H40α and H42α emission in one merging galaxy NGC 3256, and reveal the true star formation activity.

3.2 ALMA

The Atacama Large Millimeter/submillimeter Array (ALMA)[1] is an interferometer consisting of 66 antennas (12-m and 7-m) located on the Chajnantor plateau at 5000m altitude (Figure 3.1). The baselines can be up to 16 km. Additional compact configurations are accessible for spatially extended targets. In the case of the targets with large scale structure of which 12-m array can not recover well, it is possible to use Atacama Compact Array (ACA) which consists of of twelve 7-m antennas and four 12-m antennas. The observable frequency coverage depends on the receivers, ranging from Band3 (starting at $\sim$ 84 GHz) to Band10 (ending at $\sim$ 950 GHz). The field of view is determined by the size of individual antennas and the observing frequency, and generally the full width at half maximum (FWHM) of the primary beam is used to describe the diameter of the field of view. For example, the field of view is $\sim$ 19" at 300 GHz for 12-m array and 35" for 7-m array. The angular resolution depends on the observing configuration and frequency. In the case of the most compact configuration ($\sim$ 160 m), the spatial resolution is $\sim$ 0.5" at $\sim$ 950 GHz and $\sim$ 4.8" at 110 GHz. In the case of the most extended configuration ($\sim$ 16 km), the spatial resolution is $\sim$ 0.020" at $\sim$ 230 GHz to $\sim$ 0.043" at 110 GHz. The resolution in arcsec can be approximated as

$$FWHM(") = 76/(\text{maximum baseline (km)})/(\text{frequency (GHz)}). \tag{3.1}$$

The noise revel in the data cubes (S) is roughly proportional to

$$S \propto (k * T_{\rm sys})(A * N^2 * (N_p * \Delta v * \Delta \tau)^{0.5})^{-1} \tag{3.2}$$

[1] https://almascience.org/about-alma/alma-basics

where k is Boltzmann constant, T_{sys} is the system temperature, A is the effective surface area of each antenna, N is the number of antennas, N_p is the number of polarizations, Δv is the available bandwidth (is 7.5 GHz for continuum observation and channel width for spectral line observations) and $\Delta\tau$ is the integration time. *Common Astronomy Software Applications* package (`CASA`) (McMullin et al. , 2007) has been developed to support the data processing of the radio astronomical telescopes such as ALMA and VLA. I use `CASA` for the data analysis in this thesis for ALMA data.

Figure 3.1 The outside appearance of ALMA.

3.3 NGC 3256

NGC 3256 is a merging LIRG with a FIR luminosity of $L_{\rm FIR} = 10^{11.43}\ L_{\odot}$, and the luminosity distance of $D_L = 35$ Mpc (Sanders et al. , 2003). Since NGC 3256 is one of the brightest galaxies within ~ 40 Mpc, it is an ideal target source for a case study. As shown in Figure 3.2(a) and (b), there are two long tidal tails of stars and HI gas (e.g., English et al. , 2003), which are clear evidences of a galaxy-galaxy interaction. In the context of selection criteria in chapter 2, NGC 3256 is

a late stage merger since the optical DSS image shows single nucleus. However, this galaxy consists of two galaxies and has two distinct northern and southern nuclei separated by $\sim$ 5" ($\sim$ 850 pc), identified by X-ray, IR, and radio emissions. A schematic picture is shown in Figure 3.3. In addition, SFE $[L_{\odot}] = L_{\rm FIR}/L'_{\rm CO} \sim$ 40 (K km s^{-1} pc^2)$^{-1}$ (Sargent et al. , 1989) is lower compared to the average value of SFE seen in merging galaxies (Michiyama et al. , 2016). Therefore, NGC 3256 can be a transient phase from early stage to late stage in a merger process.

Ohyama et al. (2015) found that the primary heating source is likely related to starburst activity at the northern galaxy, and a low-luminosity AGN is believed to be the dominant source of the far-infrared luminosity at the southern galaxy. The star formation activities associated with modest dust obscured regions were investigated with optical spectroscopy (Lípari et al. , 2000). They suggest that the nuclear starburst and extended HII region at the spiral arms have similar properties (e.g., electron temperature $T_{\rm e} \sim$ 6000-7000 K, and electron density $n_{\rm e} \sim 100-1000$ cm^{-3}). In order to investigate the dusty HII region associated with the southern nucleus, Piqueras López et al. (2012, 2013) observed infrared recombination lines in NGC 3256. They show that the southern nucleus in NGC 3256 has a large dust extinction ($A_{\rm V} \sim 12$), and it is difficult to investigate the SFR of the dusty region even by using infrared spectroscopy.

Sakamoto et al. (2006) investigated the molecular gas distributions with SMA, and found a strong gas concentration toward the double nucleus. The other important finding is the high-velocity gas from the nuclei, where the galactic wind was identified by Na D absorption lines (Heckman et al. , 2000). Sakamoto et al. (2014) further investigate the molecular gas distribution by using ALMA and identified two molecular bipolar outflows from the two nuclei. One is the spatially extended starburst driven outflow around the northern nucleus, and the other is AGN driven

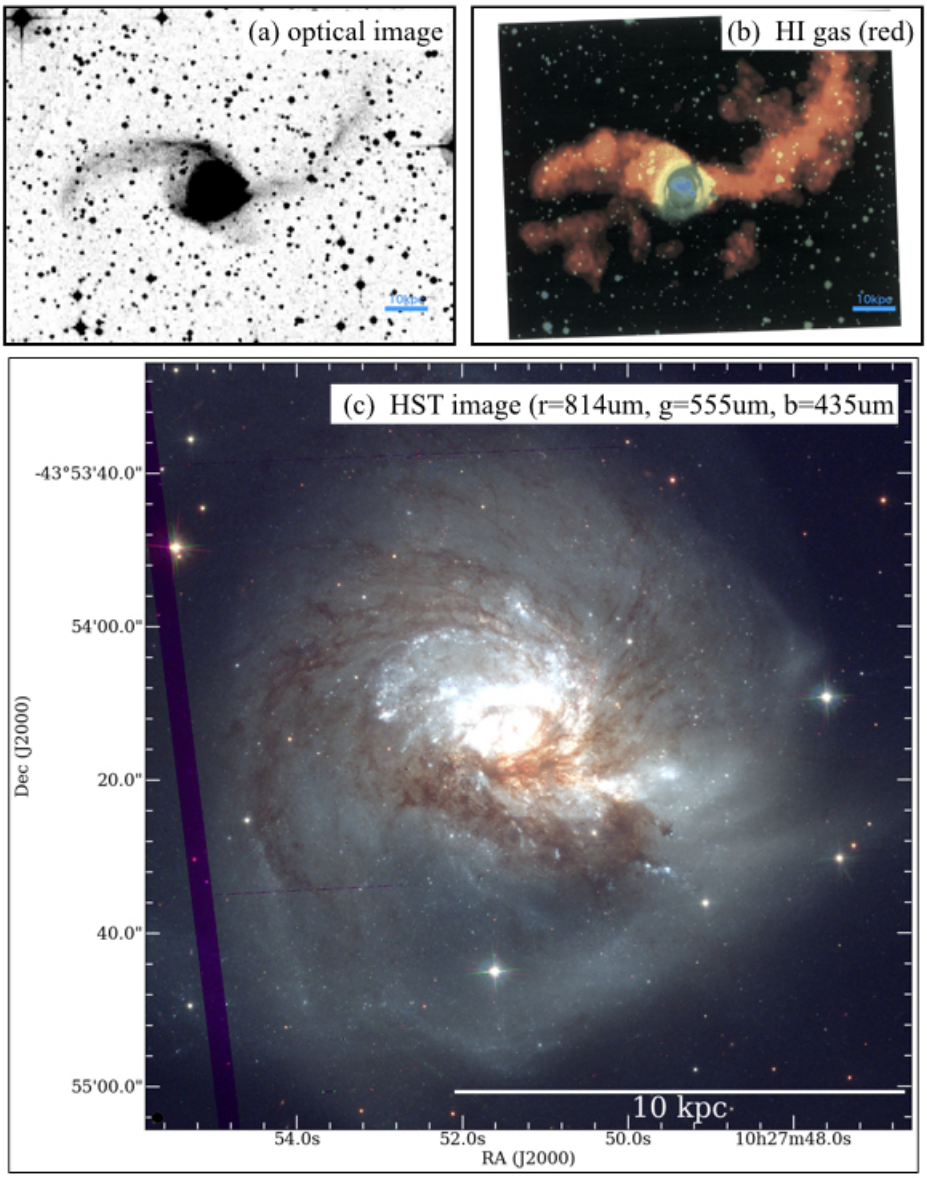

Figure 3.2 The images of NGC 3256. (a) The DSS red filter image shows the clear stellar tidal tail. (b) The red color shows the HI distribution, and there are HI tidal tails (English et al. , 2003). (c) The image obtained by HST. There is a face on blue spiral galaxy and an edge-on dusty galaxy.

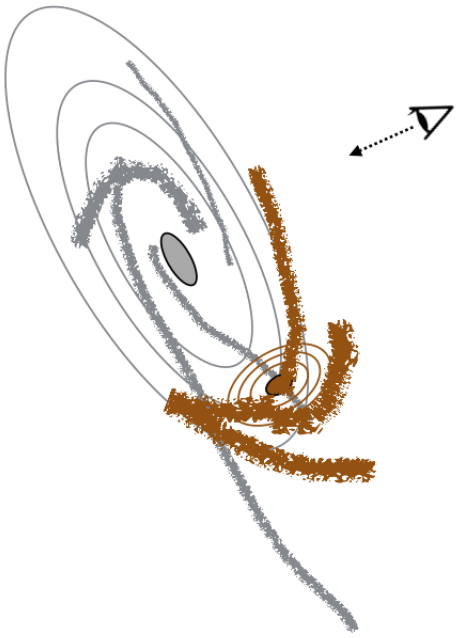

Figure 3.3 The schematic picture of the central part of NGC 3256 based on Sakamoto et al. (2014). There are a face-on spiral galaxy (north) and edge-on dusty galaxy (south).

collimated outflow around the southern nucleus. Therefore, NGC 3256 is a good laboratory to investigate the feedback mechanism during the merger process. I will investigate the molecular outflows in chapter 4.

3.4 Data

3.4.1 MUSE

I use IFU data obtained by Multi Unit Spectroscopic Explorer (MUSE). MUSE is a second generation instrument for the Very Large Telescope (VLT) of the European Southern Observatory (ESO). The data for NGC 3256 are obtained from ESO science archive portal[2]. Both Hα and Hβ are detected in the entire galaxy. I use Hβ map (Figure 3.4a) to avoid the contamination of NII lines around Hα emission. I use Hα and Hβ peak ratio $(\mathrm{H}\alpha/\mathrm{H}\beta)_{\mathrm{obs}}$ to make the dust extinction map (Figure 3.4b)

$$E(\mathrm{B}-\mathrm{V}) = -\frac{2.5}{k(\mathrm{H}\alpha)-k(\mathrm{H}\beta)} \log\left[\frac{(\mathrm{H}\alpha/\mathrm{H}\beta)_{\mathrm{obs}}}{(\mathrm{H}\alpha/\mathrm{H}\beta)_{\mathrm{model}}}\right]. \tag{3.3}$$

$k(\lambda)$ is the dust extinction curve and $k(\mathrm{H}\alpha)-k(\mathrm{H}\beta) = 1.163$ (Calzetti et al. , 2000). $(\mathrm{H}\alpha/\mathrm{H}\beta)_{\mathrm{model}}$ is 2.69 assuming case-B, $T_e = 5000$ K, and $n_e = 10^3$ cm^{-3}. The dust extinction magnitude

$$A_{\mathrm{V}} = R_{\mathrm{V}}\, E(\mathrm{B}-\mathrm{V}) \tag{3.4}$$

where $R_{\mathrm{V}} = 4.05$ for starburst galaxies (Calzetti et al. , 2000; Calzetti , 2013) (Figure 3.4b). The extinction corrected Hβ map is shown in Figure 3.4c.

3.4.2 ALMA

I use the ALMA data to obtain H40α, H42α and ^{13}CO (1–0) data cube and $\sim$ 99 GHz continuum image (Michiyama et al. , 2018; Harada et al. , 2018) (Ta-

[2] http://archive.eso.org/scienceportal/home

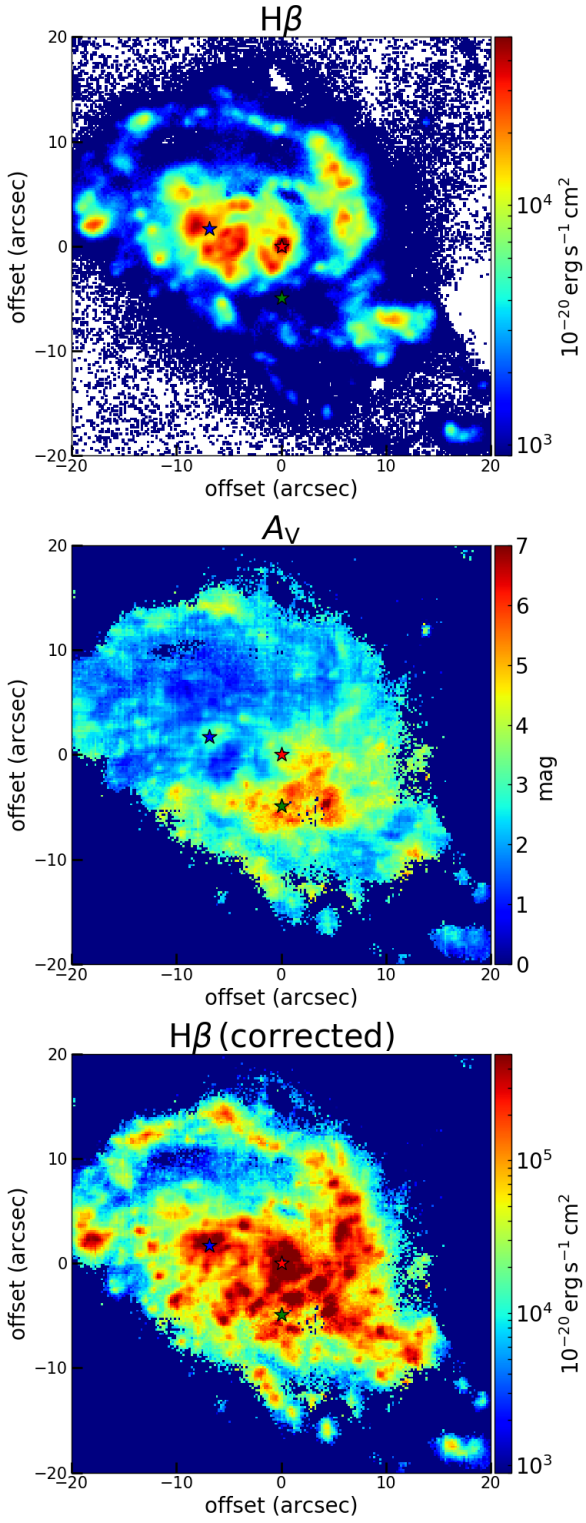

Figure 3.4 (a) Hβ map, (b) dust extinction map, and (c) dust extinction corrected Hβ map. The stars correspond to the position where H40α is detected (Section 3.4.2)

ble 3.1)[3]. For ALMA data, I follow the calibration method conducted by East Asian ALMA Regional Center. However, I have conducted additional reduction for band-edge flagging and flux scaling for the specific data (see Section 3.8). The data from three different projects have been combined to obtain the H40α image without any weighting for each observations. I subtract the continuum by using the uvcontsub task in CASA. The data cubes are made with a velocity resolution of 50 km s^{-1} using tclean task in CASA (version 5.1.2, Briggs weighting, robust = 2.0) with automatically masking loop auto-multithresh (sidelobethreshold=2.0, noisethreshold=2.5, lownoisethreshold=1.5, minbeamfrac=0.3, growiterations=75, and negativethreshold=0.0). I summarize the achieved angular resolution and sensitivity in Table 3.2.

Figure 3.5 show the (a1)-(a2) integrated intensity map, (b) channel map, and (c1)-(c3) spectrum of H40α. The same figures for H42α are shown in Figure 3.6. I use H40α line flux to derive physical parameters since the image quality (i.e., angular resolution and sensitivity) is better than H42α. In order to identify the HII region probed by H40α line, I use the imfit task in CASA and fit elliptical Gaussian components on the integrated intensity map. H40α blobs are detected at northern nucleus, southern nucleus, and dust lane that has a position offset from two nuclei with the signal to noise ratio of > 10, > 8, and > 4, respectively. The coordinates, line flux, and source size (FWHM major and minor axis) of detected blobs are shown in Table 3.3.

Figure 3.7 shows the spatial distribution of ^{13}CO (1–0) emission and 99 GHz continuum emission. Spatially extended structure is seen in both ^{13}CO (1–0) and 99 GHz continuum. In addition, both show the peak at the northern and southern nuclei and the arm where H40α emissions are detected.

[3]ALMA Project ID: 2015.1.00993.S, 2015.1.00412.S, and 2016.1.00965.S

Table 3.1 ALMA archive data used in this project

line	date	ALMA project ID	configuration
H40α	04 March 2016	2015.1.00993.S	C36-1/2
	07 March 2016	2015.1.00993.S	C36-1/2
	01 May 2016	2015.1.00412.S	C36-2/3
	28 May 2016	2015.1.00412.S	C40-3
	29 May 2016	2015.1.00412.S	C40-3
	29 October 2016	2016.1.00965.S	C40-6
H42α	04 March 2016	2015.1.00993.S	C36-1/2
	07 March 2016	2015.1.00993.S	C36-1/2
^{13}CO (1–0)	09 March 2016	2015.1.00993.S	C36-1/2
	11 March 2016	2015.1.00993.S	C36-1/2

Table 3.2 The achieved angular resolution and sensitivity for ALMA data

line	weight	beam size	rms (cube)	rms (integrated intensity)	rms (continuum)
		$''$	mJy beam^{-1}	mJy beam^{-1} km s^{-1}	mJy
H40α	robust = 2.0	1.48 $\times$ 1.31	0.08	11	–
H42α	robust = 2.0	2.57 $\times$ 2.05	0.18	27	–
^{13}CO (1–0)	robust = 0.5	1.43 $\times$ 1.33	0.24	50	–
99GHz	robust = 2.0	1.32 $\times$ 1.20	–	–	0.028

Table 3.3 H40α source identification

component	Longitude	Latitude	Peak	major	minor	PA	size
	degree	degree	Jy km s^{-1} beam^{-1}	arcsec	arcsec	$^\circ$	kpc^2
Northern nucleus	10:27:51.248	-43:54:14.318	93	2.2$\pm$0.17	1.9$\pm$0.13	169	0.38$\pm$0.01
Southern nucleus	10:27:51.221	-43:54:19.220	85	1.79$\pm$0.15	1.55$\pm$0.11	50	0.25$\pm$0.01
Arm	10:27:51.826	-43:54:12.445	44	1.63$\pm$0.26	1.27$\pm$0.16	41	0.19$\pm$0.01

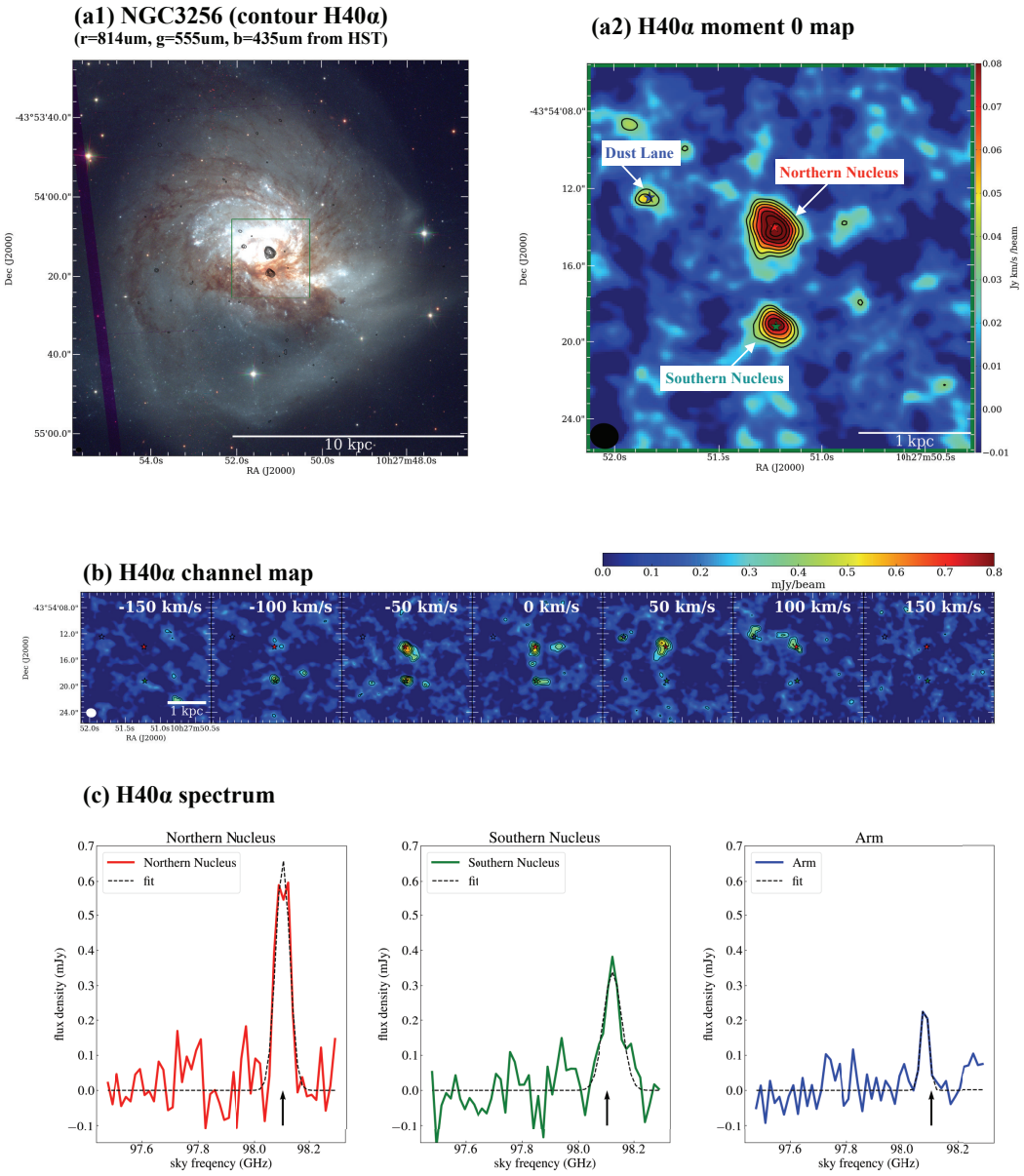

Figure 3.5 (a1) The optical color image of entire NGC 3256. Black contour shows H40α with $11 \times (3,4,5,6,7,8,9)$ [mJy beam^{-1} km s^{-1}]. (a2) The integrated intensity map of H40α image that achieves the angular resolution of $\sim 1\farcs48 \times \sim 1\farcs31$. H40$\alpha$ lines are detected at the northern nucleus, the southern nucleus, and the arm that is offset from two nuclei with the signal to noise ratio of 10, 8, and 4, respectively. Contours are same as (a1). (b) H40α channel map. The contour is $0.08 \times (3,4,5,6,7)$ [mJy beam^{-1}]. (c) H40α Spectrum with the photometric beam size of $\sim 1\farcs5$ at northern nuclei (red), southern nuclei (green), and arm (blue). The black dashed line is the result of gaussian fitting.

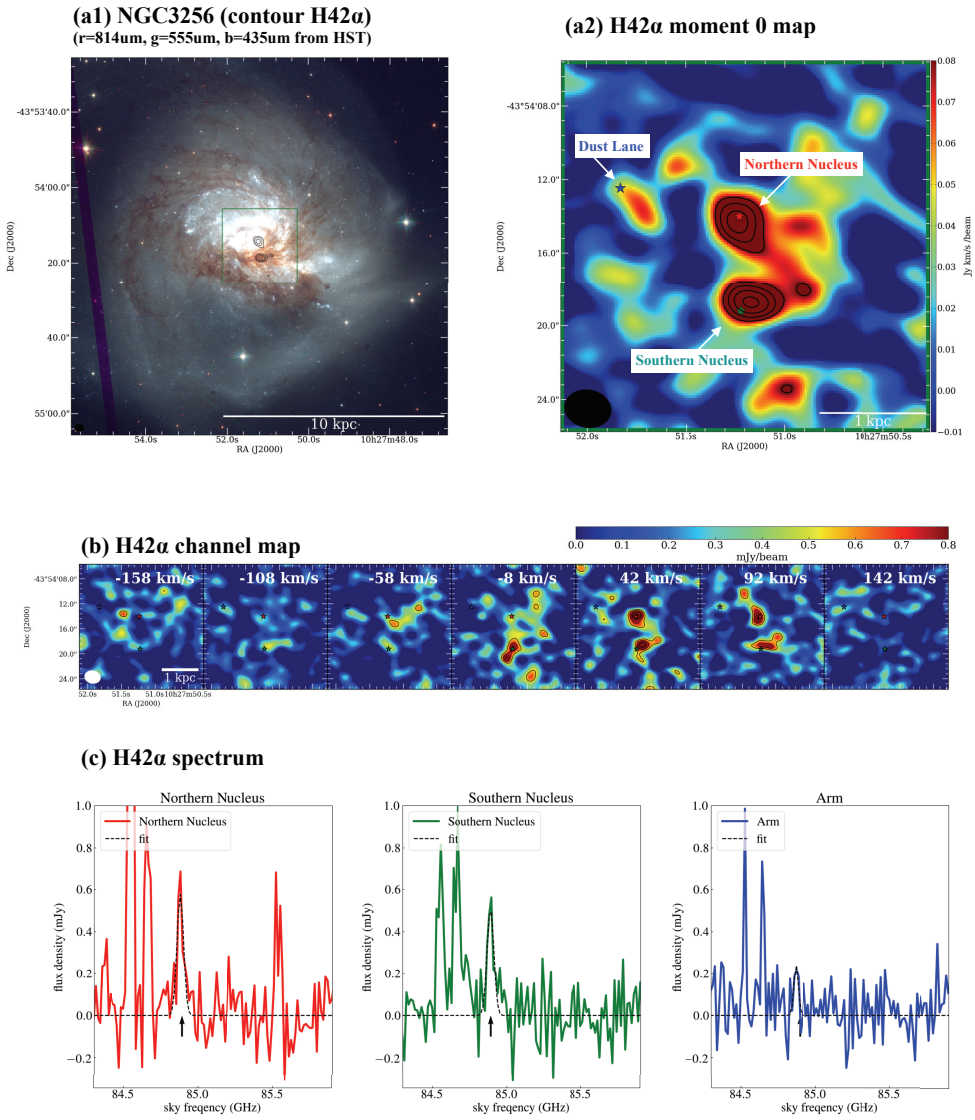

Figure 3.6 (a1) The optical color image of entire NGC 3256. Black contour shows H42α with $22 \times (3,4,5,6)$ [mJy beam^{-1} km s^{-1}]. (a2) The integrated intensity map of H40α image that achieves the angular resolution of $\sim 2\farcs57 \times \sim 2\farcs05$. I detect H42$\alpha$ at the northern nucleus and the southern nucleus with the signal to noise ratio of 5 and 5 respectively. Contours are same as (a1). (b) H42α channel map. The contour is $0.18 \times (3,4,5,6,7)$ [mJy beam^{-1}]. (c) H42α Spectrum with the photometric beam size of $\sim 2\farcs6$ at northern nuclei (red), southern nuclei (green), and arm (blue). The black dashed line is the result of gaussian fitting. There are other three emission lines in these spectrums; c-C_3H_2 ($2_{1,2}$–$1_{0,1}$) at 84.547 GHz, CH_3CCH (5_K–4_K) at 84.664 GHz, and SO (2_2–1_1) at 85.295 GHz (sky frequency).

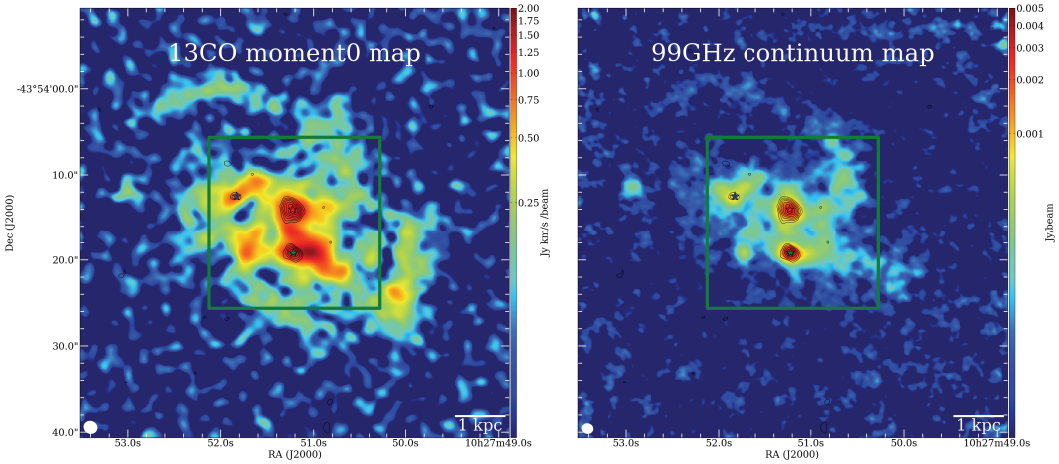

Figure 3.7 (left) The integrated intensity map of ^{13}CO (1–0) emission. (right) Continuum map at 99 GHz. The contours show the H40α emission.

3.5 Analysis

3.5.1 SFR diagnostic for hydrogen recombination lines

The relation between ionising photon rate Q [s^{-1}] and SFR [M$_\odot$ yr^{-1}] depends on initial mass function (IMF), mass range of stellar IMF, and time scale (τ) over which star formation needs to remain constant. Assuming Kroupa IMF (Kroupa , 2002), the mass range of $0.1-100$M$_\odot$, $\tau > 6$ Myr, and starburst model of `STARBURST99` (version 7.0.1), SFR can be calculated using the relation of

$$\frac{SFR}{\mathrm{M}_\odot\ \mathrm{yr}^{-1}} = 7.4\times10^{-54}\left[\frac{Q}{\mathrm{s}^{-1}}\right]. \tag{3.5}$$

The coefficient is from Calzetti (2013). Emission measure ($EM = n_e n_p V$, where n_e, n_p and V are ionized electron density, positive ion density, and volume of ionized HII region, respectively) is described by using total recombination line coefficient

($\alpha_{\rm B}$)

$$\frac{EM}{\rm cm^{-3}} = \left[\frac{Q}{\rm s^{-1}}\right]\left[\frac{\alpha_{\rm B}}{\rm cm^3\ s^{-1}}\right]^{-1}. \tag{3.6}$$

Using the specific emissivity (ϵ) of each recombination lines, the recombination line luminosity can be calculated by

$$\frac{L_{\rm RL}}{\rm erg\ s^{-1}} = \left[\frac{\epsilon}{\rm erg\ s^{-1}\ cm^{-3}}\right]\left[\frac{EM}{\rm cm^{-3}}\right]. \tag{3.7}$$

Here, the emissivity is given per unit $n_{\rm e}n_{\rm p}$. From equation (3.5)-(3.7),

$$\frac{SFR_{\rm RL}}{\rm M_\odot\ yr^{-1}} = (7.4\times10^{-54})\left[\frac{\epsilon}{\rm erg\ s^{-1}\ cm^{-3}}\right]^{-1}\left[\frac{\alpha_{\rm B}}{\rm cm^3\ s^{-1}}\right]\left[\frac{L_{\rm RL}}{\rm erg\ s^{-1}}\right]. \tag{3.8}$$

The luminosity can be converted from the observed total line flux (Solomon & Vanden Bout , 2005)

$$\frac{L_{\rm RL}}{\rm erg\ s^{-1}} = 4.0\times10^{30}\left[\frac{\int f_{\nu\rm RL}\,{\rm d}\nu}{\rm Jy\ kms^{-1}}\right]\left[\frac{\nu_{\rm rest}}{\rm GHz}(1+z)^{-1}\right]\left[\frac{D_{\rm L}}{\rm Mpc}\right]^2. \tag{3.9}$$

Finally, the relation between SFR and total recombination line flux (Bendo et al. , 2015) is

$$\frac{SFR_{\rm RL}}{\rm M_\odot\ yr^{-1}} = 2.96\times10^{-23}\left[\frac{\alpha_{\rm B}\ \rm cm^6}{\epsilon\ \rm erg}\right]\left[\frac{\nu}{\rm GHz}\right]\left[\frac{\rm D}{\rm Mpc}\right]^2\left[\frac{\int f_{\nu\rm RL}\,{\rm d}\nu}{\rm Jy\ km\ s^{-1}}\right]. \tag{3.10}$$

The $\alpha_{\rm B}$ terms depend on electron temperature ($T_{\rm e}$) and electron density ($n_{\rm e}$) assuming case-B recombination. The $\alpha_{\rm B}$ values are listed in Storey & Hummer (1995). I fixed the $n_{\rm e}$ of 10^3 cm^{-3} since the dependence is negligible in the range of 10^2-10^5 cm^{-3} (Storey & Hummer , 1995; Bendo et al. , 2015). I use log linear

interpolated relation between $\alpha_{\rm B}$ and $T_{\rm e}$ for hydrogen recombination

$$\frac{\alpha_{\rm B}}{\rm cm^3\ s^{-1}} = (3.6\times10^{-10})\left[\frac{T_{\rm e}}{\rm K}\right]^{-0.8}. \tag{3.11}$$

The ϵ values are also listed by Storey & Hummer (1995), and I fixed the $n_{\rm e}$ of 10^3 cm^{-3} to use the log-linearly interpolated relation between ϵ and $T_{\rm e}$. For example, in the case of optical, infrared and sub-mm recombination lines,

$$\left[\frac{\epsilon}{\rm erg\ s^{-1}\ cm^{-3}/n_e n_p}\right] \sim \begin{cases} (3.0\times10^{-27})\ \left[\frac{T_{\rm e}}{\rm K}\right]^{-1.3} & (\text{for H40}\alpha) \\ (1.2\times10^{-21})\ \left[\frac{T_{\rm e}}{\rm K}\right]^{-0.9} & (\text{for H}\alpha) \\ (1.9\times10^{-22})\ \left[\frac{T_{\rm e}}{\rm K}\right]^{-0.8} & (\text{for H}\beta) \\ (3.4\times10^{-23})\ \left[\frac{T_{\rm e}}{\rm K}\right]^{-1.0} & (\text{for Br}\gamma). \end{cases} \tag{3.12}$$

The free-free (Bremsstrahlung) continuum emission can also be used to probe the ionized gas *EM*. Therefore, it is possible to calculate SFR from the 99GHz flux density (Scoville & Murchikova , 2013; Bendo et al. , 2015)

$$\frac{SFR_{\rm cont}}{\rm M_\odot\ yr^{-1}} = 1.09\times10^{10}\ \left[\frac{\alpha_{\rm B}}{\rm cm^3\ s^{-1}}\right]\left[\frac{\nu}{\rm GHz}\right]^{0.17}\left[\frac{T_{\rm e}}{\rm K}\right]^{0.5}\left[\frac{\rm D}{\rm Mpc}\right]^2\left[\frac{f_{\nu\rm cont}}{\rm Jy}\right]. \tag{3.13}$$

From equation 3.10 and 3.13, the ratio of the line flux density integrated over velocity v to the free-free flux density can be written as

$$R = \frac{\int f_{\nu\rm line}\,{\rm d}\nu}{f_{\nu\rm cont}}\left[\frac{\rm Jy}{\rm Jy\ km\ s^{-1}}\right] = 3.68\times10^{32}\left[\frac{\epsilon}{\rm erg\ s^{-1}\ cm^{-3}}\right]\times\left[\frac{\nu}{\rm GHz}\right]^{-0.83}\left[\frac{T_{\rm e}}{\rm K}\right]^{0.5}. \tag{3.14}$$

The 99GHz continuum emission is dominated by free-free emission in most case. However, there is a possible contribution from non-thermal radio emissions

and dust emissions. In order to check this contribution, I use the 5.0, 8.3 and 15 GHz continuum flux density measured by Very Large Array (VLA) from literature (Neff et al. , 2003) and 200GHz Band6 data from archival ALMA data (Harada et al. , 2018). Figure 3.8 shows the spectral energy density (SED) of the northern and southern nucleus. Three power law components can explain ∼1-300 GHz SED. One is the power law from non-thermal emission and I use the slope as a free parameter. The other is free-free and dust emission with the slope of -0.17 and 4.0. I find that the contribution of free-free emission at 99GHz continuum flux density (frac-FF) is $\sim$ 75% and $\sim$ 85% at the northern and southern nucleus, respectively. I assume frac-FF of 80% to derive the parameters on the arm. Using equation 3.14 and 3.12, the $T_{\rm e}$ can be calculated. Subsequently, α_B, ϵ and SFR can be derived.

3.5.2 Molecular gas mass

Assuming optically thin emission and local thermodynamic equilibrium (LTE) condition, molecular gas mass associated with H40α detected regions is derived from ^{13}CO. It is assumed that excitation temperature of 10 K (Harada et al. , 2018) and the ^{12}CO/^{13}CO ratios ($R_{12/13}$) of $\sim$ 100 are constant in every region. These assumptions may have systematic errors. Henkel et al. (2014) show that the ^{12}C/^{13}C abundance ratios vary over the galaxy population; $>$ 100 in high-z U/LIRGs, $\sim$ 100 in local starburst galaxies, $\sim$ 40 in weaker starburst without large scale mergers, and $\sim$ 25 in the center of Milky Way. The following equation is used to convert from the ^{13}CO luminosity to molecular gas mass under these assumptions (Battisti & Heyer , 2014)

$$\frac{M_{\rm H_2}}{M_\odot} = 0.41\ R_{12/13}\ \frac{L'_{^{13}\rm CO}}{\rm K\ km\ s^{-1}\ pc^2} \tag{3.15}$$

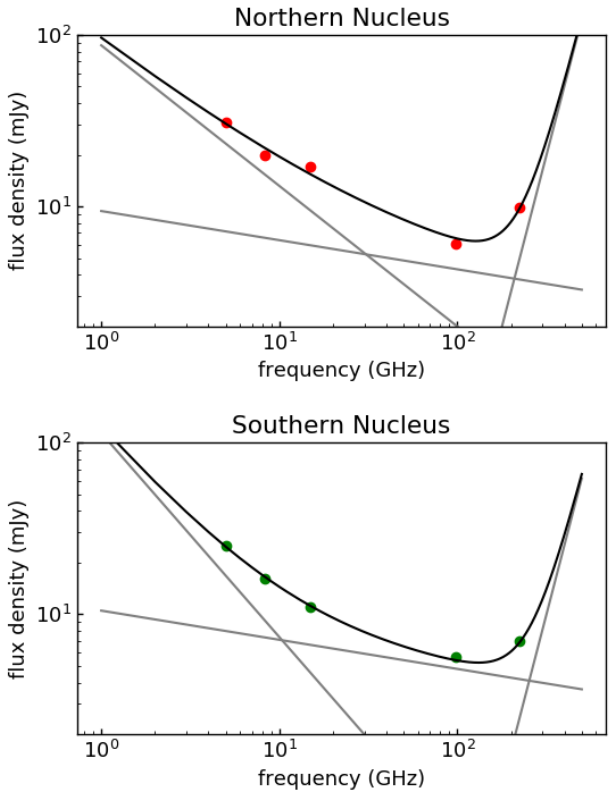

Figure 3.8 The spectral energy distribution (SED) at the northern and southern nucleus within 2.″5 and 3.″5. I use the 5.0, 8.3 and 15 GHz continuum flux density measured by Very Large Array (VLA) from literature Neff et al. (2003), and 224 GHz data points from archival ALMA data Harada et al. (2018). The gray lines show the three power law components. I use a synchrotron function with a power-law index that was allowed to vary, a free-free function with the index of -0.17, and a modified Rayleigh Jeans function for dust with the index of 4.

3.5.3 Result

The dust extinction corrected Hβ map (Figure 3.4c) shows spatially extended star forming regions. The total SFR based on Hβ map is $\sim 36\ M_{\odot}\ \mathrm{yr}^{-1}$. Table 3.4 shows the SFR and T_{e} of blobs where H40α detected. A conservative overall photometric error of 5 % is adapted, which is the technical requirement of ALMA cycle 3 and 4.. The SFR of three detected regions are 6.4 ± 0.4, 5.0 ± 0.4, and $1.3 \pm 0.1\ M_{\odot}\ \mathrm{yr}^{-1}$, respectively. A notable region is the southern nucleus. The SFR of southern nucleus is consistent with that of northern one within the error, nevertheless, strong Hβ emission at the southern nucleus is absent. This means that MUSE Hβ observation missed the HII region associated with the extremely dusty southern nucleus.

Figure 3.9 shows the traditional empirical star formation ($\Sigma_{\mathrm{H_2}} - \Sigma_{\mathrm{SFR}}$) based on pixel-by-pixel analysis using Hβ and ^{13}CO map. Three blobs detected by H40α (red, green, and blue markers in Figure 3.9) have surface density of SFR and $M_{\mathrm{H_2}}$ as high as that of starburst galaxies. It is obvious that optical observations missed the dusty star burst region at southern nucleus (green diamonds for extinction corrected Hβ map and a green cross for H40α observation). In addition to the intense three regions, all the other pixels show the higher surface density of SFR and $M_{\mathrm{H_2}}$ than the similar scale blobs obtained in nearby normal galaxies (i.e., Bigiel et al. , 2008). These blobs can be direct evidences of the offset starbursts in merging galaxies.

Table 3.4 SFR derived by recombination lines

component	$\int f_{\nu \mathrm{H40}\alpha}\,\mathrm{d}\nu$ mJy km s^{-1}	$f_{\nu \mathrm{cont}}$ mJy	R km s^{-1}	T_e K	$SFR_{(\mathrm{H40}\alpha)}$ M$_\odot$ yr^{-1}	$\Sigma_{SFR(\mathrm{H40}\alpha)}$ M$_\odot$ yr^{-1} kpc^{-2}	$\int f_{\nu \mathrm{H}\beta}\,\mathrm{d}\nu$ 10^{-13} erg s^{-1} cm^{-2}	$SFR_{(\mathrm{H}\beta)}$ M$_\odot$ yr^{-1}
Northern Nucleus	118±6	2.74±2.74	43±3	4100±400	6.4±0.4	34.0±2.3	10.6	4.4
Southern Nucleus	61±3	2.74±2.74	22±2	9400±800	5.0±0.3	40.1±2.7	0.7	0.3
Arm	24±1	0.53±0.53	45±3	3900±300	1.3±0.1	12.8±0.9	2.1	0.9

Table 3.5 Molecular gas mass derived by ^{13}CO (1–0)

component	$\int f_{\nu 13\mathrm{CO}}\,\mathrm{d}\nu$ Jy km s^{-1}	M_{H_2} 10^8 M$_\odot$	$\Sigma_{M_{\mathrm{H2}}}$ M$_\odot$ pc^{-2}
Northern Nucleus	1.54±0.08	5.1±0.3	2670±130
Southern Nucleus	1.09±0.05	3.6±0.2	2860±140
Arm	0.52±0.03	1.7±0.1	1710±90

3.6 Discussion

I calculate the total SFR based on extinction corrected Hβ map of $\sim 36\ M_{\odot}\ \mathrm{yr}^{-1}$ in Section 3.5.3. However, this value underestimates the total SFR due to the significant dust extinction. Based on the H40a data, I calculate SFR of the dusty starburst region at the southern nucleus to be $\sim 5.0\ M_{\odot}\ \mathrm{yr}^{-1}$. Therefore, I use the sum of both non-dusty and dusty star formation ($\sim 41\ M_{\odot}\ \mathrm{yr}^{-1}$) as a total SFR in NGC 3256. The key questions are (i) whether optical and infrared nebular emission (e.g., Hα, Hβ, and Brγ) can trace the true SFR or not. (ii) how much nuclear starbursts contribute toward the total SFR from entire the galaxy. (iii) whether star formation rate (SFR) derived from nebulae recombination lines is consistent with the SFR from FIR luminosity.

3.6.1 Northern Nucleus

The primary heating source is likely related to starburst activity at the northern galaxy (Ohyama et al. , 2015). At the northern nucleus, there is the largest (size = 0.38 ± 0.01 kpc^2) H40α nebula among identified three (Table 3.3). The derived T_{e} of 4100$\pm$400 K is consistent with the HII regions in NGC 253 and NGC 4945 (3700–6300 K) (Bendo et al. , 2015, 2016) that do not have merging or interacting evidences. The derived SFR is 6.4$\pm$0.4 $M_{\odot}\ \mathrm{yr}^{-1}$, which is $\sim$ 16% of the total SFR. The star formation rate surface density (Σ_{SFR}) is 34.0$\pm$2.3 $M_{\odot}\ \mathrm{yr}^{-1}\ \mathrm{kpc}^{-2}$ and molecular gas mass surface density ($\Sigma_{M_{\mathrm{H_2}}}$) is $2670 \pm 70\ M_{\odot}\ \mathrm{pc}^{-2}$, which is a typical value for the starburst galaxies (Kennicutt , 1998). I conclude that HII regions at northern nucleus in NGC 3256 consistent with similar regions in typical starburst galaxies. At the northern nucleus, the SFR derived from Hβ is $\sim 4.4\ M_{\odot}\ \mathrm{yr}^{-1}$, this is $\sim$ 70% of SFR derived from H40α (Table 3.4). The difference is probably due to imperfect dust extinction correction using Hα and Hβ ratio.

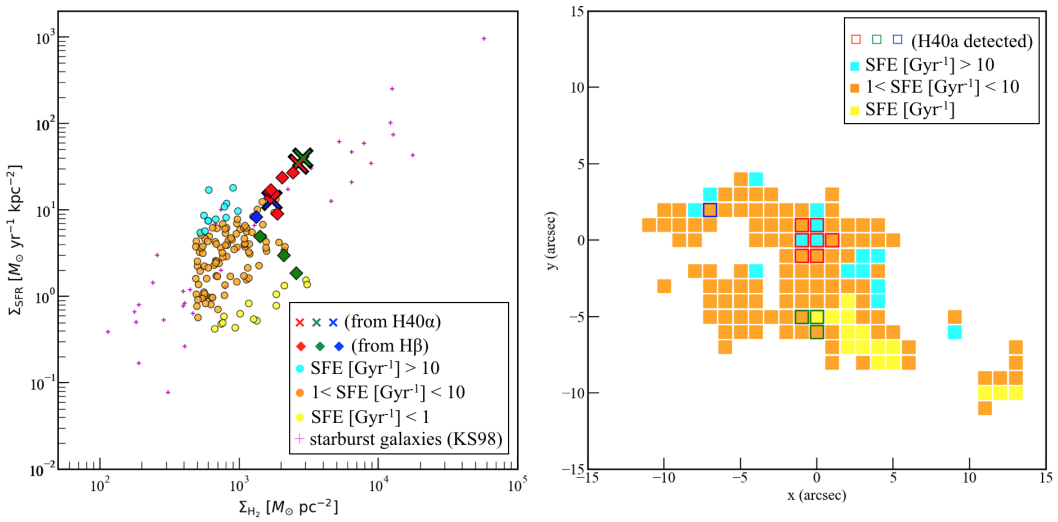

Figure 3.9 (left) Pixel by pixel analysis for a empirical star formation relation ($\Sigma_{H_2} - \Sigma_{SFR}$). A pixel is corresponding to 1" $\sim$ 170 pc. The red, green, and blue crosses correspond to the northern nucleus, southern nucleus, and arm in Tables 3.4 and 3.5. The red, green, and blue diamonds correspond to the pixel by pixel analysis based on Hβ map for the northern nucleus, southern nucleus, and arm. The cyan, orange, and yellow circles correspond to the pixel with SFE [Gyr^{-1}]>10, 1 $<$ SFE [Gyr^{-1}] $<$ 10, SFE [Gyr^{-1}]<1, respectively. The magenta plus singns are the star burst galaxies in Kennicutt (1998). (right) The red, green, and blue squares correspond to the positions for the pixel with SFE [Gyr^{-1}]>10, 1 $<$ SFE [Gyr^{-1}] $<$ 10, SFE [Gyr^{-1}]<1, respectively. The red, green, and blue squares correspond to red, green, and blue circles in left panel.

3.6.2 *Southern Nucleus*

The H40α emissions are detected at the southern nucleus where there is no strong emission in extinction corrected Hβ map (Figure 3.4c). The SFR derived from optical observation is about ten times lower than SFR derived from H40α ($SFR = 5.0 \pm 0.3\ M_{\odot}\ \mathrm{yr}^{-1}$). This suggests that the optical emission around southern nucleus is not originally from extremely dust obscured nebulae emission. The SFR of 0.8 $M_{\odot}\ \mathrm{yr}^{-1}$ from Hβ may be contribution from the different components (e.g., surface of the dusty star forming region). In terms of the empirical star formation relation (e.g., Kennicutt , 1998; Daddi et al. , 2010), the star formation activity at the dusty southern nucleus is consistent with northern less dusty nucleus within error bars.

The southern nucleus can be detectable at wavelength $\gtrsim 1\mu$m (Lípari et al. , 2000). Piqueras López et al. (2012, 2013) have conducted SINFONI integral field spectroscopy (IFS) observation with Very Large Telescope (VLT) towards U/LIRGs, and detect Brγ emission from the southern nucleus of NGC 3256 (norther nucleus is not in the field of view) (Figure 3.10). I obtain the Brγ image from on-line catalog (Piqueras López et al. , 2016) and measure the Brγ flux of $\sim 6.3 \times 10^{-15}$ erg s^{-1} cm^{-2} at the southern nucleus. Assuming $A_{\mathrm{Brg}} \sim 1.2$ estimated from Brγ/ Brδ ratio (Piqueras López et al. , 2013), I find that SFR estimated from Brγ ($SFR_{(\mathrm{Br}\gamma)}$) is $\sim 3.3\ M_{\odot}\ \mathrm{yr}^{-1}$, which is $\sim 60\%$ of the SFR derived from H40α. This suggests that dust extinction magnitude is underestimated. In order to achieve the SFR of $\sim 5.0\ M_{\odot}\ \mathrm{yr}^{-1}$, $A_{\mathrm{Br}\gamma}$ is about 1.7, which is corresponding to $A_{\mathrm{V}} \sim 17$ ($A_{\mathrm{Br}\gamma} = 0.096 A_{\mathrm{V}}$).

One concern is that the southern nucleus shows the evidence of low-luminosity AGN based on the IRAC color and silicate absorption feature (Ohyama et al. ,

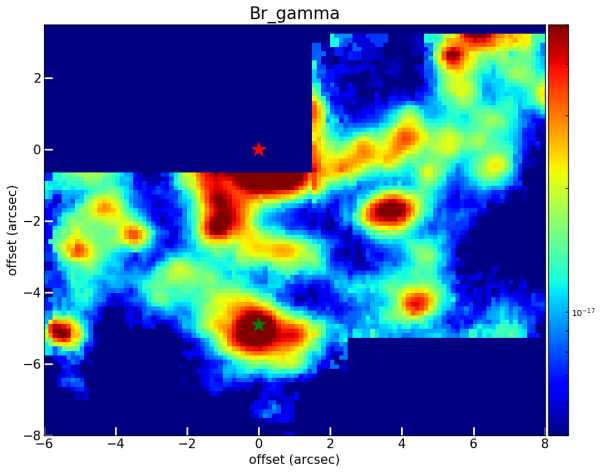

Figure 3.10 The spatial distribution of the Brγ emission obtained by SINFONI/VLT.

2015). The recombination lines are expected to be identified in the broad-line region of obscured AGN. However, Izumi et al. (2016) show that the expected line flux is too low to be detected even by ALMA.

3.6.3 Extended starburst

The sum of the nuclear starburst in the northern and southern nucleus is $11.4 \pm 0.6\ M_{\odot}\ \mathrm{yr}^{-1}$, which means that the contribution of nuclear and spatially extended starburst is $\sim 27\%$ and $\sim 73\%$, respectively. Such a disk-wide starburst is expected based one IR SED fitting (Lira et al. , 2008). They calculated SFR is ~ 15 and $\sim 6\ \mathrm{M}_{\odot}\ \mathrm{yr}^{-1}$ at the northern and the southern nuclei, respectively. This means that the ratio between mid-IR continuum and hydrogen recombination lines is higher in the northern nucleus than the southern nucleus. The reason is not clear but one possible explanation is that the excess mid-IR flux is possibly because continuum

warm dust heated by the starburst itself. The important finding is that both hydrogen recombination lines and IR-SED fitting show the large contribution of disk-wide starburst agains nuclear starburst in NGC 3256. In addition, one H40α blob is detected on the arm at the dust lane that is offset from the two nuclei (Arm in Figure 3.5(a2)). This blob is also identified in dust extinction corrected Hβ map (Figure 3.4c). The SFR in this blob is1.3$\pm$0.1 $M_\odot$ yr^{-1} corresponding to Σ_{SFR} is 12.8$\pm$0.9 $M_\odot$ yr^{-1} kpc^{-2} based on H40α observation. This is $\sim$ 3% of the total SFR. The SFE is 12.5 ± 1.1 Gyr^{-1}, 13.9 ± 1.1 Gyr^{-1}, and 7.6 ± 0.7 Gyr^{-1} at Northern Nucleus, Southern Nucleus, and Arm, respectively (Figure 3.9). These are as high as SFE of local starburst galaxies investigated by (Kennicutt , 1998). Figure 3.9 shows that star forming blobs in NGC 3256 have large scatter in Σ_{H_2}–Σ_{SFR}. There are blobs with SFE of $>$ 10 Gyr^{-1} as well as blobs with SFE of $<$ 1 Gyr^{-1} outside of nuclear region. This means that the SFE is not uniform in NGC 3256. It is necessary to investigate the mechanism to explain both efficient and in-efficient star formation activity simultaneously, in the future.

3.6.4 FIR luminosity

My analysis shows that the total SFR is ~ 41 $M_\odot$ yr^{-1} in NGC 3256 including both Hβ and H40α. The conversion from recombination line luminosity to SFR (equation 3.8) is applicable when star formation have remained over timescale $\tau > 6$ Myr. It does not depend on long timescale, which means that recombination lines can trace current young (10-100 Myr) starburst activity (Calzetti , 2013). On the other hand, conversion from total IR luminosity ($L_{\rm TIR}$) to SFR depends on longer timescale due to the accumulation over time of long-lived low-mass stars in

the stellar SED. For example,

$$\frac{SFR_{\rm TIR}}{\rm M_\odot\ yr^{-1}} = \begin{cases} (1.6\times10^{-44})\ \frac{L_{\rm TIR}}{\rm erg\ s^{-1}} & (\tau = 10\ {\rm Gyr}) \\ (2.8\times10^{-44})\ \frac{L_{\rm TIR}}{\rm erg\ s^{-1}} & (\tau = 100\ {\rm Myr}) \\ (3.7\times10^{-44})\ \frac{L_{\rm TIR}}{\rm erg\ s^{-1}} & (\tau = 10\ {\rm Myr}) \end{cases} \tag{3.16}$$

assuming Kroupa IMF and the mass range of $0.1-100$ M$_\odot$ (Calzetti , 2013). Using the $L_{\rm TIR} = 10^{11.56}$ L$\odot$ (Sanders et al. , 2003), $SFR_{\rm TIR}$ ∼22, 39, and 51 M$_\odot$ yr^{-1} for τ =10 Gyr, 100 Myr, and 10 Myr, respectively. This means that recombination lines and FIR observation suggest that star formation has remain ∼ 100 Myr in NGC 3256. This time scale is shorter than the merger age of ∼ 500 Myr (Lípari et al. , 2000). It can possibly be a evidence to show that starburst activity in NGC 3256 is triggered by galaxy-galaxy merger. However, it is necessary to consider the systematical error for the estimation of SFR and AGN contributions against FIR luminosity in order to investigate the time scale of starburst activity.

3.6.5 Variety of the electron temperature

The electron temperature is derived when the SFR is calculated. I find that electron temperature around the southern nucleus is a factor of two higher ($T_{\rm e}$=9400±800K) than northern nucleus and HII regions in the other galaxies (e.g., NGC 253 and NGC 4945) (Bendo et al. , 2015, 2016). This difference is originally from the line ratio $R = \int f_{\nu\rm line}{\rm d}\nu / f_{\nu\rm cont}$. The actual flux density from free-free emission (after correction) ∼ 2.7 [mJy] for both northern and southern nucleus. On the other hand, the H40α line flux is 118 ± 6 and 61 ± 3 [mJy km s^{-1}]. This means that free-free emission has a same flux density for the northern and southern nucleus, while the recombination line flux at the southern nuclei is about half of the northern one. In order to explain this difference, higher electron density is necessary in the southern

nucleus than the northern one.

In the case of star forming regions in Milky Way, there is a clear relation between electron temperature and metallicity (Shaver et al. , 1983), and the relation is modeled by Pagel (1979). Using the relation for the HII regions in Milky Way, the $T_e \sim 9400$ K for the southern nucleus corresponds to $12+\log(O/H) \sim 8.4$ and $T_e \sim 4200$ K for the nouthern nucleus corresponds to $12+\log(O/H) \sim 9.2$ ($Z \sim 3.5 Z_\odot$), where $12+\log(O/H)_\odot = 8.66$ and $Z_\odot = 0.014$ (Asplund et al. , 2009). Kewley et al. (2006) show that the central metallicity in the interacting galaxies tends to be lower than non-interacting systems of equivalent mass, and later Rupke et al. (2008); Herrera-Camus et al. (2018) find the same trend for U/LIRGs. Low metallicity in merging galaxies is explained by nuclear inflows of metal poor-interstellar gas during merger process. Chemical enrichment from star formation, gas consumption, and AGN and SN feedback (e.g., outflows) can also influence the nuclear metallicity (Torrey et al. , 2012). The exact origin is under discussion. The important suggestion from our H40α observations of NGC 3256 is that metallicity of extremely dusty nucleus ($A_V \sim 18$) in merging galaxy is lower than the non-dusty regions where UV or optical emission line can be detected. This suggests that the merger induced starburst due to a large scale inflow mainly occurs in the dusty southern nucleus, and star formation history is different from non-dusty regions. The other possibility is massive outflow (Sakamoto et al. , 2014) that remove gas and metal. The properties of the molecular gas outflows are investigated in Chapter 4. Finally, I note that the conversion from ionising photon rate Q and SFR (equation 3.5) depends on metallicity. For example, the conversion factor could be 1.5 times small in the case of the low metallicity galaxy NGC 5253 (Bendo et al. , 2017) with the metallicity of $12+\log(O/H) \sim 8.26$ ($Z \sim 0.0056$), and the SFR may be overestimated at the southern nucleus.

3.7 Chapter Summary

In order to show the evidences for the large contribution of disk-wide starbursts against total SFR in a merging galaxy NGC 3256, I investigate spatially resolved SFR by using optical and mm hydrogen recombination line. At first, I use optical integral field units (MUSE mounted on VLT) and obtain maps of recombination lines (i.e., Hα and Hβ). I found many star forming blobs outside of nuclear regions. However, it is difficult to investigate star formation activities in dusty regions by using optical observations. I use mm recombination lines to investigate "true" star formation activity without dust extinction. I observed H40α and H42α by using ALMA. The total SFR obtained by Hβ and H40α line emission is $\sim 41\ M_{\odot}\ \mathrm{yr}^{-1}$. The main findings are as follow;

(1) I detect H40α emission at the northern and southern nucleus and arm that offsets from nuclei. However, there are no bright Hβ blobs in the souther nucleus. This means that there is a heavily dust obscured blob at the southern nucleus that is not detected in optical lines due to the large A_{V}. The SFR from the southern dusty region is $5.0 \pm 0.3\ M_{\odot}\ \mathrm{yr}^{-1}$, which is the 12% of total SFR.

(2) The sum of the nuclear starburst in the northern and southern nucleus is $11.4 \pm 0.5\ M_{\odot}\ \mathrm{yr}^{-1}$, which means that the contribution of nuclear and spatially extended starburst is $\sim 27\%$ and $\sim 73\%$, respectively. This means that disk-wide starbursts are more important than dust-enshrouded nuclear starbursts.

(3) Recombination line and total FIR luminosity suggest the starburst timescale of $\sim 100\ \mathrm{Myr}^{-1}$. This is shorter than the timescale of merger process ($\sim 500\ \mathrm{Myr}^{-1}$). It likely suggests that the current starbursts are triggered by a

merger process.

(4) The electron temperature is higher in dusty blob at the southern nucleus (9400 ± 800K) than the other non-dusty blobs at the northern nucleus (4100 ± 400K) and at the arm (3900 ± 300K). This suggests the lower metallicity in the southern nucleus due to metal poor gas inflow or massive outflow of metal and gas.

3.8 Chapter Appendix

For ALMA data, I follow the calibration method conducted by East Asian ALMA Regional Center. However, I have conducted additional analysis for band-edge flagging and flux scaling for the specific data set[4]. At first, we flag 8 channels for band-edge, whereas original analysis flag 15 channels that include the channels near the H40α emission. For the same data set, there is a problem for the flux scaling. We re-scale the flux, comparing the continuum flux density between nearby spectral windows obtained by independent observations. The detail of the analysis in CASA is following scripts.

```
# [Original]
  flagdata(vis = 'uid___A002_Xb00ce7_X47b4.ms.split',
    mode = 'manual',
    spw = '0:0~14;225~239,
    1:0~14;225~239,
    2:0~14;225~239,
    3:0~14;225~239',
    flagbackup = F)
# [new]
flagdata(vis = 'uid___A002_Xb00ce7_X47b4.ms.split',
    mode = 'manual',
    spw = '0:0~7;232~239,
    1:0~7;232~239,
    2:0~7;232~239,
    3:0~7;232~239',
    flagbackup = F)
```

```
# [Original]
setjy(vis = 'uid___A002_Xb00ce7_X47b4.ms.split.cal',
```

[4] 'uid___A002_Xb00ce7_X47b4.ms.split'

```
  field = 'J1038-4325',
  spw = '0',
  standard = 'manual',
  fluxdensity = [0.20777, 0, 0, 0])
# [new]
setjy(vis = 'uid___A002_Xb00ce7_X47b4.ms.split.cal',
  field = 'J1038-4325',
  spw = '0',
  standard = 'manual',
  fluxdensity = [0.20777*1.115, 0, 0, 0])
```

4 | Dense molecular gas outflows in NGC 3256

4.1 Science Goal

As shown in section 1.3, one of the most important issues of the merger evolution scenario is to understand the feedback mechanism during the merger process. The galactic scale outflow works as a feedback mechanism, removing the material for the star formation (and/or black hole accretion) from the nuclear region and/or heating the interstellar gas (i.e., negative feedback) (e.g., Di Matteo et al. , 2005; McNamara & Nulsen , 2007). On the other hand, Maiolino et al. (2017) show the possible evidence for the star formation in the outflow based on optical spectroscopic observations (i.e., positive feedback). Theoretical models predict such positive feedback near AGN, forming dense gas clumps in the outflow by the interaction between jet and the impinging ISM (e.g., Zubovas & Nayakshin , 2014; Costa et al. , 2015; Ferrara & Scannapieco , 2016; Zubovas & Bourne , 2017). Such dense clouds are continuously formed in the outflows (Richings & Faucher-Giguère , 2018). Therefore, molecular outflows play an important role in terms of both positive and negative feedback.

In observations, CO lines are used to identify the outflows (e.g., Cicone et al. , 2014). However, CO does not trace the densest parts of molecular clouds where star formation occurs. High sensitivity ALMA observations allow us to investigate the outflows in molecular lines other than CO, which further allows us to reveal the physical and/or chemical properties of outflows. In this chapter, I use ALMA

to look for the dense gas outflows in HCN and HCO^+ emissions whose critical densities are roughly three orders of magnitude higher than CO for a given J.

I identify NGC 3256 as an ideal laboratory to investigate the feedback mechanisms since high velocity components in CO are already identified to be related to cold gas outflows from both the northern and southern nuclei (Sakamoto et al. , 2014). The summary of their findings are as follows.

[Northern outflow]

An uncollimated bipolar outflow is found in the northern nucleus, which has a maximum velocity of ~ 750 km s^{-1} and mass of $\sim 6 \times 10^7\ M_\odot$. Comparing the energy of the outflow and starburst activity in the northern nucleus, it is suggested that the northern outflow is driven by the starburst activity.

[Southern outflow]

A collimated bipolar CO outflow is found in the southern nucleus, which has a maximum velocity of ~ 2600 km s^{-1} and mass of $\sim\ 2.5 \times 10^7\ M_\odot$. The southern outflow is associated with the jet detected by Very Large Array (Neff et al. , 2003), which is possibly triggered by a weak or recently dimmed AGN in the southern nucleus. Emonts et al. (2014) identify the broad near infrared (near-IR) H_2 emission line associated with southern outflow, which suggests that shocks or X-ray heat the gas to ~ 2000 K. The shock enhancement in NGC 3256 is suggested by Rich et al. (2011) based on optical IFU observations and by Harada et al. (2018) based on ALMA line survey observation.

I investigate the physical and chemical components of the outflow in NGC 3256, and provide the observational evidence for the feedback mechanism during the merger process through the comparison between dense gas traced by HCN and HCO^+ and diffuse gas traced by CO. Furthermore, I quantify the physical properties of outflows by using Bayesian likelihood statistical analysis under the assumption

of non local thermodynamic equilibrium (non-LTE).

Here, the line ratios (in unit of brightness temperature) are defined by the symbol "R" as follows; $R_{21/10}$ = CO (2–1) / CO (1–0), $R_{32/10}$ = CO (3–2) / CO (1–0), $R_{\rm HCN/CO}$ = HCN (1–0) / CO (1–0), $R_{\rm HCO^+/CO}$ = HCO^+ (1–0) / CO (1–0), and $R_{\rm HCN/HCO^+}$ = HCN (1–0) / HCO^+ (1–0). Part of this chapter is published in the APJ, 868, 95, (2018) as ALMA Observations of HCN and HCO+ Outflows in the Merging Galaxy NGC 3256 by Tomonari Michiyama (Michiyama et al. , 2018).

4.2 ALMA data

HCN (1–0) and HCO^+ (1–0) observations were carried out on 2016 March 7 and 8 using 45 twelve meter antennas (ALMA Project ID: 2015.1.00993.S), and I used the calibrated visibility data. The continuum is subtracted by using the uvcontsub task in `CASA` (McMullin et al. , 2007). The image cubes are produced by using tclean task in `CASA` (version 4.7.0, Briggs weighting, robust = 0.5) with automatically masking loop as described in the `CASA Guides`[1]. The image has an angular resolution of $2\farcs1 \times 1\farcs7$ (360 $\times$ 460 pc) and the r.m.s noise level is ~ 0.2 mJy beam^{-1} for the velocity resolution of 30 km s^{-1}. Channel maps are shown in Figures 4.1 and 4.2. North-Nucleus and South-Nucleus (stars in Figures) are defined by the peaks of the radio emission (Neff et al. , 2003). Investigating the line ratios, beam-matched ($2\farcs1 \sim 360$ pc) and uv-clipped (> 18 kλ) images are used so that their largest angular scales are consistent with those of the archival CO data. The absolute flux is calibrated using Ganymede with the nominal calibration error of 5%. The long term flux variation of the bandpass calibrator is 6 %. Therefore, 10 % error is adopted as a conservative overall photometric error. For CO (2–1) observation, I use the archival data (ALMA Project ID: 2015.1.00714.S). Beam-

[1] https://casaguides.nrao.edu/index.php/M100_Band3_Combine_4.3

matched and uv-clipped images are produced by using clean task in CASA (version 4.7.0, Briggs weighting, robust = 0.5) with automatically masking loop. CO (1–0) and CO (3–2) observations were conducted during Cycle0 (ALMA Project ID: 2011.0.00525.S), and I used the calibrated archival data. I combined the visibility data from the compact (15–269 m) and the extended (16–374 m) configurations. The channel maps for CO lines are in Figure 4.3-4.5

Table 4.1 The coordinates of symbols in figures

region	RA. (J2000)	DEC. (J2000)	symbol
North-OF-Blue	$10^{h}27^{m}51\overset{s}{.}02$	$-43°54'13\overset{''}{.}12$	blue triangle
North-Nucleus	$10^{h}27^{m}51\overset{s}{.}23$	$-43°54'14\overset{''}{.}00$	star
OF-Red	$10^{h}27^{m}51\overset{s}{.}20$	$-43°54'15\overset{''}{.}64$	red circle
South-Nucleus	$10^{h}27^{m}51\overset{s}{.}22$	$-43°54'19\overset{''}{.}20$	star
South-OF-Blue	$10^{h}27^{m}51\overset{s}{.}17$	$-43°54'21\overset{''}{.}43$	blue circle

4.3 Identification and properties of molecular outflows

4.3.1 Outflow Identification

The kinematics of the gas associated with the outflow are distinct from the systematic disk rotation. Therefore, the emission associated with possible outflow can be identified by extracting the emission at the extreme (i.e., largest and smallest) velocities in the channel as a first order method. I define the emission in $v = [240, 360]$ km s^{-1} and $v = [-360, -180]$ km s^{-1} as the red-shifted and blue-shifted outflow gas, respectively. Figure 4.6 shows moment 0 maps generated using these velocity ranges. I define “South-OF-Blue" to indicate the location of the blue-shifted component at the south of South-Nucleus, and “OF-Red" to indicate the red-shifted component which is located between North- and South-Nucleus. Further-

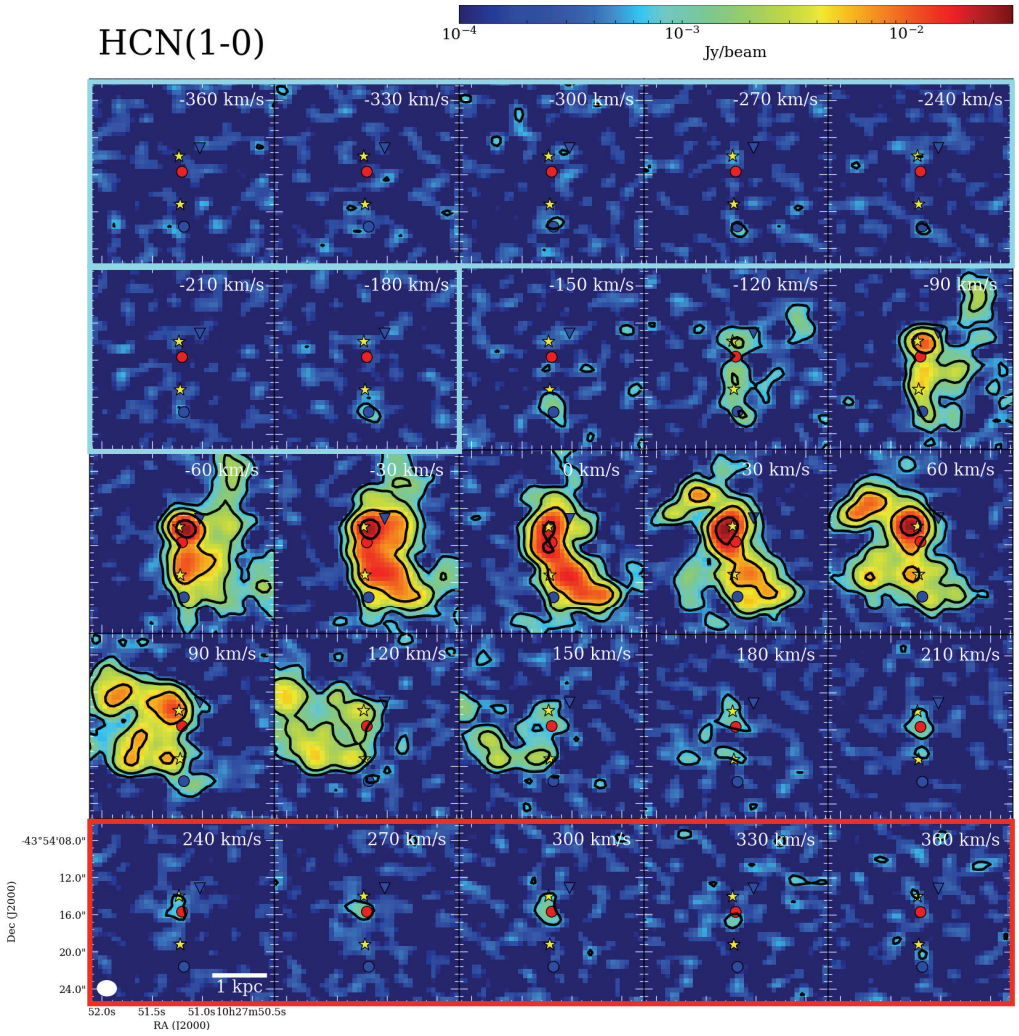

Figure 4.1 HCN (1–0) channel map. The size of each map is 20 ″(3.4 kpc) square centered on RA. = $10^{\rm h}27^{\rm m}51\overset{\rm s}{.}18$, Dec. = $43^\circ54'17\overset{''}{.}85$. The black contours are at nσ ($n = 3, 9, 27, 81$ and $\sigma = 0.2$ mJy beam^{-1}). The stars, circles, and a triangle are corresponding to the coordinates shown in Table 4.1. The stars represent the positions of the northern and southern nuclei. The blue circle and triangle are the positions of the blue-shifted components, and the red circle is the positions of red-shifted components identified in section 4.3.1. We obtain the blue and red wing maps by integrating the emission in the velocity range [-360,-180] km s^{-1} and [240,360] km s^{-1}.

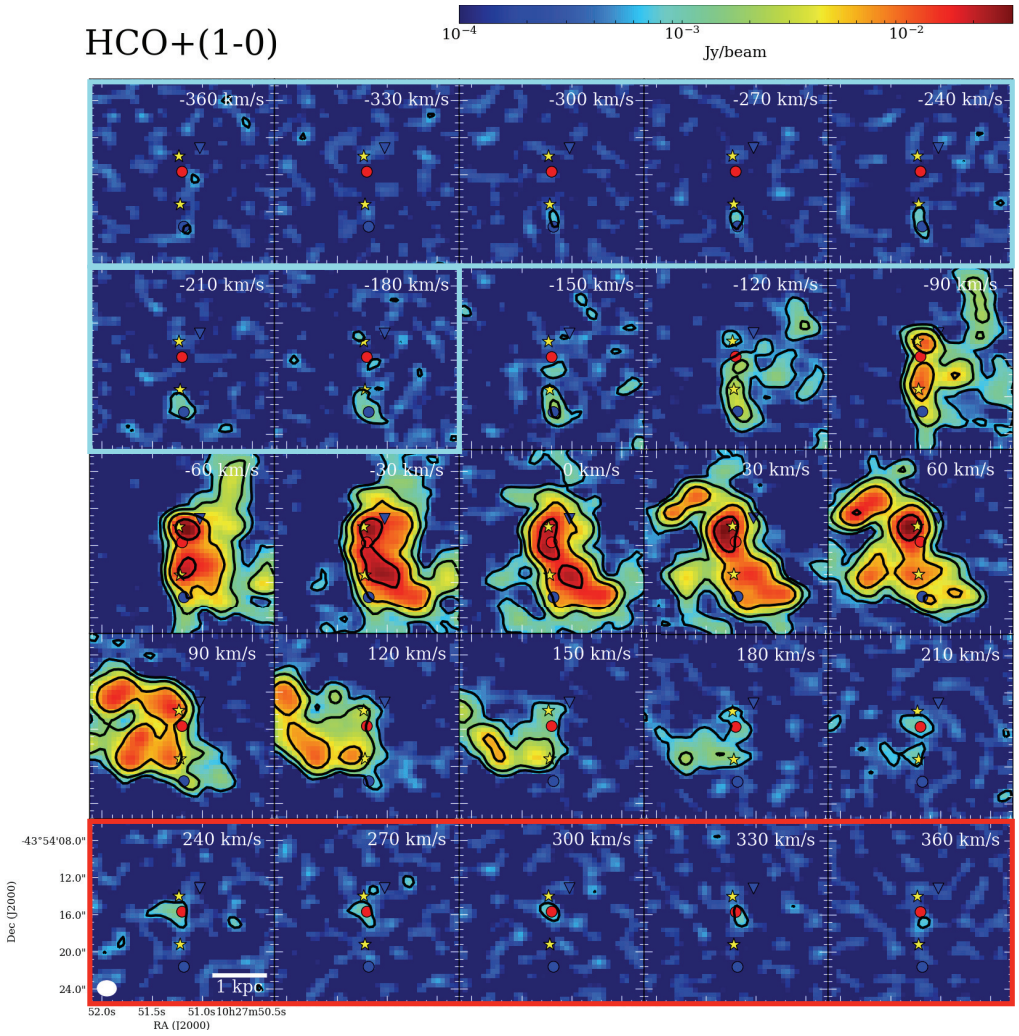

Figure 4.2 HCO^+ (1–0) channel map. The size of each map is 20 ″(3.4 kpc) square centered on RA. = $10^h27^m51^s.18$, Dec. = 43°54′17.″85. The black contours are at n$\sigma(n = 3, 9, 27, 81$ and $\sigma = 0.2$ mJy beam^{-1}). The stars, circles, and a triangle are corresponding to the coordinates shown in Table 4.1. The stars represent the positions of the northern and southern nuclei. The blue circle and triangle are the positions of the blue-shifted components, and the red circle is the positions of red-shifted components identified in section 4.3.1. We obtain the blue and red wing maps by integrating the emission in the velocity range [-360,-180] km s^{-1} and [240,360] km s^{-1}.

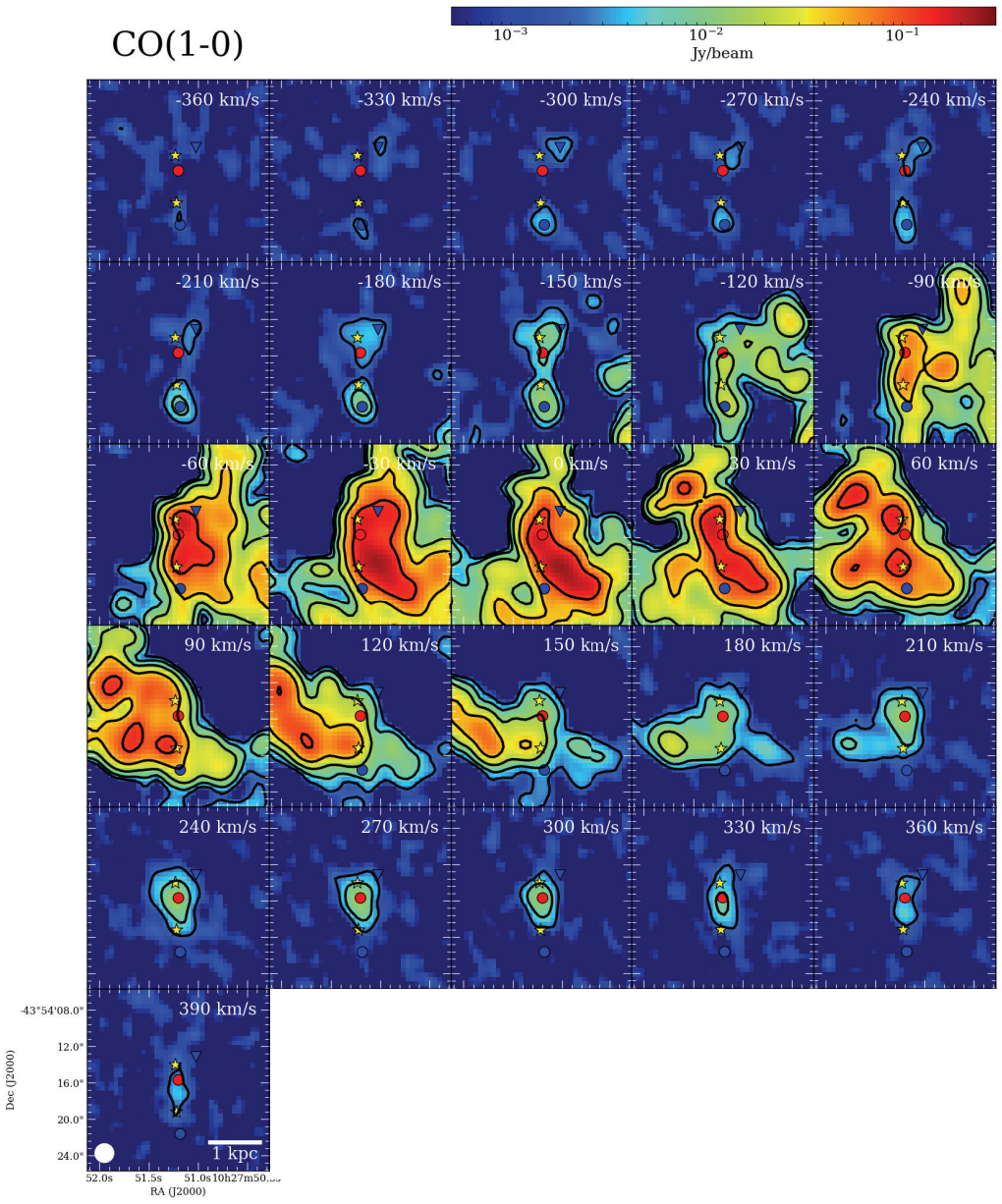

Figure 4.3 CO (1–0) channel map. The size of each map is 20 ″(3.4 kpc) square centered on RA. = $10^{\rm h}27^{\rm m}51\overset{\rm s}{.}18$, Dec. = $43^\circ54'17\overset{''}{.}85$. The black contours are at nσ($n = 3, 9, 27, 81$ and $\sigma = 3$ mJy beam^{-1}). The stars, circles, and a triangle are corresponding to the coordinates shown in Table 4.1.

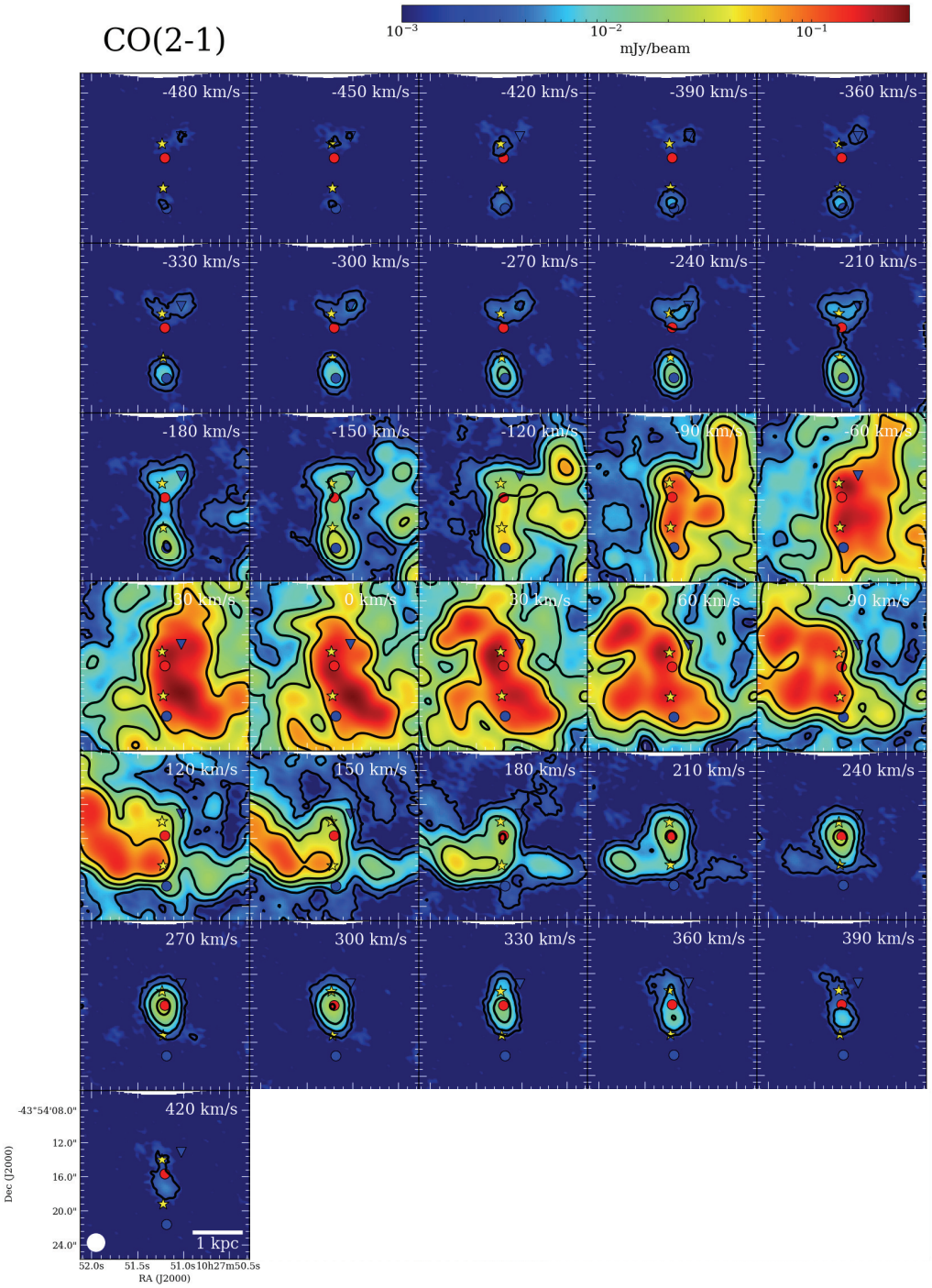

Figure 4.4 CO (2–1) channel map. The size of each map is 20 ″(3.4 kpc) square centered on RA. = $10^{\rm h}27^{\rm m}51\overset{\rm s}{.}18$, Dec. = $43^\circ54'17\overset{''}{.}85$. The black contours are at n$\sigma(n = 3, 9, 27, 81$ and $\sigma = 2$ mJy beam^{-1}). The stars, circles, and a triangle are corresponding to the coordinates shown in Table 4.1.

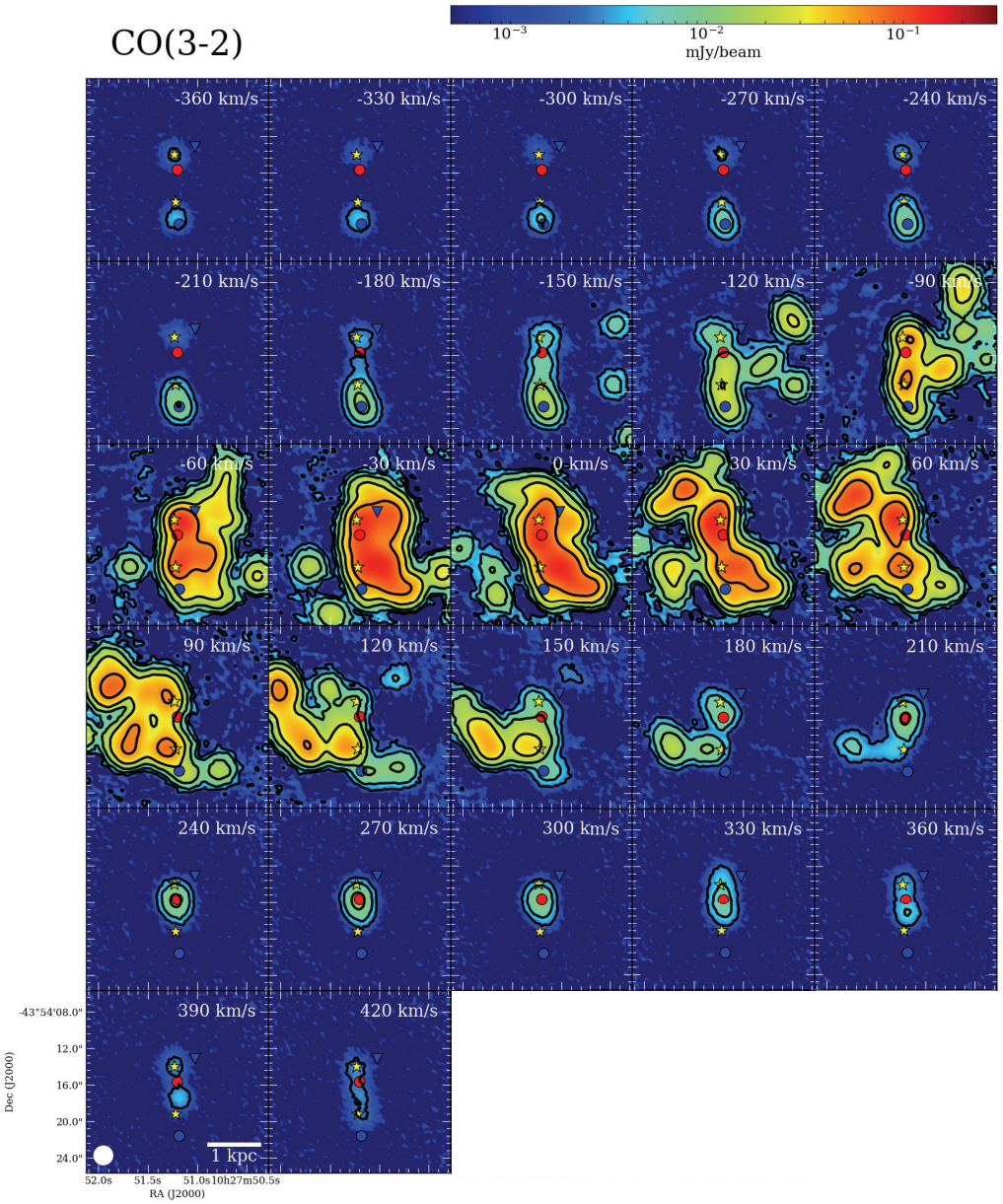

Figure 4.5 CO (3–2) channel map. The size of each map is 20 ″(3.4 kpc) square centered on RA. = $10^{\rm h}27^{\rm m}51\overset{\rm s}{.}18$, Dec. = $43^\circ54'17\overset{''}{.}85$. The black contours are at nσ($n = 3, 9, 27, 81$ and $\sigma = 9$ mJy beam^{-1}). The stars, circles, and a triangle are corresponding to the coordinates shown in Table 4.1.

more, I define “North-OF-Blue" as the peak position of the blue-shifted CO (1–0) emission located $\sim 2\farcs4$ north-west of the North-Nucleus. The exact coordinates of North-OF-Blue, North- Nucleus, OF-Red, South-Nucleus, and South-OF-Blue are shown in Table 4.1. Figure 4.6 (upper right) shows the schematic view of two bipolar outflows originally suggested by Sakamoto et al. (2014). Hereafter, the term “northern outflow" indicates the outflows from the northern nucleus and “southern outflow" indicates the outflow from the southern nucleus. The line flux of HCN (1–0) is 0.16 and 0.12 Jy km s^{-1} whereas HCO$^+$ (1–0) is 0.16 and 0.20 Jy km s^{-1} for the red- and blue-shifted emission, respectively. In addition, I integrate the same velocity range of the CO (1–0), CO (2–1), and CO (3–2) emission line (Figure 4.6 bottom).

Several differences are found between the distributions of dense gas (i.e. HCN (1–0) and HCO$^+$ (1–0)) and diffuse gas (i.e., CO) outflows. The dense gas outflows are identified at OF-Red and South-OF-Blue. They are undetected at North-OF-Blue (Figure 4.6). I find that the CO (1–0) fluxes in Figure 4.6 are 5.3, 1.9 and 2.2 Jy km s^{-1} for red-shifted emission around OF-Red, blue-shifted emission around North-OF-Blue, and blue-shifted emission around South-OF-Blue, respectively.[2] The CO (1–0) flux at OF-Red is likely the sum of the components from both the northern and the southern nuclei. I use the flux ratio between the blue-shifted components at North-OF-Blue and South-OF-Blue to estimate the fractional contribu-

[2]We note that the CO (1–0) fluxes in Sakamoto et al. (2014) are 8.9, 3.2, and 1.2 Jy km s^{-1} for red-shifted emission around OF-Red, blue-shifted emission around North-OF-Blue, and blue-shifted emission around South-OF-Blue, respectively. These values are different from our measurements. The difference between our CO (1–0) image and that of Sakamoto et al. (2014) is the uv-coverage, imaging parameters, and integrated velocity range. For OF-Red and North-OF-Blue, the fluxes measured in Sakamoto et al. (2014) are larger than our measurements. Since the data set used in Sakamoto et al. (2014) has compact uv-coverage than ours, these differences are due to spatially extended northern outflow. For South-OF-Blue, the flux measured in Sakamoto et al. (2014) is smaller than our measurements. This is due to the integrated velocity range. Using the velocity range of [-360,-240] for the blue-shifted components, the CO (1–0) flux is $\sim$ 1.1 Jy km s^{-1}, and our measurement is consistent with Sakamoto et al. (2014).

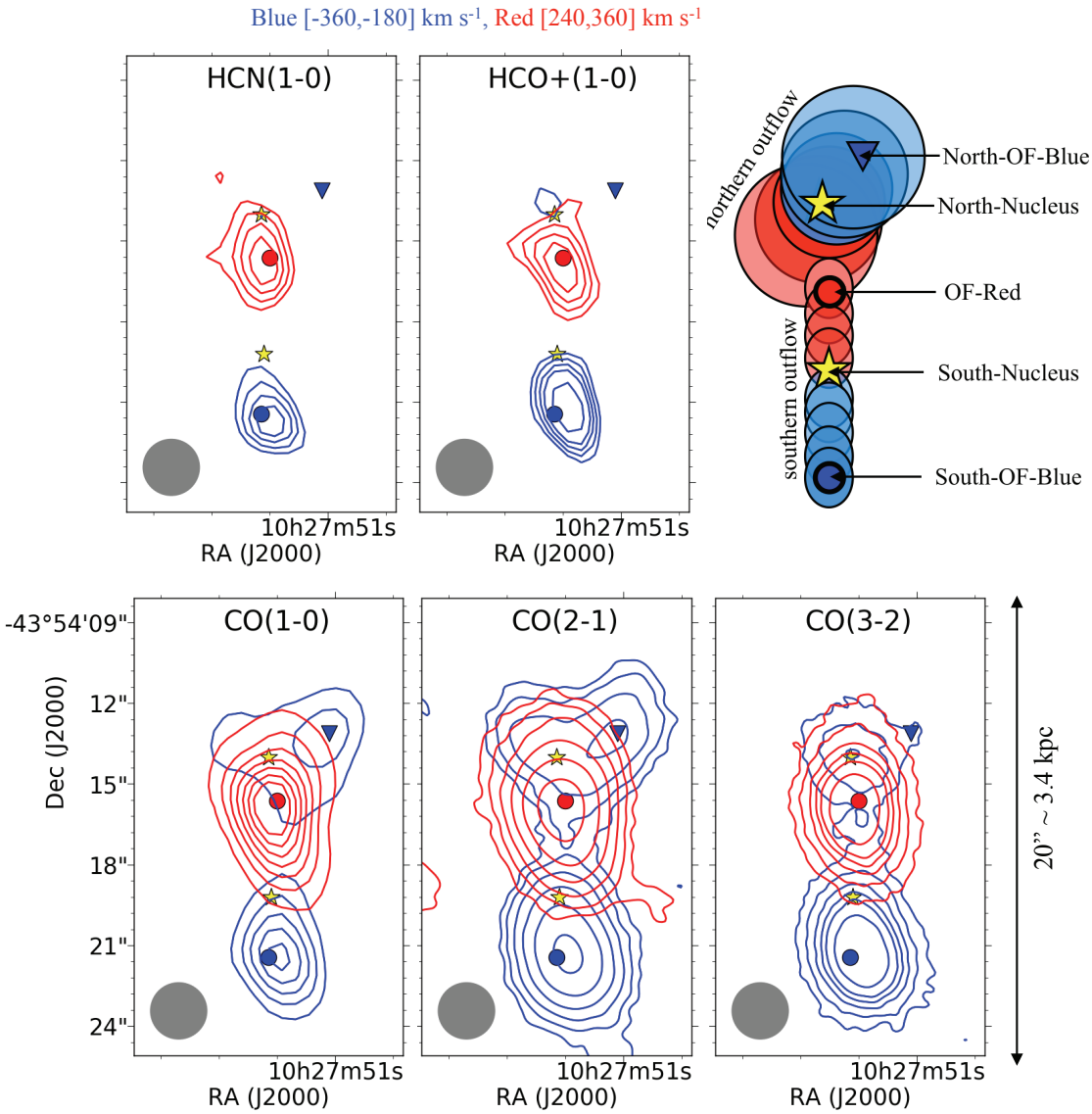

Figure 4.6 The spatial distribution of the extreme velocity components. The beams are restored by 2.″1. The size of these images are 10 ″× 20 ″(1.7 × 3.4 kpc) rectangle centered on RA. = $10^{h}27^{m}51.^{s}18$, Dec. = $43°54'17.''85$. Blue- and red-shifted gas are shown by blue and red contour respectively. The stars and circles correspond to the coordinates shown in Table 4.1. The contours are $0.02 \times (3,4,5,6)$ [Jy beam^{-1} km s^{-1}] for HCN (1–0), $0.02 \times (3,4,5,6,8)$ [Jy beam^{-1} km s^{-1}] for HCO^{+} (1–0), $0.1 \times (3,6,9,12,15,18,21)$ [Jy beam^{-1} km s^{-1}] for CO (1–0), $0.07 \times (3,9,27,54,81)$ [Jy beam^{-1} km s^{-1}] for CO (2–1), and $0.2 \times (3,9,18,27,36,54)$ [Jy beam^{-1} km s^{-1}] for CO (3–2). At top right panel, we show the schematic view of the outflows. These outflows are predicted by Sakamoto et al. (2014) based on CO observations. There are two bi-polar outflows (northern outflow and southern outflow), and we assume that red- and blue-shifted extreme velocity components of HCN (1–0) and HCO^{+} (1–0) is associated with southern outflow.

tion of the southern outflow at OF-Red. This means that the CO (1–0) line flux associated with the southern outflow is ~ 5 Jy km s^{-1}.

4.3.2 Outflow Properties

I estimate the dense gas mass associated with outflow independently from HCN (1–0) (dense gas mass $M_{\rm dense}$) and CO (1–0) (molecular gas mass $M_{\rm mol}$) using the luminosity to mass conversion factor $\alpha_{\rm HCN}$ and $\alpha_{\rm CO}$ [M$_\odot$ (K km s^{-1} pc^2)$^{-1}$];

$$\frac{M_{\rm dense}}{[{\rm M}_\odot]} = \alpha_{\rm HCN}\ \frac{L_{\rm HCN(1-0)}}{[{\rm K\ km\ s^{-1}\ pc^2}]} \tag{4.1}$$

$$\frac{M_{\rm mol}}{[{\rm M}_\odot]} = \alpha_{\rm CO}\ \frac{L_{\rm CO(1-0)}}{[{\rm K\ km\ s^{-1}\ pc^2}]} \tag{4.2}$$

where $L_{\rm HCN(1-0)}$ and $L_{\rm CO(1-0)}$ are the luminosities of the outflow calculated from the line flux derived in section 4.3.1. I use large systematic error due to the range of commonly adopted conversion factors; $\alpha_{\rm HCN} = [0.24, 10.0]$ and $\alpha_{\rm CO} = [0.8, 4.6]$ (Bolatto et al. , 2013b; Barcos-Muñoz et al. , 2018). I subsequently estimate the age (*Age*), outflow rate ($\dot{M}$), and kinetic energy ($P_{\rm kin,OF}$) (Cicone et al. , 2014) as follows.

$$\frac{Age}{\rm Myr} = \left(\frac{l_{\rm OF}}{\rm pc}\right)\left(\frac{V_{\rm OF}}{\rm km\ s^{-1}}\right)^{-1} \tag{4.3}$$

$$\frac{\dot{M}}{\rm M_\odot\ yr^{-1}} = 10^6\left(\frac{M_{\rm dense}\ {\rm or}\ M_{\rm mol}}{\rm M_\odot}\right)\left(\frac{Age}{\rm Myr}\right)^{-1} \tag{4.4}$$

$$\frac{P_{\rm kin,OF}}{\rm erg\ s^{-1}} = (3\times10^{35})\left(\frac{\dot{M}}{\rm M_\odot\ yr^{-1}}\right)\left(\frac{V_{\rm OF}}{\rm km\ s^{-1}}\right)^2 \tag{4.5}$$

where the $V_{\rm OF}$ is the representative velocity of the southern outflow, $l_{\rm OF}$ is the distance from the nucleus to the outflow. I use the de-projected outflow velocity of the southern outflow $V_{\rm OF} \sim 1600$ km s^{-1}, which is derived from the central value of the integrated range of blue-shifted components (Figure 4.1) assuming an inclination of

80° (Sakamoto et al. , 2014). The de-projected distance of l_{OF}=400 pc is estimated from the coordinates shown in Table 4.1. Table 4.2 shows the derived properties of southern outflows. Comparing the power of outflows and the kinetic power injected by supernovae, we can investigate whether southern outflow can be explained by supernovae explosions or not. The relation

$$\frac{P_{\rm kin,SF}}{\rm erg\ s^{-1}} = 7 \times 10^{41}\ \frac{SFR}{\rm M_\odot\ yr^{-1}} \tag{4.6}$$

derived by Veilleux et al. (2005) is used. The SFR of ~ 6 $M_\odot$ yr^{-1} [3] at the southern nucleus in the $\sim 3\farcs0$ region is adapted based on infrared SED fitting (Lira et al. , 2008). The power of the outflows is larger than the kinetic power from supernovae explosions ($P_{\rm kin,OF}/P_{\rm kin,SF}$ is $> 20\%$ and $> 100\%$ using $M_{\rm dense}$ and $M_{\rm mol}$, respectively). This suggests that the energy source such as an AGN is needed since $P_{\rm kin,OF}/P_{\rm kin,SF}$ is $\sim 1\%$ for pure starburst driven outflow (Cicone et al. , 2014; Pereira-Santaella et al. , 2018). This supports the CO outflow parameters and geometry suggested by Sakamoto et al. (2014), in which a weak or recently dimmed AGN likely to drive the southern outflow.

4.3.3 Line Ratio

The line flux associated with outflows and nuclei are measured in a consistent manner for all lines. For the two nuclei, all of the channels ([-390,390] km s^{-1}) with the signal to noise ratio of > 3 are integrated. For the extreme velocity components, only the channels defined in Section 4.3.1 (Figure 4.6) are integrated. In such case, the line flux does not include the entire outflowing gas since excluded channels closer to the systematic velocity contain the gas in the outflow at lower

[3] We note that this value is higher than the SFR derived by infrared SED fitting ($\sim$2 $M_\odot$ yr^{-1}) conducted by Sakamoto et al. (2014) based on the method introduced in Murphy et al. (2011).

Table 4.2 Southern outflow properties derived from HCN (1–0) and CO (1–0) observations.

Properties	Southern Outflow	
	HCN (1–0)	CO (1–0)
α_{CO} or α_{HCN} [$M_\odot$ (K km s^{-1} pc^2)$^{-1}$]	0.24–10	0.8–2.1
M_{dense} or M_{mol} [10^5 $M_\odot$]	2.8–120	100–260
V_{OF} [km s^{-1}]	1600	
l_{OF} [pc]	400	
Age [Myr]	0.25	
$\dot{M}$ [$M_\odot$ yr^{-1}]	1–48	40–104
log($P_{kin,OF}$) [erg s^{-1}]	42.0–43.6	43.5–43.9

velocity. Nonetheless, I mainly investigate the line ratios associated with outflows, and the absolute value of the line flux associated with outflow does not impact our conclusion. Three sigma upper limit are used for non-detection. Table 4.3 shows the measured line fluxes. Table 4.4 shows the line ratios ($R_{21/10}$, $R_{32/10}$, $R_{HCN/CO}$, $R_{HCO^+/CO}$, and R_{HCN/HCO^+}). I find that both $R_{HCO^+/CO}$ (i.e. dense gas fraction) and the $R_{32/10}$ are larger in the southern outflow (0.20±0.04 and 1.3±0.2, respectively) than in the southern nucleus (0.08±0.01, 0.7±0.1, respectively). Such trend is not seen for the northern outflow.

Table 4.3 Measured line flux for each region inner 2.1″ beam

region	velocity range	CO *J*=1–0	CO *J*=2–1	CO *J*=3–2	HCN *J*=1–0	HCO^+ *J*=1–0
	km s^{-1}	Jy km s^{-1}				
North-OF-Blue	[-360,-180]	0.5 ± 0.1	1.0 ± 0.1	<0.6	<0.06	<0.06
North-Nucleus	[-390,390]	36 ± 4	139 ± 14	280 ± 28	2.6 ± 0.3	2.8 ± 0.3
OF-Red	[240,360]	1.5 ± 0.2	5.3 ± 0.5	9.5 ± 1	0.08 ± 0.02	0.08 ± 0.02
South-Nucleus	[-390,390]	39 ± 4	142 ± 14	250 ± 25	1.1 ± 0.1	1.9 ± 0.2
South-OF-Blue	[-360,-180]	0.8 ± 0.08	4.1 ± 0.4	9.9 ± 1.0	0.07 ± 0.02	0.10 ± 0.02

Table 4.4 Line ratios in each region

region	$R_{21/10}$	$R_{32/10}$	$R_{HCN/CO}$	$R_{HCO^+/CO}$	R_{HCN/HCO^+}
North-Nucleus	1.0±0.1	0.9±0.1	0.12±0.02	0.13±0.02	0.94±0.13
North-OF-Blue	0.5±0.1	<0.1	<0.20	<0.20	-
OF-Red	0.9±0.1	0.7±0.1	0.09±0.02	0.09±0.02	0.99±0.34
South-Nucleus	0.9±0.1	0.7±0.1	0.05±0.01	0.08±0.01	0.60±0.08
South-OF-Blue	1.2±0.2	1.3±0.2	0.13±0.04	0.20±0.04	0.68±0.24

4.4 Radiative Transfer Modeling

4.4.1 RADEX *and Bayesian analysis*

It is expected that the physical condition (e.g., temperature and density) of the outflow can be substantially different from the ambient ISM. In order to investigate the physical conditions, a radiative transfer treatment is necessary. I use RADEX (van der Tak et al. , 2007) for the modeling of the non local thermodynamic equilibrium (non-LTE) radiative transfer. The physical conditions are derived based on CO (1–0), CO (2–1), CO (3–2), HCN (1–0), and HCO^+(1–0) for North-Nucleus, South-Nucleus, and South-OF-Blue. The assumptions are as follows. At first, background temperature assumed to be T_{bg} = 2.73 K. The CO and H_2 abundance ratio is assumed to be [CO/H_2] =1.0×10^{-4} since 15 % of C is in the form of CO with a cosmic value of (C/H)= 3×10^{-4} (Omont , 2007). The typical line width of 150 km s^{-1} (full width half maximum, FWHM) is used since FWHM of CO (2–1) emission at North-Nuclei and South-Nuclei are 160 and 112 km s^{-1}, respectively. The same calculations are conducted using 300 km s^{-1} and 50 km s^{-1}, and we find that the value of FWHM does not affect the results within one sigma range. These assumptions and RADEX modeling enable us to estimate line intensities based on kinetic temperature (T_{kin}), H_2 volume density (n_{H_2}), CO column density (N_{CO}), beam filling factor (FF), and the abundance ratio (N_{HCN}/N_{CO} and N_{HCO^+}/N_{CO}). Conversely, the parameters (T_{kin}, n_{H_2}, N_{H_2}, FF, N_{HCN}/N_{CO} and N_{HCO^+}/N_{CO}) can be estimated from

the multi-line intensities using Bayesian likelihood statistical analysis (Kamenetzky et al. , 2012). The best values of these parameters are searched within a range of $T_{\rm kin} = 5 - 6300$ K, $n_{\rm H_2} = 10^1 - 10^7$ cm^{-3}, $N_{\rm CO} = 10^{12} - 10^{22}$ cm^{-2}, $FF = 10^{-5} - 10^0$, $\rm N_{HCN}/N_{CO}$=$10^{-7} - 10^{-3}$, and $\rm N_{HCO^+}/N_{CO}$=$10^{-7} - 10^{-3}$. In order to avoid the non-physical condition, I assume that the length of the column does not exceed the diameter of the photometric beam size ($\sim$ 400 pc $\sim$ 2.1"). Similarly, I assume that the total mass does not exceed the virial mass ($M_{\rm dyn} = 1040\, R\, {\sigma_v}^2$; FWHM = $2.35\sigma_v$, R $\sim$200 pc) (Wilson & Scoville , 1990).

4.4.2 Results

Table 4.5 shows the results of the Bayesian likelihood statistical analysis. Figure 4.7 shows the relative probability function for the free parameters ($n_{\rm H_2}$, $T_{\rm kin}$, $N_{\rm CO}$, FF, $N_{\rm HCN}/N_{\rm CO}$ and $N_{\rm HCO^+}/N_{\rm CO}$) at South-Nucleus (black) and South-OF-Blue (blue). Except for the $N_{\rm CO}$ and FF, the one sigma range [4] (Table 4.5) of the estimated value is large, and the apparent offset between South-OF-Blue and South-Nucleus in the peaks (Figure 4.7) is mostly insignificant. The critical issue is that four lines are used for input parameters and five parameters are estimated, which results in the broad probability functions. The other issue is that assumption of a single phase ISM, which is not appropriate in the case of multiple phase ISM (e.g., warm and cold). Sliwa et al. (2014) and Saito et al. (2015) investigated the spatially resolved physical properties of the merging galaxies (NGC 1614 and VV 114) with similar analyses. Sliwa et al. (2014) suggest that the cold ($<$ 100 K) molecular gas component is dominant in NGC 1614. On the other hand, in NGC 3256, estimated one sigma range of $\rm T_{kin}$ is warmer than 100 K. In addition, South-OF-blue in NGC 3256 shows warmer $\rm T_{kin}$ and smaller $\rm N_{CO}$ than every region

[4]The one sigma range is estimated with the same manner conducted by Kamenetzky et al. (2012).

in NGC 1614. For the accurate estimation of physical conditions, it is necessary to use optically thin lines like ^{13}CO and/or high-J lines (Sliwa et al. , 2014; Saito et al. , 2015). Even though there are uncertainties, this analysis can be a first step for quantification of the physical conditions of the extra-galactic molecular outflow.

Table 4.5 The results of RADEX modeling

region	$T_{\rm kin}$ K	$n_{\rm H_2}$ cm^{-3}	$N_{\rm CO}$ cm^{-2}	FF	$N_{\rm HCN}/N_{\rm CO}$	$N_{\rm HCO^+}/N_{\rm CO}$
South-Nucleus	17 - 259	$10^{3.6}$ - $10^{6.0}$	$10^{18.4}$ - $10^{19.4}$	0.01 - 0.21	$10^{-5.9}$ - $10^{-4.1}$	$10^{-5.3}$ - $10^{-3.5}$
South-OF-Blue	33 - 254	$10^{4.3}$ - $10^{6.2}$	$10^{16.6}$ - $10^{17.7}$	0.0006 - 0.0055	$10^{-4.9}$ - $10^{-3.8}$	$10^{-4.7}$ - $10^{-3.3}$

4.5 Discussion

I can investigate the overall properties of the gas outflow such as the mass and velocities based on the diffuse gas observations using CO lines. A multi-line analysis including the dense gas tracers gives us additional information pertaining to the physical and chemical properties of the outflow. I assume that HCN and HCO$^+$ are collisionally excited and the $R_{\rm HCN/CO}$ and $R_{\rm HCO^+/CO}$ trace the dense gas fraction (e.g., Gao & Solomon , 2004; Bigiel et al. , 2015). In the following, I investigate the line ratios ($R_{\rm HCN/CO}$, $R_{\rm HCO^+/CO}$, $R_{21/10}$, and $R_{32/10}$) at the nucleus (i.e. North-Nucleus and South-Nucleus) and outflow components (i.e. South-OF-Blue, North-OF-Blue, and OF-Red) for both the northern and southern galaxy (Figure 4.8).

4.5.1 South-OF-Blue

The dense gas outflow is clearly detected in both HCN (1–0) and HCO$^+$ (1–0) at South-OF-Blue (Figure 4.6). I find that ~ 2 times larger dense gas fraction traced in $R_{\rm HCO^+/CO}$ at South-OF-Blue ($R_{\rm HCO^+/CO} = 0.20 \pm 0.04$) than South-Nucleus ($R_{\rm HCO^+/CO}$ = 0.08 ± 0.01) (Table 4.4 and Figure 4.8). The $R_{\rm HCN/CO}$ also shows same trend. In

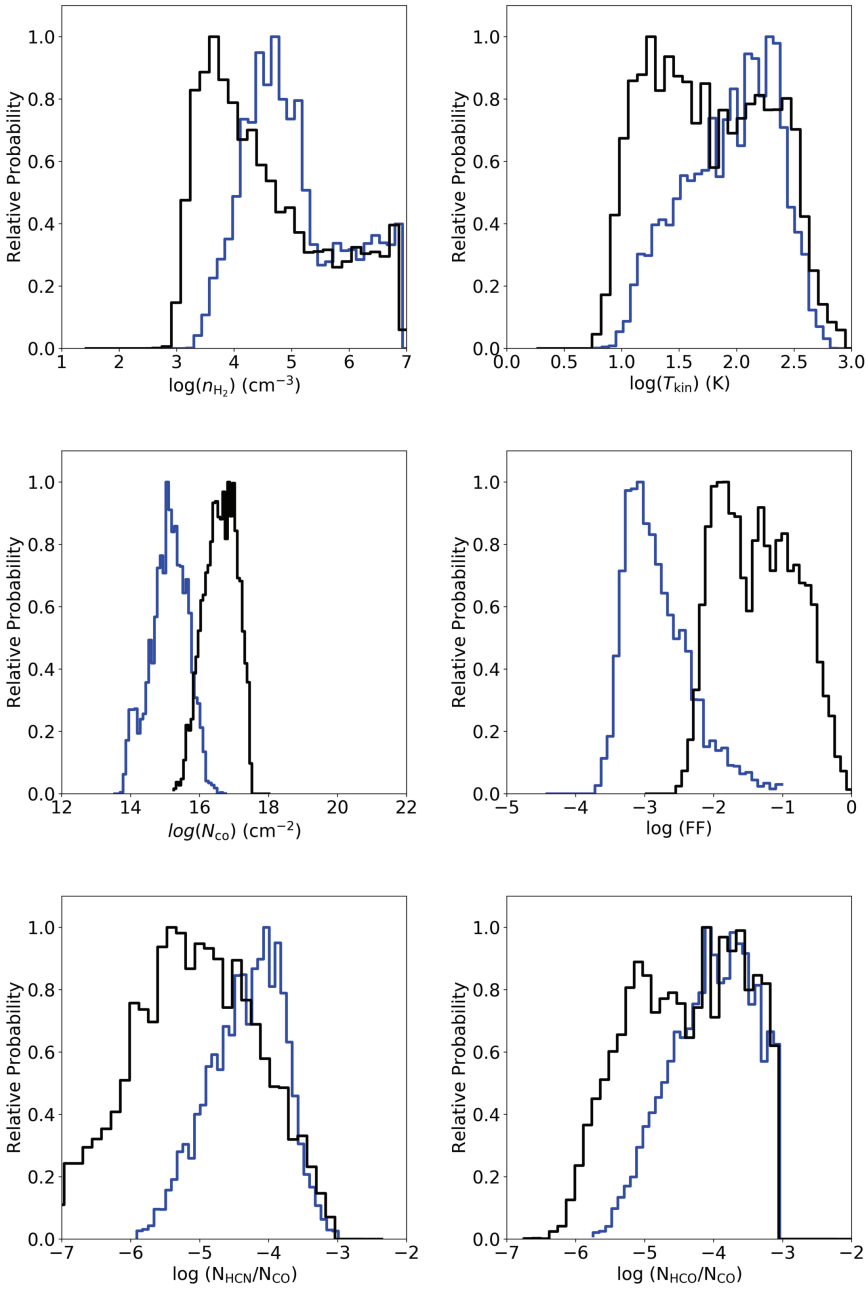

Figure 4.7 The results of RADEX modeling. We show the probability functions for each parameter measured by CO, HCN, and HCO^+ flux. The black lines show the relative probability function for each parameter at South-Nucleus. The blue lines show the relative probability function for each parameter at South-OF-Blue.

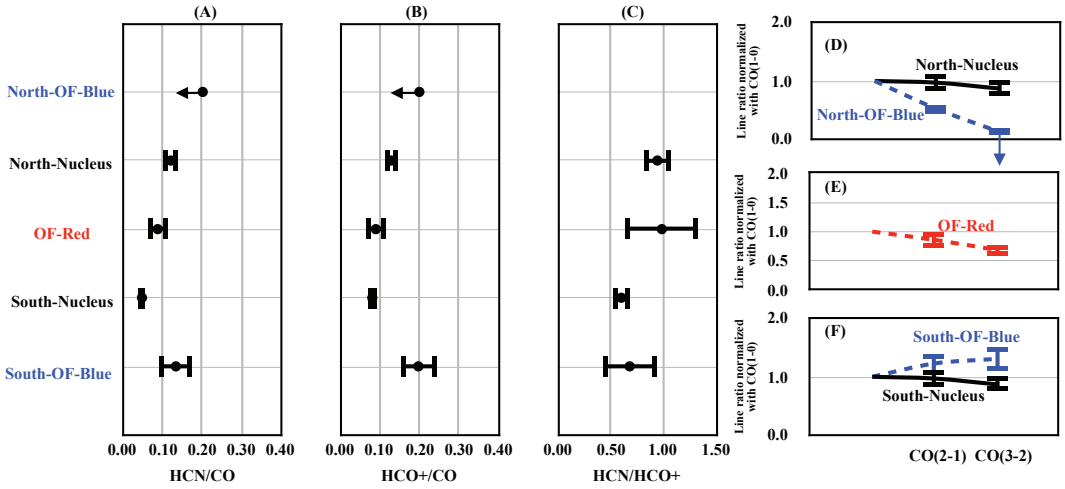

Figure 4.8 (A)-(C) Line ratios for each region. The panels show the (A) $R_{\rm HCN/CO}$, (B) $R_{\rm HCO^+/CO}$, and (C) $R_{\rm HCN/HCO^+}$. The dense gas fraction traced by $R_{\rm HCN/CO}$ and $R_{\rm HCO^+/CO}$ is similar or smaller at North-OF-blue and larger at South-OF-blue than the nucleus. (D)-(F) CO spectral line energy distribution up to J=3 for each region; (D) North-OF-Blue and North-Nucleus, (E) OF-Red, (F) South-OF-Blue and South-Nucleus. A decreasing trend is seen at North-OF-Blue, and an increasing trend is seen at South-OF-Blue. The values are shown in Table 4.4.

addition, I find a factor of two larger $R_{21/10} = 1.2 \pm 0.2$ and $R_{32/10} = 1.3 \pm 0.2$ at South-OF-Blue than at South-Nucleus ($R_{21/10} = 0.9 \pm 0.1$ and $R_{32/10} = 0.7 \pm 0.1$). These results suggest that dense gas fraction is larger and excitation condition is higher in the South-OF-Blue than in the South-Nucleus, which means that the ISM is significantly altered due to the energy input from the powerful outflow. The `RADEX` modeling also suggest the higher $T_{\rm kin}$ and $n_{\rm H_2}$ (Figure 4.7) in South-OF-Blue compared to South-Nucleus, while the one sigma range is large.

I further investigate variation in the line ratio as a function of velocity (Figure 4.9 and 4.10), and I show the line ratios against the absolute value of velocity offset at OF-Red and South-OF-Blue in Figure 4.11. In the case of South-OF-Blue, I find the increase of the dense gas fraction towards the largest velocity offset (e.g.,

$R_{\rm HCN/CO} = 0.22 \pm 0.03$ at -240 km s^{-1} and 0.32 ± 0.05 at -300 km s^{-1})(Figure 4.11). On the other hand, the $R_{32/10}$ and $R_{21/10}$ decrease towards the largest velocity offset (e.g., $R_{32/10} = 2.3 \pm 0.2$ at -240 km s^{-1} and 1.4 ± 0.2 at -360 km s^{-1}).

I can not explain such difference when HCN (1–0), HCO$^+$(1–0), CO (2–1) and CO (3–2) trace the same gas. It is possible that the gas with the largest velocity offset is efficiently compressed into dense gas clumps while diffuse gas outflow is outspread. Therefore, one possible explanation is a two-phase gas in the outflow; i.e., dense clumps are traced by HCN (1–0) and HCO$^+$ (1–0) and diffuse gas are traced by CO lines. Figure 4.12 shows the schematic view of the blue-shifted part of southern outflow. This also explains the large uncertainty of the Bayessian estimation for the $T_{\rm kin}$ and $n_{\rm H_2}$ due to the assumption of single phase gas. Such multi-phase outflows can be produced due to the jet and ISM interaction (Zubovas & Nayakshin , 2014; Costa et al. , 2015; Ferrara & Scannapieco , 2016) in numerical simulations. This formation process is supported by the detection of a collimated structure detected by the VLA (Neff et al. , 2003) whose spatial distribution is consistent with the outflow detected in CO (Sakamoto et al. , 2014). In addition, the detection of near-IR H_2 emission lines suggests the gas heated by X-ray or shock in the southern outflow (Emonts et al. , 2014).

The similar characteristics with southern outflow are seen in the case of galaxies hosting the strong radio jet (IC 5063 and M51). IC 5063 is a massive radio loud elliptical galaxy with a Seyfert 2 nucleus (Morganti et al. , 2013; Tadhunter et al. , 2014; Dasyra et al. , 2015; Morganti et al. , 2015; Dasyra et al. , 2016). Based on the observation of near-IR H_2 lines, Tadhunter et al. (2014) suggest the fast shock into the ISM due to the radio jet expansion. The higher excitation condition in the jet driven outflows is suggested from the CO (4–3) / CO (2–1) in IC 5063 (Dasyra et al. , 2016) in which CO (4–3) / CO (2–1) is over unity (in brightness temperature

Line ratios for blue-shifted components

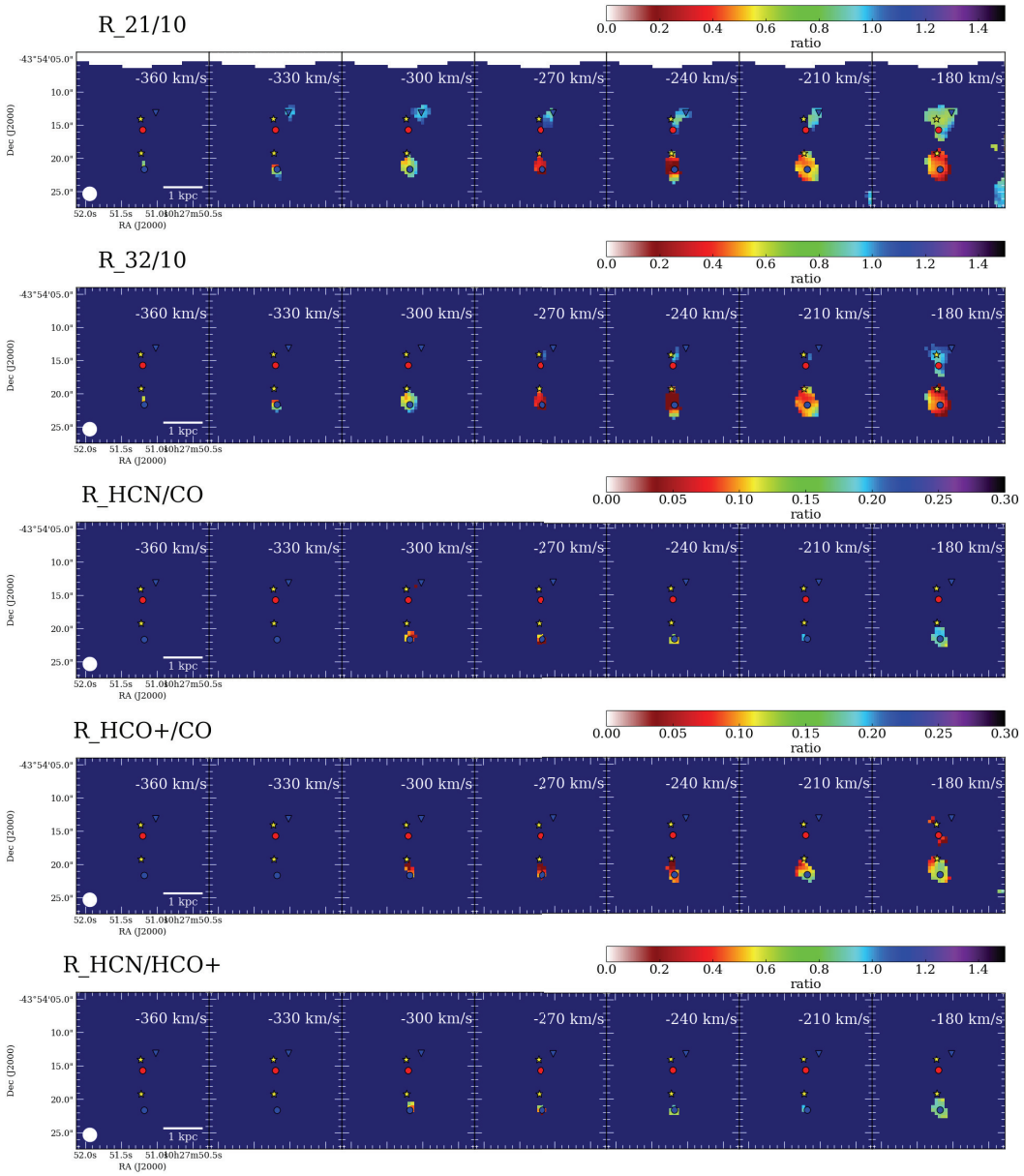

Figure 4.9 Line ratios for blue-shifted components. Symbols are the same as Figure 4.1. The size of each map is 20 ″(3.4 kpc) square centered on RA. = $10^{h}27^{m}51\overset{s}{.}18$, Dec. = 43°54′17.″85.

Line ratios for red-shifted components

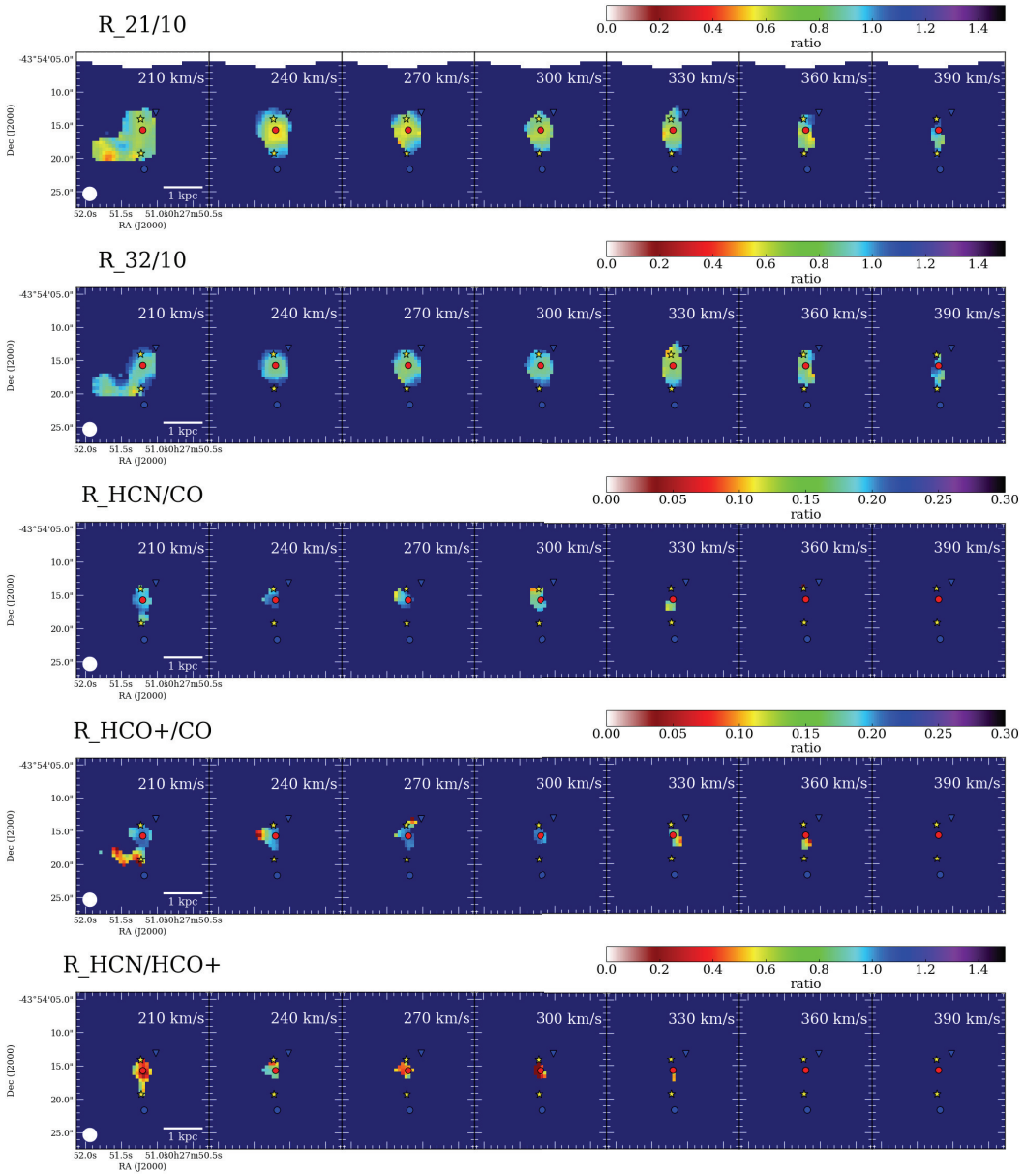

Figure 4.10 Line ratios for red-shifted components. Symbols are the same as Figure 4.1. The size of each map is 20 ″(3.4 kpc) square centered on RA. = $10^{h}27^{m}51\overset{s}{.}18$, Dec. = 43°54′17.″85.

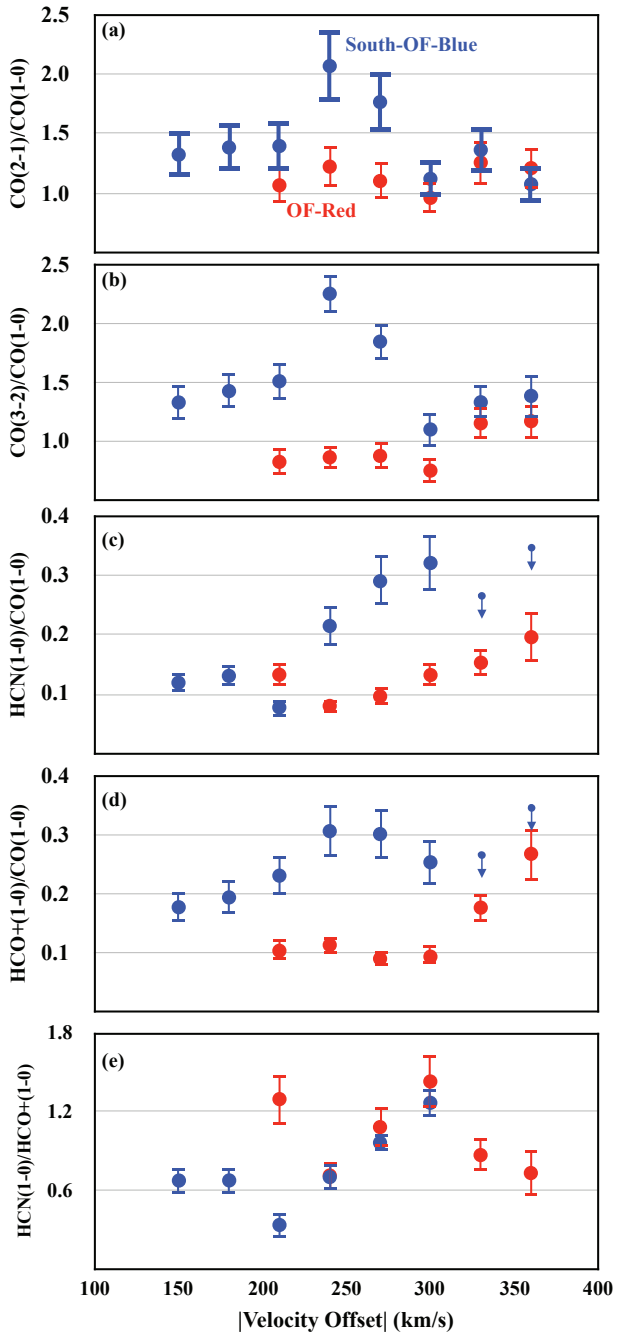

Figure 4.11 The relation between absolute value of velocity offset and the line ratios; (a)$R_{21/10}$, (b)$R_{32/10}$, (c)$R_{\rm HCN/CO}$, (d)$R_{\rm HCO^+/CO}$, and (e)$R_{\rm HCN/HCO^+}$. The blue shifted components (blue) are for South-OF-Blue, and red shifted components (red) are for OF-Red. At South-OF-Blue, low-J CO ratio decreases towards the largest velocity offset, on the other hand, dense gas fraction increases. The arrows show 5 sigma upper limits. This difference is probably due to two-phase ISM in the outflow. In addition, $R_{\rm HCN/HCO^+}$ increases towards the largest velocity offset, and one possible explanation is that shock is dominant in the outflow.

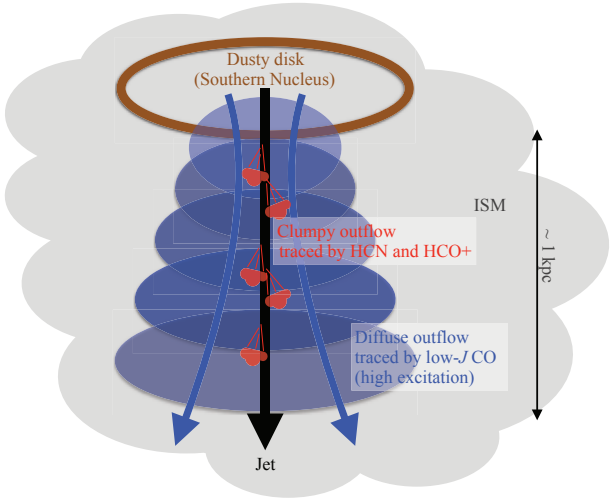

Figure 4.12 A schematic view of expected feature of the blue-shifted components of southern outflow in NGC 3256 (South-OF-Blue). There are clumpy and diffuse gas outflow. The gas with the largest velocity offset is efficiently compressed into dense gas clumps due to a jet-ISM interaction. Such clumps possibly lead future star formation.

unit) at the gas associated with outflows.

In the case of M51, Matsushita et al. (2015) show large $R_{\rm HCN/CO} > 1$ for the outflow associated with the AGN jet based on the map obtained at $\sim$ 34 pc resolution at the Submillimeter Array (SMA), which suggests that HCN is enhanced in shocks. Assuming that the dense gas is only associated with the shock front of the jet-ISM interaction in NGC 3256, the beam filling factor of HCN can be smaller than CO. This means that if the outflows are observed with better resolution (e.g., $\sim$30 pc), $R_{\rm HCN/CO}$ possibly shows > 1 at the edge of the outflow.

On the other hand, the outflow associated with AGN seen in Mrk 231 shows different characteristics from the southern outflow in NGC 3256. In the case of Mrk 231, the lower excitation condition in the wings than the core is suggested ($R_{21/10} \sim 0.8$ in the core but < 0.8 in the outflow) (Cicone et al. , 2012). Cicone

et al. (2012) suggest an acceleration by radiation pressure on the dust in molecular clouds (Fabian et al. , 2009) without interactions between the jet and ISM of the host galaxy in order to explain the lower excitation outflow in Mrk 231. In addition, (Aalto et al. , 2012) shows that $R_{\rm HCN/CO}$ in the outflow of Mrk 231 is higher (~ 0.6) than $R_{\rm HCN/CO}$ at South-OF-Blue. The reason for such differences is not clear. A major difference is that NGC 3256S is not in a QSO phase as in Mrk 231, but it is a low luminosity AGN.

Summarizing the characteristics of the southern outflow, it has higher excitation condition and larger dense gas fraction than in the southern nucleus. In addition, the southern outflow is possibly a two-phases (dense clumps traced by HCN and HCO^+ and diffuse components traced by low-J CO) outflow. The next issue is the possibility for the star formation in such dense clumps. Dugan et al. (2014); Wagner et al. (2016) shows that jet-ISM interaction can lead to the formation of new massive stars in the numerical simulations. I use the empirical relation between SFR and dense gas mass (SFR [$M_\odot$ yr^{-1}]= $10^{-7.93} \times M_{\rm dense}^{1.02}$) (Usero et al. , 2015) in order to estimate the SFR associated with southern outflow. We estimate SFR = 0.004-0.2 [$M_\odot$ yr^{-1}] from dense gas mass associated with outflow ($M_{\rm dense}$ = $(2.8-120) \times 10^5$ [$M_\odot$]). Compared to the total SFR of $\sim 41\ M_\odot$ yr^{-1}, this estimated SFR in the outflow is too small to be recognized as a positive feedback. A more direct observational evidence of positive feedback is necessary, and it requires high resolution observations that trace the star formation acticvity.

4.5.2 North-OF-Blue

Unlike CO observations, extreme velocity components of HCN (1–0) and HCO^+ (1–0) are not detected at North-OF-Blue. It is difficult to compare the dense gas fraction between the northern nucleus and the outflow since our observation sensitivity

is not sufficient to derive meaningful upper limit. I find that $R_{32/10}$ and $R_{21/10}$ are lower ($R_{21/10} = 0.5 \pm 0.1$, $R_{32/10} < 0.1$) at North-OF-Blue (dotted blue line in Figure 4.8 (D)) than the North-Nucleus ($R_{21/10} = 1.0 \pm 0.1$, $R_{32/10} = 0.9 \pm 0.1$) (solid line in Figure 4.8 (D)). A possible explanation is that the outflow has lower or similar excitation condition compared to the northern nucleus, assuming that all CO lines are optically thick at North-Nucleus. This suggests that the gas is expelled from the nucleus with little interaction between the outflow and the ISM. The similar trend is seen at the starburst galaxy M82 that has $R_{32/10} = 1.1 \pm 0.2$ around the nucleus and 0.4 ± 0.2 in the outflow (Weiß et al. , 2005). Finally, the note is that the moment 0 map of the blue-shifted CO (2–1) component around North-Nucleus and North-OF-Blue shows the V-like shape in the moment 0 map. The directions of the CO (1–0) and CO (3–2) outflow are different and faint CO (3–2) is detected around North-OF-Blue (Figure 4.6). This suggests that it arises from two different outflows and such V-like shape outflow is reported at different scales, for example, AGN jet in Circinus (Marconi et al. , 1994) and outflow cavity from low mass protostars (Zhang et al. , 2016). A higher resolution and sensitivity are necessary for further investigation.

4.5.3 OF-Red

Dense gas outflow traced in HCN (1–0) and HCO^+ (1–0) is detected at OF-Red (Figures 4.1-4.6). At OF-Red, both the southern and northern outflow can contribute to the red-shifted extreme gas components. For CO observations, I assume 54% and 46% of the red-shifted components arise from the southern and northern nucleus, respectively (Sakamoto et al. , 2014). On the other hand, since the dense gas tracers are not detected at North-OF-Blue, it is assumed that 100% of the red-shifted components arise from the southern nucleus in the case of HCN and HCO^+.

This indicates that the outflow emanating from the southern nucleus is denser than the northern outflow (Figure 4.6). The dense gas fraction at OF-Red is a factor of a few smaller than at a South-OF-Blue at given absolute velocity offset (Figure 4.11). If it is assumed that 54% of the CO red-shifted components arise from the southern outflow, the dense gas fraction increases by a factor of two. In such case, a symmetric bi-polar southern outflow between red- and blue-shifted components can be explained in terms of the dense gas fraction. Furthermore, dense gas fractions increase at the largest velocity offset (Figure 4.11). For example, $R_{\rm HCN/CO}$ is 0.08 ± 0.01 at +240 km s^{-1} and 0.20 ± 0.04 at +360 km s^{-1}. This trend is also seen at South-OF-Blue and suggests that the gas is efficiently compressed into dense clumps with the largest velocity offset.

4.5.4 Shock in the outflow

It is suggested that the HCN and HCO$^+$ outflows detected in South-OF-Blue can be a multi-phase outflow that is formed due to the jet-ISM interaction. This possibly means the shock enhancement (Goldsmith & Pittard , 2017), as suggested by Emonts et al. (2014) showing the possibility for the shock heated outflow from their near-IR H_2 observation. In this section, I investigate the chemical properties of the outflows from HCN (1–0) and HCO$^+$ (1–0) line ratio. The conventional idea is that shocks reduce the abundance of HCO$^+$ while leaving the HCN abundance unchanged (Iglesias & Silk , 1978; Elitzur , 1983; Mitchell , 1983; Harada et al. , 2015). In LIRGs, Papadopoulos (2007) suggest that the HCO$^+$ abundance could be reduced in the highly turbulent molecular gas where shocks are expected to be frequent. Burkhardt et al. (2016) investigate the protostellar outflow with multi-line and find that HCN and shocked gas tracers (e.g., CH_3OH, HNCO) can be seen at the edge of the outflow but HCO$^+$ is not. In addition, Lindberg et al. (2016)

show that HCN/HCO^+ ratio is enhanced in the outflow of Mrk 231 based on PdBI observations. In the case of the outflow at South-OF-Blue in NGC 3256, R_{HCN/HCO^+} increases towards the largest velocity offset, i.e., R_{HCN/HCO^+} is 0.34 ± 0.06 at -240 km s^{-1} and 1.27 ± 0.20 at -360 km s^{-1} at South-OF-Blue. In contrast to South-OF-Blue, there is no clear enhancement of R_{HCN/HCO^+} toward the largest velocity offset at OF-Red. The difference can be probably due to the orientation of the two galaxies. A coexistence of the ISM belonging to the NGC 3256N and NGC 3256S toward the direction of OF-Red makes it easy to enhance R_{HCN/HCO^+} entire extreme velocity components (from low to high velocity) at OF-Red. In addition, the red-shifted HNC wing is also detected at OF-Red (Harada et al. , 2018), which suggests stronger shock in the red-shifted outflow since HNC emission is expected in shock and/or dense warm gas (e.g., Aalto et al. , 2002).

The HCN and HCO^+ line ratio is insufficient to draw a conclusion for shock enhancement. For example, the HCO^+ abundance increase behind a shock front in a diffuse cloud ($\sim 3 \times 10^4$ cm^{-3}) through reaction of C^+ and O (Ziurys et al. , 1989; Mitchell , 1983). For additional clues, it is necessary to observe shock gas tracers (e.g., CH_3OH, SiO, HNCO) in the outflow. In the same data set presented here, shock gas tracers are simultaneously observed. However, the sensitivity was not enough to detect the extreme velocity components of these lines since the line flux is more than 10 times lower than HCN (1–0) and HCO^+ (1–0). Based on the spatial distribution of these shock gas tracers, Harada et al. (2018) suggest the shock enhancement in the outflow.

The possible solution to identify the enhancement of shocks is to search for H_2O line in the outflow. H_2O is the most abundant molecule in the grain mantle (Yamamoto , 1985) and H_2O abundance is enhanced if the grain mantels are progressively eroded by shock (Flower & Pineau des Forêts , 2010). The brightness of

H_2O is comparable to high-J CO (Yang et al. , 2013; Falstad et al. , 2015). H_2O lines in LIRGs have already been reported (König et al. , 2017), and future high resolution and sensitivity H_2O observations are the keys to investigate the shocks in extragalactic outflows.

4.6 High Resolution CO (2–1) image

Finally, Figure 4.13 shows the highest resolution (0.16" $\sim$ 27 pc) image of the southern outflow in ALMA archive (ALMA Project ID: 2015.1.00714.S). I only use the data obtained with 12m array in 1st and 7th September 2016 in order to focus on compact structure in the outflows. The image is made using the tclean task in `CASA` (version 5.1.2, Briggs weighting, robust = 2.0) with automatically masking loop auto-multithresh (sidelobethreshold=2.0, noisethreshold=3.0, lownoisethreshold=2.0, minbeamfrac=0.3, growiterations=75, and negativethreshold=0.0). The clumpy structures are detected in both blue- and red-shifted components at similarly large velocity offsets. In order to identify the clumps, I use two dimensional fitting tool (`2D Fit tool`) in `CASA`. Four clumps (B1-B4) are identified in blue-shifted components and three (R1-R3) in red-shifted components. The size of clumps are measured as the half light radius of the components by 2D fitting for ellipticals. The fitting results are shown in Figure 4.14 and Table 4.6. The fitting shows the size of clumps is 34-105 pc and the mass is $(0.3-6.7)\times10^7\,M_\odot$. In order to investigate the velocity dispersion of the clumps in the southern outflow, I check the line profile for each clump. Double gaussian is fitted to the line profile at B3, B4, R1, R2 and R3. The fitting results are shown in Figure 4.15. In the case of B1 and B2, it is difficult to separate outflow components and rotating disk since the peak of second components are not clear. Finally, Table 4.6 shows the summary of the clump properties. The virial masses are calculated by using the equation from Donovan Meyer et al.

(2013)

$$\frac{M_{\rm vir}}{\rm M_\odot} = 1040 \left(\frac{R}{\rm pc}\right) \left(\frac{\sigma_v}{\rm km\ s^{-1}}\right)^2 \tag{4.7}$$

Comparing the clumps in the southern outflow with GMCs in nearby galaxies and Milky Way using the data presented in Tosaki et al. (2017), clumps in the southern outflow of NGC 3256 show higher velocity dispersion than the same size clumps in the normal galaxies (Figure 4.16). In addition, all the clumps have the $M_{\rm vir}/M_{\rm H_2}$ ratio of > 1. These results suggest that the clumps in the outflows are not gravitationally bound due to high turbulence. This can be an indirect evidence of shocked gas clumpy outflow, which is suggested by line ratios in previous sections. I note that the effective radius shown in Table 4.6 and Figure 4.16 possibly miss the extended structure. However, in order to explain the velocity dispersion of > 50 km s^{-1} by Larson's law (Larson , 1981), the effective radius should be > 1 pc. In addition, the difference of the clump find algorithm and resolution there are possibly systematic offset between my work and Tosaki et al. (2017).

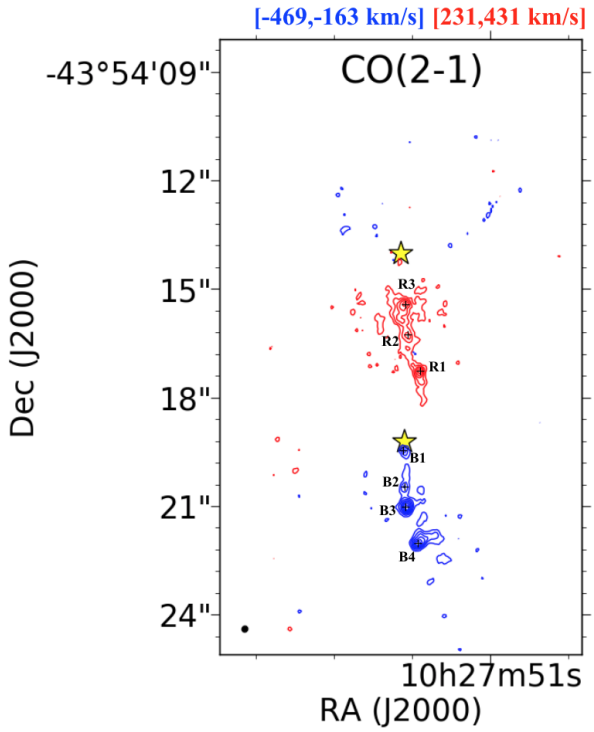

Figure 4.13 The high resolution ($0.17 \times 0.16''$) image of CO (2–1) outflow from ALMA archive. We identify the clumps (B1-B4 for blue-shifted components, R1-R3 for red-shifted components).

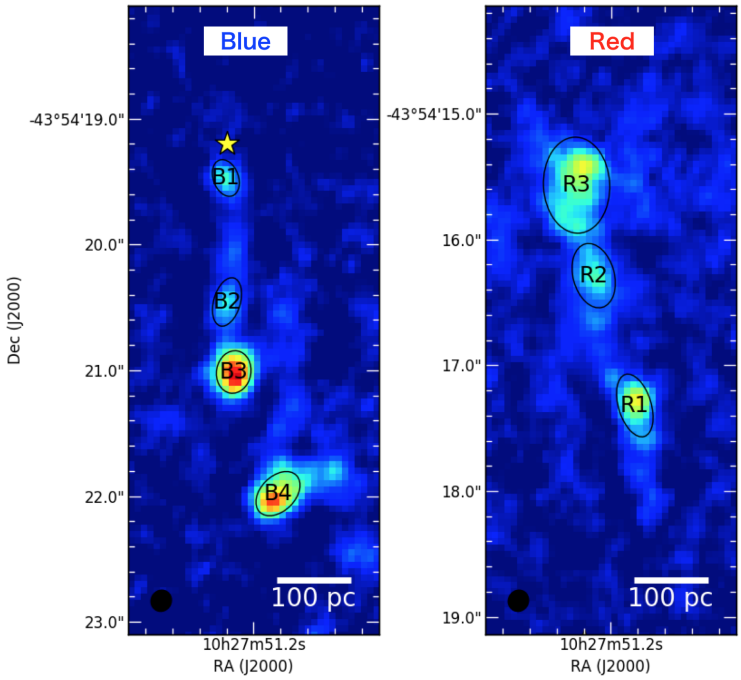

Figure 4.14 The results of two dimensional fitting for the clumps in the outflow. Figure 4.15 shows the spectrums for each clump. Table 4.6 shows the properties of each clump.

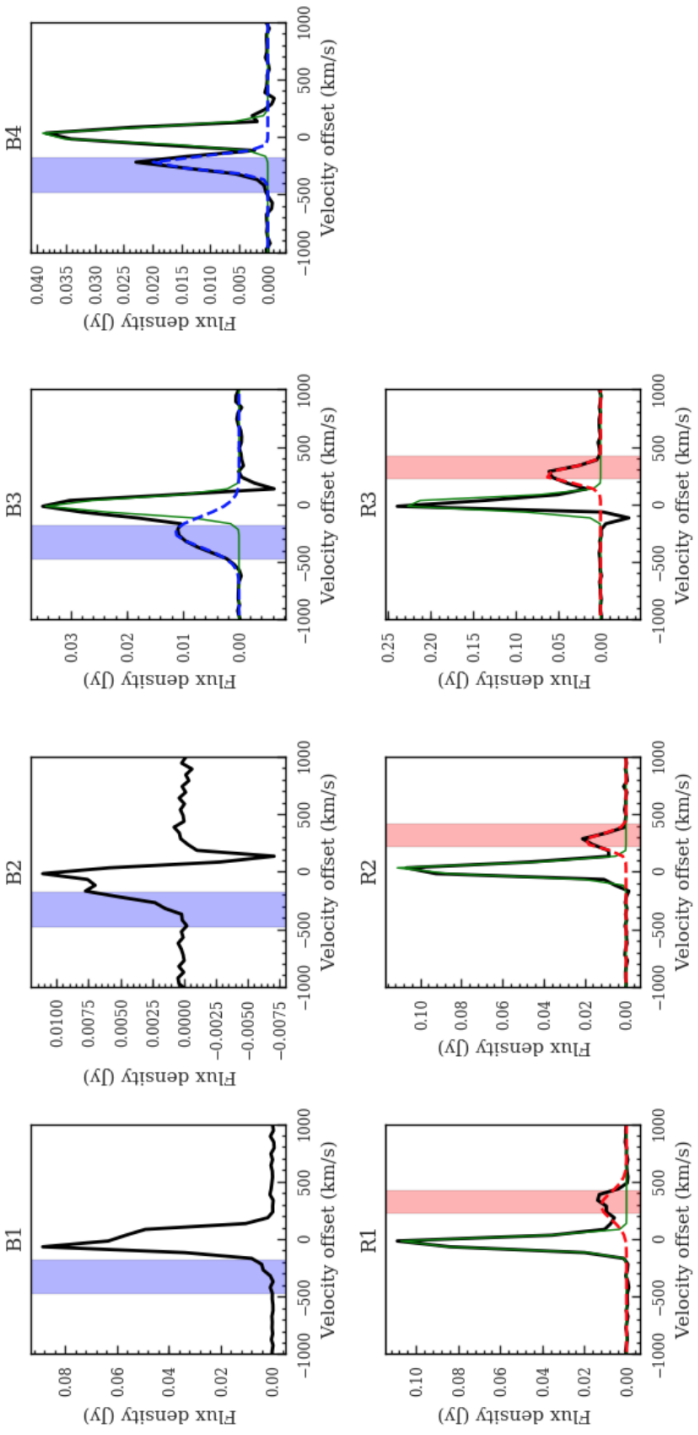

Figure 4.15 The results of double gaussian fitting at the outflow positions. Black is the original spectrum, and the green is the main component associated with rotating disk, and the blue and red is the blue- and red-shifted second components. We assume these blue and red components as outflow. We do not conduct gaussian fitting when the peak of second components are not clear (B1 and B2).

Table 4.6 The properties of clumps in outflow

Label	RA	Dec	Maj	Min	PA	$R_{\rm eff}$	σ_v	Δv	flux	$M_{\rm H_2}$	$M_{\rm vir}$	$M_{\rm vir}/M_{\rm H_2}$
			arcsec	arcsec	degree	pc	km s^{-1}	km s^{-1}	Jy km s^{-1}	$M_\odot$	$M_\odot$	
B1	10:27:51.221	-43.54.19.5	0.32±0.01	0.19±0.01	19±0.9	42	-	-	0.9	3.1E+06	-	-
B2	10:27:51.200	-43.54.20.5	0.31±0.01	0.13±0.01	162±1.6	34	-	-	1.0	3.4E+06	-	-
B3	10:27:51.215	-43.54.21.0	0.30±0.02	0.23±0.02	172±9.6	44	131	-229	7.5	2.6E+07	7.8E+08	30.7
B4	10:27:51.179	-43.54.22.0	0.51±0.07	0.24±0.04	121±6.8	60	56	-215	5.6	1.9E+07	1.9E+08	10.1
R1	10:27:51.182	-43.54.17.3	0.46±0.06	0.21±0.03	16±5.6	52	119	300	7.2	2.4E+07	7.7E+08	31.4
R2	10:27:51.212	-43.54.16.3	0.40±0.02	0.26±0.01	3±9.6	55	58	277	6.0	2.0E+07	1.9E+08	9.3
R3	10:27:51.225	-43.54.15.6	0.74±0.08	0.52±0.05	3±11.6	105	59	266	19.6	6.7E+07	3.9E+08	5.8

4.7 Chapter Summary

I present the detections of dense gas outflows in NGC 3256 based on ALMA HCN (1–0) and HCO^+(1–0) observations. Investigating the line ratios ($R_{HCN/CO}$, $R_{HCO^+/CO}$, R_{HCN/HCO^+}, $R_{21/10}$, and $R_{32/10}$) for outflows and nuclei in NGC 3256, I characterize the physical and chemical properties in the outflows. My findings are as follows.

(1) The extreme velocity components of HCN (1–0) and HCO^+ (1–0) are not detected at North-OF-Blue, which means that there is no signature of dense gas outflow in the starburst driven northern outflow. The $R_{21/10}$ and $R_{32/10}$ ratios are comparable between the northern outflow and the northern nucleus. This suggests that the gas is expelled from the starburst region without experiencing large physical or chemical changes.

(2) I clearly identify the dense gas in the southern outflow emanating from the low-luminosity AGN in the southern nucleus. Investigating line ratios, I find that both the dense gas fraction and $R_{32/10}$ ratios are larger in the outflow than in the nucleus. This suggests that warm and dense gas in the southern outflow, and non-LTE modeling also supports this idea.

(3) For the southern outflow, I additionally find that the dense gas fraction increases and $R_{32/10}$ decreases towards the largest velocity offset. One possible situation is the existence of a two-phase (diffuse and clumpy) outflow. Such a two-phase outflow can be produced by a jet-ISM interaction, which possibly triggers the shock and/or star formation in the outflow. However, it is difficult to investigate star formation activity in the southern outflow.

(4) The increase of R_{HCN/HCO^+} suggests the shock enhancement in the southern

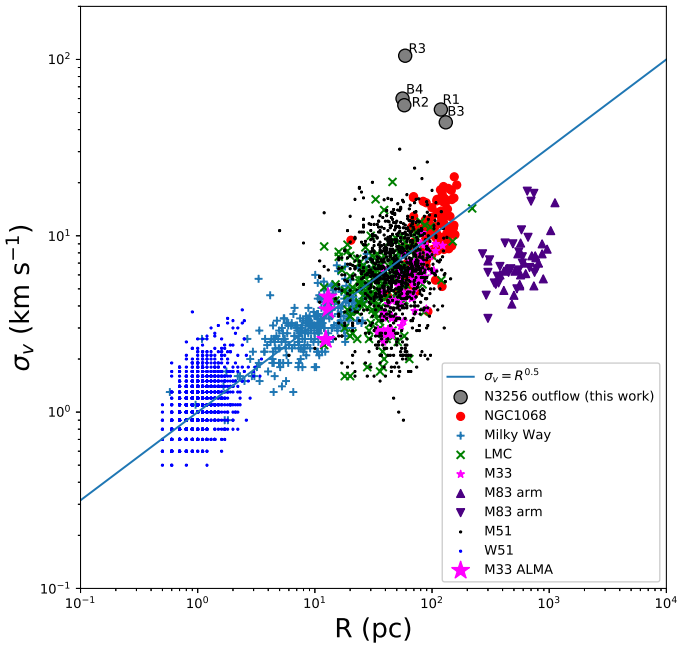

Figure 4.16 Comparison between clumps in nearby galaxies, Milky Way, and clumps in the southern outflow of NGC 3256. The GMCs in this diagram are from Tosaki et al. (2017). We find that the clumps show higher velocity dispersion than the same size clumps in the normal galaxies. This might suggests that the clumps are not gravitationally bounded due to high turbulence.

outflow due to a jet-ISM interaction. However, it is necessary to detect additional multi-molecule in the outflow in order to investigate chemical properties inside the outflow.

(5) Finally, I find clumps in the southern outflow by using the highest resolution ($\sim$ 0.16") CO (2–1) imaging data. I conclude that the clumps in the southern outflow are not gravitationally bounded. This result also supports the idea of shocked gas clumpy outflow suggested by the line ratio analysis.

5 | Conclusion

5.1 Summary

In this thesis, I have conducted millimeter/submillimeter observations toward merging galaxies. In chapter 2, I presented a survey observation of merging galaxies using ASTE and AKARI. In chapter 3 and 4, I showed the ALMA observations of one merging galaxy NGC 3256 as a case study. Through these observations, I will answer the key questions introduced in section 1.5.

- **Is star formation relation universal between normal galaxies and mergers?**

  No. I found that normal isolated spiral galaxies and merging galaxies have different slopes (α) in the $\log L_{\rm CO} - \log L_{\rm FIR}$ plane: $\alpha \sim 0.8$ for disk galaxies and ~ 1.1 for merging galaxies. This means that merging galaxies fill the gap between disk- and starburst-sequence. This supports the model based on Teyssier et al. (2010); Bournaud (2011). In their model, they predicted that the spatially extended starburst (due to fragmentation of high-dispersion gas outer the nuclear region) is equally important especially in the early phase as well as nuclear starburst (due to massive inflow) in the late phase.

- **Where and how much is the starburst triggered during the merger process?**

  My conclusion is that the contribution of the disk-wide starbursts is larger than dusty nuclear starbursts. While the importance of disk-wide starbursts was recognized in previous literature, dust-enshrouded nuclear starbursts were

possibly missed. The key in my project is that I use both VLT IFU (i.e., Hα and Hβ) and ALMA (i.e., H40α and H42β) observation. The synergy between VLT and ALMA enables us to directly quantify the SFR at diffuse disk-wide star forming region and dusty nuclear starbursts.

As a case study, I observed merging galaxy NGC 3256. At first, from optical observations, I found many star forming blobs outside of nuclear regions, and these regions are categorized as starburst in terms of surface density of SFR and $M_{\rm H_2}$. However, it is difficult to investigate star formation activities in dusty regions by using optical observations. From ALMA sub-mm recombination line mapping, I found that there is a star forming region at the southern nucleus where optical recombination lines are undetected due to strong dust extinction ($A_{\rm V} \sim 18$). This means that $\sim 12\%$ of star formation activity is missed using optical lines as indicators of star formation activity in a dusty merging galaxy. Combining two observations, the global SFR in NGC 3256 is $\sim 41\ M_{\odot}\ {\rm yr}^{-1}$. The SFR in the northern and southern nuclei is 6.4 ± 0.9 and $5.0\pm0.7\ M_{\odot}\ {\rm yr}^{-1}$, respectively. This means that the contribution of extended star formation ($\sim 72\%$) is larger than dusty nuclear starbursts ($\sim 28\%$) in NGC 3256. For comprehensive approach, it is necessary to investigate more advanced merging galaxies (like merging ULIRGs) than NGC 3256. It is predicted that contribution of nuclear starburst is larger than disk-wide starburst in advanced late stage merger. My method using mm recombination line is ideal to investigate star formation activity in extremely dusty region in ULIRGs.

- **What kind of structure and properties do molecular outflows have?**

  I found clumpy structure at the AGN triggered outflow in NGC 3256. In ad-

dition, CO, HCN and HCO^+ observations showed the higher excitation and the larger dense gas fraction at the AGN triggered outflow than the nucleus. It is difficult to explain these results if we assume simple mass translation due to inflow and outflow. The complex physical mechanisms are necessary. For example, clumpy outflows are not basically included in the typical merger scenario, whereas such outflows are predicted in strong AGN feedback models. One possible scenario to produce clumpy structure in the outflow is a jet and ISM interaction. Such clumps in the outflows can possibly become the sites of future star formation ("positive feedback"), affecting the long-term evolution of the host galaxy. However, the expected SFR derived from total dense gas mass in the outflow is not as high as the SFR of host galaxy. The conclusion from this study is that while the degree of star formation is likely small, the existence of "positive feedback" is possible and it is not completely ruled out. As a next step, it is necessary to investigate how outflows affect the star formation activity not only for high-velocity gas but also for the gas in the disk. On the other hand, in the case of starburst triggered outflow in NGC 3256, clumps are not seen inside the outflow. In addition, observations showed the lower excitation and the smaller or similar dense gas fraction seen at the northern starburst triggered outflow than the northern nucleus. This suggests that the gas is simply expelled without any action from the nucleus, which can be explained by a standard process of "negative feedback".

The observational data presented in this thesis provides evidences of previously expected "disk-wide starbursts" and the new idea of "clumpy dense outflows" in merging galaxies, particularly in NGC 3256. However, this is just a case study only for one merging galaxy NGC 3256. The important next step is to expand our

observation from individual case studies to a statistically significant sample that includes a wide range of merger stages, star formation rates, and nuclear properties.

5.2 Future Works

Once ALMA started operation, merging galaxies have been observed with high resolution and sensitivity. Such observations enable us to precisely investigate physical, kinematic, and chemical properties of merging galaxies. However, most of the observational studies focus on each galaxy (i.e., chapter 3 and 4). It is necessary to find general characteristics by summarizing each case study. In order to improve the statistical studies by using single dish telescopes (i.e., chapter 2), it is possible to use ALMA archive. As a first step, I check how many galaxies have been observed up to now (October 2018). I cross match the IRAS Bright Galaxy Sample (Sanders et al. , 2003) and ALMA archive. I find that 197 of 629 sources have already observed by ALMA. In the case of VV catalog (Vorontsov-Velyaminov , 1959; Vorontsov-Velyaminov et al. , 2001), I find that 79 of 2014 sources have already observed by ALMA. Establishing ALMA merging galaxy catalog, I will investigate the general properties of the merging galaxies. The key questions are, for example, “How many merging galaxies have a massive molecular gas outflow?", “What is the difference between gas poor and rich mergers?", “Does a galaxy merger affect the chemical properties of the galaxy?", and etc.

One of the ultimate goals of astronomy is understanding the galaxy evolution during the history of the Universe, and redshift ~ 2 is the peak epoch of the star formation in the Universe. U/LIRGs are the principal galaxy population at this epoch, which produce $\sim 90\%$ of the IR luminosity density associated with star formation (e.g., Murphy et al. , 2011). Galaxy-galaxy mergers are the key mechanism to enhance the IR-luminosity in the Universe. It is necessary to directly compare

between galaxies at the peak epoch and local merging U/LIRGs. In terms of the molecular gas properties, a great number of observational studies are conducted towards the local U/LIRGs by using low-J CO lines (see chapter 2). On the other hand, for high redshift sources, it is difficult to observe low-J CO lines due to limited observable frequency. Therefore, molecular gas properties are investigated by high-J CO lines and/or atomic carbon lines (e.g., Bothwell et al. , 2016). Recently high frequency receivers have rapidly been developing; e.g., CO (4–3) to CO (7-6), CI(1–0), CI(2–1) from ALMA Band 8 to 10 receivers. I have just started ALMA ACA CI (2–1) and CO (4–3) observations towards 40 U/LIRGs (ALMA project ID: 2018.1.00994.S). I will directly compare the molecular gas properties between high redshift sources and local active galaxies.

In the future, I will continually observe merging galaxies with multi-wavelength and multi-line. I will give noteworthy phenomena during merger process which current theoretical models do not consider.

REFERENCES

Aalto S. Garcia-Burillo S. Muller S. Winters J. M. Gonzalez-Alfonso E. van der Werf P. Henkel C. Costagliola F. & Neri R. 2015, High resolution observations of HCN and HCO^+J = 3-2 in the disk and outflow of Mrk 231. Detection of vibrationally excited HCN in the warped nucleus, A&A, 574 A85

Aalto S. Garcia-Burillo S. Muller S. Winters J. M. van der Werf P. Henkel C. Costagliola F. & Neri R. 2012, Detection of HCN, HCO^+, and HNC in the Mrk 231 molecular outflow. Dense molecular gas in the AGN wind, A&A, 537 A44

Aalto S. Polatidis A. G. Hüttemeister S. & Curran S. J. 2002, CN and HNC line emission in IR luminous galaxies, A&A, 381 783–794

Anantharamaiah K. R. Viallefond F. Mohan N. R. Goss W. M. & Zhao J. H. 2000, Starburst in the Ultraluminous Galaxy Arp 220: Constraints from Observations of Radio Recombination Lines and Continuum, The Astrophysical Journal, 537 613–630

Armus L. Charmandaris V. Bernard-Salas J. Spoon H. W. W. Marshall J. A. Higdon S. J. U. Desai V. Teplitz H. I. Hao L. Devost D. Brandl B. R. Wu Y. Sloan G. C. Soifer B. T. Houck J. R. & Herter T. L. 2007, Observations of Ultraluminous Infrared Galaxies with the Infrared Spectrograph on the Spitzer Space Telescope. II. The IRAS Bright Galaxy Sample, ApJ, 656 148–167

Arp H. 1966, Atlas of peculiar galaxies

Arp H. C. & Madore B. 1987, A catalogue of southern peculiar galaxies and associations

Asplund M. Grevesse N. Sauval A. J. & Scott P. 2009, The Chemical Composition of the Sun, ARA&A, 47 481–522

Baldry I. K. Glazebrook K. Brinkmann J. Ivezić Ž. Lupton R. H. Nichol R. C. & Szalay A. S. 2004, Quantifying the Bimodal Color-Magnitude Distribution of Galaxies, ApJ, 600 681–694

Barcos-Muñoz L. Aalto S. Thompson T. A. Sakamoto K. Martín S. Leroy A. K. Privon G. C. Evans A. S. & Kepley A. 2018, Fast, Collimated Outflow in the Western Nucleus of Arp 220, ApJ, 853 L28

Barnes J. E. 2004, Shock-induced star formation in a model of the Mice, Monthly Notices of the Royal Astronomical Society, 350 798–808

Barnes J. E. & Hernquist L. 1992, Dynamics of Interacting Galaxies, Annual Review of Astronomy and Astrophysics, 30 705–742

Battisti A. J. & Heyer M. H. 2014, The Dense Gas Mass Fraction of Molecular Clouds in the Milky Way, ApJ, 780 173

Bendo G. J. Beswick R. J. D'Cruze M. J. Dickinson C. Fuller G. A. & Muxlow T. W. B. 2015, ALMA observations of 99 GHz free-free and H40α line emission from star formation in the centre of NGC 253, MNRAS, 450 L80–L84

Bendo G. J. Henkel C. D'Cruze M. J. Dickinson C. Fuller G. A. & Karim A. 2016, Free-free and H42α emission from the dusty starburst within NGC 4945 as observed by ALMA, MNRAS, 463 252–269

Bendo G. J. Miura R. E. Espada D. Nakanishi K. Beswick R. J. D'Cruze M. J. Dickinson C. & Fuller G. A. 2017, Tests of star formation metrics in the low-metallicity galaxy NGC 5253 using ALMA observations of H30α line emission, MNRAS, 472 1239–1252

Bigiel F. Leroy A. Walter F. Brinks E. de Blok W. J. G. Madore B. & Thornley M. D. 2008, THE STAR FORMATION LAW IN NEARBY GALAXIES ON

SUB-KPC SCALES, The Astronomical Journal, 136 2846–2871

Bigiel F. Leroy A. K. Blitz L. Bolatto A. D. da Cunha E. Rosolowsky E. Sandstrom K. & Usero A. 2015, DENSE GAS FRACTION AND STAR FORMATION EFFICIENCY VARIATIONS IN THE ANTENNAE GALAXIES, The Astrophysical Journal, 815 103

Bolatto A. D. Warren S. R. Leroy A. K. Walter F. Veilleux S. Ostriker E. C. Ott J. Zwaan M. Fisher D. B. Weiss A. & et al. 2013a, Suppression of star formation in the galaxy NGC 253 by a starburst-driven molecular wind, Nature, 499 450–453

Bolatto A. D. Wolfire M. & Leroy A. K. 2013b, The CO-to-H2Conversion Factor, Annual Review of Astronomy and Astrophysics, 51 207–268

Bothwell M. S. Maiolino R. Peng Y. Cicone C. Griffith H. & Wagg J. 2016, Molecular gas as the driver of fundamental galactic relations, MNRAS, 455 1156–1170

Bothwell M. S. Smail I. Chapman S. C. Genzel R. Ivison R. J. Tacconi L. J. Alaghband-Zadeh S. Bertoldi F. Blain A. W. Casey C. M. Cox P. Greve T. R. Lutz D. Neri R. Omont A. & Swinbank A. M. 2013, A survey of molecular gas in luminous sub-millimetre galaxies, MNRAS, 429 3047–3067

Bournaud F. 2011, Star formation in galaxy interactions and mergers, EAS Publications Series, 51 107–131

Bournaud F. Daddi E. Weiß A. Renaud F. Mastropietro C. & Teyssier R. 2015, Modeling CO emission from hydrodynamic simulations of nearby spirals, starbursting mergers, and high-redshift galaxies, A&A, 575 A56

Bridge C. R. Carlberg R. G. & Sullivan M. 2010, The CFHTLS-Deep Catalog of Interacting Galaxies. I. Merger Rate Evolution to z = 1.2, ApJ, 709 1067–1082

Burkhardt A. M. Dollhopf N. M. Corby J. F. Carroll P. B. Shingledecker C. N. Loomis R. A. Booth S. T. Blake G. A. Herbst E. Remijan A. J. & et al. 2016,

CSO AND CARMA OBSERVATIONS OF L1157. II. CHEMICAL COMPLEXITY IN THE SHOCKED OUTFLOW, The Astrophysical Journal, 827 21

Calzetti D. Star Formation Rate Indicators ed. J. Falcón-Barroso & J. H. Knapen, 419

Calzetti D. Armus L. Bohlin R. C. Kinney A. L. Koornneef J. & Storchi-Bergmann T. 2000, The Dust Content and Opacity of Actively Star-forming Galaxies, The Astrophysical Journal, 533 682–695

Carilli C. & Walter F. 2013, Cool Gas in High-Redshift Galaxies, Annual Review of Astronomy and Astrophysics, 51 105–161

Casey C. M. Narayanan D. & Cooray A. 2014, Dusty star-forming galaxies at high redshift, Phys. Rep., 541 45–161

Cheng C. Ibar E. Hughes T. M. Villanueva V. Leiton R. Orellana G. Muñoz Arancibia A. Lu N. Xu C. K. Willmer C. N. A. Huang J. Cao T. Yang C. Xue Y. Q. & Torstensson K. 2018, VALES - IV. Exploring the transition of star formation efficiencies between normal and starburst galaxies using APEX/SEPIA Band-5 and ALMA at low redshift, MNRAS, 475 248–256

Chisholm J. & Matsushita S. 2016, THE MOLECULAR BARYON CYCLE OF M82, The Astrophysical Journal, 830 72

Cicone C. Feruglio C. Maiolino R. Fiore F. Piconcelli E. Menci N. Aussel H. & Sturm E. 2012, The physics and the structure of the quasar-driven outflow in Mrk 231, A&A, 543 A99

Cicone C. Maiolino R. Sturm E. Graciá-Carpio J. Feruglio C. Neri R. Aalto S. Davies R. Fiore F. Fischer J. García-Burillo S. González-Alfonso E. Hailey-Dunsheath S. Piconcelli E. & Veilleux S. 2014, Massive molecular outflows and evidence for AGN feedback from CO observations, A&A, 562 A21

Condon J. J. Condon M. A. Gisler G. & Puschell J. J. 1982, Strong radio sources in bright spiral galaxies. II - Rapid star formation and galaxy-galaxy interactions, The Astrophysical Journal, 252 102

Condon J. J. & Dressel L. L. 1978, Compact radio sources in and near bright galaxies, The Astrophysical Journal, 221 456

Cortijo-Ferrero C. González Delgado R. M. Pérez E. Cid Fernandes R. García-Benito R. Di Matteo P. Sánchez S. F. de Amorim A. L. Lacerda E. A. D. López Fernández R. & Tadhunter C. 2017, The spatially resolved star formation history of mergers. A comparative study of the LIRGs IC 1623, NGC 6090, NGC 2623, and Mice, A&A, 607 A70

Costa T. Sijacki D. & Haehnelt M. G. 2015, Fast cold gas in hot AGN outflows, MNRAS, 448 L30–L34

Cox T. J. Jonsson P. Primack J. R. & Somerville R. S. 2006, Feedback in simulations of disc-galaxy major mergers, Monthly Notices of the Royal Astronomical Society, 373 1013–1038

Cox T. J. Jonsson P. Somerville R. S. Primack J. R. & Dekel A. 2008, The effect of galaxy mass ratio on merger-driven starbursts, MNRAS, 384 386–409

Cui J. Xia X.-Y. Deng Z.-G. Mao S. & Zou Z.-L. 2001, Statistical Properties of Ultraluminous IRAS Galaxies from an HST Imaging Survey, AJ, 122 63–82

Cullen H. Alexander P. Green D. A. Clemens M. & Sheth K. 2007, The unusual distribution of molecular gas and star formation in Arp 140, MNRAS, 374 1185–1197

Cutri R. M. Skrutskie M. F. van Dyk S. Beichman C. A. Carpenter J. M. Chester T. Cambresy L. Evans T. Fowler J. Gizis J. Howard E. Huchra J. Jarrett T. Kopan E. L. Kirkpatrick J. D. Light R. M. Marsh K. A. McCallon H. Schneider S. Stiening R. Sykes M. Weinberg M. Wheaton W. A. Wheelock S. & Zacarias N.

2003, VizieR Online Data Catalog: 2MASS All-Sky Catalog of Point Sources (Cutri+ 2003), VizieR Online Data Catalog, 2246

Daddi E. Bournaud F. Walter F. Dannerbauer H. Carilli C. L. Dickinson M. Elbaz D. Morrison G. E. Riechers D. Onodera M. Salmi F. Krips M. & Stern D. 2010, Very High Gas Fractions and Extended Gas Reservoirs in z = 1.5 Disk Galaxies, ApJ, 713 686–707

Dasyra K. M. Bostrom A. C. Combes F. & Vlahakis N. 2015, A RADIO JET DRIVES A MOLECULAR AND ATOMIC GAS OUTFLOW IN MULTIPLE REGIONS WITHIN ONE SQUARE KILOPARSEC OF THE NUCLEUS OF THE NEARBY GALAXY IC5063, The Astrophysical Journal, 815 34

Dasyra K. M. Combes F. Oosterloo T. Oonk J. B. R. Morganti R. Salomé P. & Vlahakis N. 2016, ALMA reveals optically thin, highly excited CO gas in the jet-driven winds of the galaxy IC 5063, A&A, 595 L7

Debuhr J. Quataert E. & Ma C.-P. 2012, Galaxy-scale outflows driven by active galactic nuclei, MNRAS, 420 2221–2231

Di Matteo T. Springel V. & Hernquist L. 2005, Energy input from quasars regulates the growth and activity of black holes and their host galaxies, Nature, 433 604–607

Donovan Meyer J. Koda J. Momose R. Mooney T. Egusa F. Carty M. Kennicutt R. Kuno N. Rebolledo D. Sawada T. Scoville N. & Wong T. 2013, Resolved Giant Molecular Clouds in Nearby Spiral Galaxies: Insights from the CANON CO (1-0) Survey, ApJ, 772 107

Downes D. & Solomon P. M. 1998, Rotating Nuclear Rings and Extreme Starbursts in Ultraluminous Galaxies, ApJ, 507 615–654

Dugan Z. Bryan S. Gaibler V. Silk J. & Haas M. 2014, STELLAR SIGNATURES OF AGN-JET-TRIGGERED STAR FORMATION, The Astrophysical Journal,

796 113

Elitzur M. 1983, Shock formation of HCO/+/, ApJ, 267 174–178

Ellison S. L. Patton D. R. Simard L. & McConnachie A. W. 2008, Galaxy Pairs in the Sloan Digital Sky Survey. I. Star Formation, Active Galactic Nucleus Fraction, and the Mass-Metallicity Relation, AJ, 135 1877–1899

Elmegreen B. G. & Elmegreen D. M. 2005, Stellar Populations in 10 Clump-Cluster Galaxies of the Hubble Ultra Deep Field, The Astrophysical Journal, 627 632–646

Emonts B. H. C. Piqueras-López J. Colina L. Arribas S. Villar-Martín M. Pereira-Santaella M. Garcia-Burillo S. & Alonso-Herrero A. 2014, Outflow of hot and cold molecular gas from the obscured secondary nucleus of NGC 3256: closing in on feedback physics, A&A, 572 A40

English J. Norris R. P. Freeman K. C. & Booth R. S. 2003, NGC 3256: Kinematic Anatomy of a Merger, AJ, 125 1134–1149

Espada D. Komugi S. Muller E. Nakanishi K. Saito M. Tatematsu K. Iguchi S. Hasegawa T. Mizuno N. Iono D. Matsushita S. Trejo A. Chapillon E. Takahashi S. Su Y. N. Kawamura A. Akiyama E. Hiramatsu M. Nagai H. Miura R. E. Kurono Y. Sawada T. Higuchi A. E. Tachihara K. Saigo K. & Kamazaki T. 2012, Giant Molecular Clouds and Star Formation in the Tidal Molecular Arm of NGC 4039, ApJ, 760 L25

Ezawa H. Kohno K. Kawabe R. Yamamoto S. Inoue H. Iwashita H. Matsuo H. Okuda T. Oshima T. Sakai T. Tanaka K. Yamaguchi N. Wilson G. W. Yun M. S. Aretxaga I. Hughes D. Austermann J. Perera T. A. Scott K. S. Bronfman L. & Cortes J. R. 2008, in Society of Photo-Optical Instrumentation Engineers (SPIE) Conference Series, Vol. 7012 Ground-based and Airborne Telescopes II, 701208

Fabian A. C. Vasudevan R. V. Mushotzky R. F. Winter L. M. & Reynolds C. S. 2009, Radiation pressure and absorption in AGN: results from a complete unbiased sample fromSwift, Monthly Notices of the Royal Astronomical Society: Letters, 394 L89–L92

Falstad N. González-Alfonso E. Aalto S. van der Werf P. P. Fischer J. Veilleux S. Meléndez M. Farrah D. & Smith H. A. 2015, Herschel spectroscopic observations of the compact obscured nucleus in Zw 049.057, A&A, 580 A52

Ferrara A. & Scannapieco E. 2016, On the Formation of Molecular Clumps in QSO Outflows, ApJ, 833 46

Feruglio C. Fiore F. Carniani S. Piconcelli E. Zappacosta L. Bongiorno A. Cicone C. Maiolino R. Marconi A. Menci N. Puccetti S. & Veilleux S. 2015, The multi-phase winds of Markarian 231: from the hot, nuclear, ultra-fast wind to the galaxy-scale, molecular outflow, A&A, 583 A99

Feruglio C. Fiore F. Maiolino R. Piconcelli E. Aussel H. Elbaz D. Le Floc'h E. Sturm E. Davies R. & Cicone C. 2013, <ASTROBJ>NGC 6240</ASTROBJ>: extended CO structures and their association with shocked gas, A&A, 549 A51

Feruglio C. Maiolino R. Piconcelli E. Menci N. Aussel H. Lamastra A. & Fiore F. 2010, Quasar feedback revealed by giant molecular outflows, A&A, 518 L155

Fiore F. Feruglio C. Shankar F. Bischetti M. Bongiorno A. Brusa M. Carniani S. Cicone C. Duras F. Lamastra A. Mainieri V. Marconi A. Menci N. Maiolino R. Piconcelli E. Vietri G. & Zappacosta L. 2017, AGN wind scaling relations and the co-evolution of black holes and galaxies, A&A, 601 A143

Flower D. R. & Pineau des Forêts G. 2010, Excitation and emission of H, CO and HO molecules in interstellar shock waves, Monthly Notices of the Royal Astronomical Society no–no

Gaibler V. Khochfar S. Krause M. & Silk J. 2012, Jet-induced star formation in

gas-rich galaxies, Monthly Notices of the Royal Astronomical Society, 425 438–449

Gao Y. & Solomon P. M. 2004, The Star Formation Rate and Dense Molecular Gas in Galaxies, The Astrophysical Journal, 606 271–290

García-Burillo S. Combes F. Usero A. Aalto S. Colina L. Alonso-Herrero A. Hunt L. K. Arribas S. Costagliola F. Labiano A. Neri R. Pereira-Santaella M. Tacconi L. J. & van der Werf P. P. 2015, High-resolution imaging of the molecular outflows in two mergers: <ASTROBJ>IRAS 17208-0014</ASTROBJ> and <ASTROBJ>NGC 1614</ASTROBJ>, A&A, 580 A35

Genzel R. Tacconi L. J. Gracia-Carpio J. Sternberg A. Cooper M. C. Shapiro K. Bolatto A. Bouché N. Bournaud F. Burkert A. Combes F. Comerford J. Cox P. Davis M. Schreiber N. M. F. Garcia-Burillo S. Lutz D. Naab T. Neri R. Omont A. Shapley A. & Weiner B. 2010, A study of the gas-star formation relation over cosmic time, MNRAS, 407 2091–2108

Gil de Paz A. Boissier S. Madore B. F. Seibert M. Joe Y. H. Boselli A. Wyder T. K. Thilker D. Bianchi L. Rey S.-C. Rich R. M. Barlow T. A. Conrow T. Forster K. Friedman P. G. Martin D. C. Morrissey P. Neff S. G. Schiminovich D. Small T. Donas J. Heckman T. M. Lee Y.-W. Milliard B. Szalay A. S. & Yi S. 2007, The GALEX Ultraviolet Atlas of Nearby Galaxies, ApJS, 173 185–255

Goldsmith K. J. A. & Pittard J. M. 2017, A comparison of shock-cloud and wind-cloud interactions: the longer survival of clouds in winds, MNRAS, 470 2427–2438

González-Alfonso E. Fischer J. Graciá-Carpio J. Falstad N. Sturm E. Meléndez M. Spoon H. W. W. Verma A. Davies R. I. Lutz D. Aalto S. Polisensky E. Poglitsch A. Veilleux S. & Contursi A. 2014, The Mrk 231 molecular outflow as seen in OH, A&A, 561 A27

Greve T. R. Leonidaki I. Xilouris E. M. Weiß A. Zhang Z.-Y. van der Werf P. Aalto S. Armus L. Díaz-Santos T. Evans A. S. Fischer J. Gao Y. González-Alfonso E. Harris A. Henkel C. Meijerink R. Naylor D. A. Smith H. A. Spaans M. Stacey G. J. Veilleux S. & Walter F. 2014, Star Formation Relations and CO Spectral Line Energy Distributions across the J-ladder and Redshift, ApJ, 794 142

Harada N. Riquelme D. Viti S. Jiménez-Serra I. Requena-Torres M. A. Menten K. M. Martín S. Aladro R. Martin-Pintado J. & Hochgürtel S. 2015, Chemical features in the circumnuclear disk of the Galactic center, A&A, 584 A102

Harada N. Sakamoto K. Martín S. Aalto S. Aladro R. & Sliwa K. 2018, ALMA Astrochemical Observations of the Infrared-luminous Merger NGC 3256, The Astrophysical Journal, 855 49

Hayward C. C. Lanz L. Ashby M. L. N. Fazio G. Hernquist L. Martínez-Galarza J. R. Noeske K. Smith H. A. Wuyts S. & Zezas A. 2014, The total infrared luminosity may significantly overestimate the star formation rate of quenching and recently quenched galaxies, Monthly Notices of the Royal Astronomical Society, 445 1598–1604

Heckman T. M. 2001, in Astronomical Society of the Pacific Conference Series, Vol. 240 Gas and Galaxy Evolution ed. J. E. Hibbard M. Rupen & J. H. van Gorkom, 345

Heckman T. M. Armus L. & Miley G. K. 1990, On the nature and implications of starburst-driven galactic superwinds, The Astrophysical Journal Supplement Series, 74 833

Heckman T. M. Lehnert M. D. Strickland D. K. & Armus L. 2000, Absorption-Line Probes of Gas and Dust in Galactic Superwinds, ApJS, 129 493–516

Helfer T. T. Thornley M. D. Regan M. W. Wong T. Sheth K. Vogel S. N. Blitz L. & Bock D. C. 2003, The BIMA Survey of Nearby Galaxies (BIMA SONG). II.

The CO Data, The Astrophysical Journal Supplement Series, 145 259–327

Henkel C. Asiri H. Ao Y. Aalto S. Danielson A. L. R. Papadopoulos P. P. García-Burillo S. Aladro R. Impellizzeri C. M. V. Mauersberger R. Martín S. & Harada N. 2014, Carbon and oxygen isotope ratios in starburst galaxies: New data from NGC 253 and Mrk 231 and their implications, A&A, 565 A3

Herrera-Camus R. Sturm E. Graciá-Carpio J. Lutz D. Contursi A. Veilleux S. Fischer J. González-Alfonso E. Poglitsch A. Tacconi L. Genzel R. Maiolino R. Sternberg A. Davies R. & Verma A. 2018, SHINING, A Survey of Far-infrared Lines in Nearby Galaxies. II. Line-deficit Models, AGN Impact, [C II]-SFR Scaling Relations, and Mass-Metallicity Relation in (U)LIRGs, ApJ, 861 95

Holmberg E. 1941, On the Clustering Tendencies among the Nebulae. II. a Study of Encounters Between Laboratory Models of Stellar Systems by a New Integration Procedure., ApJ, 94 385

Hopkins P. F. Hernquist L. Cox T. J. Di Matteo T. Robertson B. & Springel V. 2006, A Unified, Merger-driven Model of the Origin of Starbursts, Quasars, the Cosmic X-Ray Background, Supermassive Black Holes, and Galaxy Spheroids, ApJS, 163 1–49

Hopkins P. F. Hernquist L. Cox T. J. & Kereš D. 2008, A Cosmological Framework for the Co-Evolution of Quasars, Supermassive Black Holes, and Elliptical Galaxies. I. Galaxy Mergers and Quasar Activity, ApJS, 175 356–389

Hubble E. P. 1926, Extragalactic nebulae., The Astrophysical Journal, 64 321

Hummel E. Beck R. & Dettmar R.-J. 1991, An Effelsberg/VLA radio continuum survey of an optically selected sample of edge-on spiral galaxies, A&AS, 87 309–317

Ichikawa K. Imanishi M. Ueda Y. Nakagawa T. Shirahata M. Kaneda H. & Oyabu S. 2014, AKARI IRC 2.5-5 μm Spectroscopy of Infrared Galaxies over a Wide

Luminosity Range, ApJ, 794 139

Iglesias E. R. & Silk J. 1978, Nonequilibrium chemistry in shocked molecular clouds, ApJ, 226 851–857

Iguchi S. & Okuda T. 2008, The FFX Correlator, PASJ, 60 857–869

Inoue H. Muraoka K. Sakai T. Endo A. Kohno K. Asayama S. Noguchi T. & Ogawa H. 2008, in Ninteenth International Symposium on Space Terahertz Technology ed. W. Wild, 281

Iono D. Saito T. Yun M. S. Kawabe R. Espada D. Hagiwara Y. Imanishi M. Izumi T. Kohno K. Motohara K. & et al. 2013, Active Galactic Nucleus and Extended Starbursts in a Midstage Merger VV 114, Publications of the Astronomical Society of Japan, 65 L7

Iono D. Wilson C. D. Yun M. S. Baker A. J. Petitpas G. R. Peck A. B. Krips M. Cox T. J. Matsushita S. Mihos J. C. & Pihlstrom Y. 2009, Luminous Infrared Galaxies with the Submillimeter Array. II. Comparing the CO (3-2) Sizes and Luminosities of Local and High-Redshift Luminous Infrared Galaxies, ApJ, 695 1537–1549

Iono D. Yun M. S. & Mihos J. C. 2004, Radial Gas Flows in Colliding Galaxies: Connecting Simulations and Observations, The Astrophysical Journal, 616 199–220

Izumi T. Nakanishi K. Imanishi M. & Kohno K. 2016, ALMA observations of the submillimetre hydrogen recombination line from the type 2 active nucleus of NGC 1068, MNRAS, 459 3629–3634

Jarrett T. H. Cohen M. Masci F. Wright E. Stern D. Benford D. Blain A. Carey S. Cutri R. M. Eisenhardt P. Lonsdale C. Mainzer A. Marsh K. Padgett D. Petty S. Ressler M. Skrutskie M. Stanford S. Surace J. Tsai C. W. Wheelock S. & Yan D. L. 2011, The Spitzer-WISE Survey of the Ecliptic Poles, ApJ, 735 112

Kamenetzky J. Glenn J. Rangwala N. Maloney P. Bradford M. Wilson C. D. Bendo G. J. Baes M. Boselli A. Cooray A. Isaak K. G. Lebouteiller V. Madden S. Panuzzo P. Schirm M. R. P. Spinoglio L. & Wu R. 2012, Herschel-SPIRE Imaging Spectroscopy of Molecular Gas in M82, ApJ, 753 70

Keel W. C. Kennicutt Jr. R. C. Hummel E. & van der Hulst J. M. 1985, The effects of interactions on spiral galaxies. I - Nuclear activity and star formation, AJ, 90 708–730

Kennicutt R. C. 1998, STAR FORMATION IN GALAXIES ALONG THE HUBBLE SEQUENCE, Annual Review of Astronomy and Astrophysics, 36 189–231

Kennicutt R. C. & Evans N. J. 2012, Star Formation in the Milky Way and Nearby Galaxies, ARA&A, 50 531–608

Kennicutt Jr. R. C. 1983, The rate of star formation in normal disk galaxies, ApJ, 272 54–67

Kennicutt Jr. R. C. Armus L. Bendo G. Calzetti D. Dale D. A. Draine B. T. Engelbracht C. W. Gordon K. D. Grauer A. D. Helou G. Hollenbach D. J. Jarrett T. H. Kewley L. J. Leitherer C. Li A. Malhotra S. Regan M. W. Rieke G. H. Rieke M. J. Roussel H. Smith J.-D. T. Thornley M. D. & Walter F. 2003, SINGS: The SIRTF Nearby Galaxies Survey, PASP, 115 928–952

Kewley L. J. Geller M. J. & Barton E. J. 2006, Metallicity and Nuclear Star Formation in Nearby Galaxy Pairs: Evidence for Tidally Induced Gas Flows, AJ, 131 2004–2017

Komugi S. Kohno K. Tosaki T. Nakanishi H. Onodera S. Egusa F. & Sofue Y. 2007, ASTE Observations of Nearby Galaxies: A Tight Correlation between CO J=3–2 Emission and Hα, PASJ, 59 55–60

König S. Martín S. Muller S. Cernicharo J. Sakamoto K. Zschaechner L. K.

Humphreys E. M. L. Mroczkowski T. Krips M. Galametz M. Aalto S. Vlemmings W. H. T. Ott J. Meier D. S. Fuente A. García-Burillo S. & Neri R. 2017, Subarcsecond imaging of the water emission in Arp 220, A&A, 602 A42

Kreckel K. Armus L. Groves B. Lyubenova M. Díaz-Santos T. Schinnerer E. Appleton P. Croxall K. V. Dale D. A. Hunt L. K. & et al. 2014, A FAR-IR VIEW OF THE STARBURST-DRIVEN SUPERWIND IN NGC 2146, The Astrophysical Journal, 790 26

Krips M. Martín S. Eckart A. Neri R. García-Burillo S. Matsushita S. Peck A. Stoklasová I. Petitpas G. Usero A. Combes F. Schinnerer E. Humphreys E. & Baker A. J. 2011, Submillimeter Array/Plateau de Bure Interferometer Multiple Line Observations of the Nearby Seyfert 2 Galaxy NGC 1068: Shock-related Gas Kinematics and Heating in the Central 100 pc?, ApJ, 736 37

Krips M. Martín S. Sakamoto K. Aalto S. Bisbas T. G. Bolatto A. D. Downes D. Eckart A. Feruglio C. García-Burillo S. Geach J. Greve T. R. König S. Matsushita S. Neri R. Offner S. Peck A. B. Viti S. & Wagg J. 2016, ACA [CI] observations of the starburst galaxy NGC 253, A&A, 592 L3

Kroupa P. 2002, The Initial Mass Function of Stars: Evidence for Uniformity in Variable Systems, Science, 295 82–91

Krumholz M. R. & McKee C. F. 2005, A General Theory of Turbulence-regulated Star Formation, from Spirals to Ultraluminous Infrared Galaxies, The Astrophysical Journal, 630 250–268

Krumholz M. R. & Thompson T. A. 2007, The Relationship between Molecular Gas Tracers and Kennicutt-Schmidt Laws, ApJ, 669 289–298

Larson R. B. 1981, Turbulence and star formation in molecular clouds, MNRAS, 194 809–826

Larson R. B. & Tinsley B. M. 1978, Star formation rates in normal and peculiar

galaxies, The Astrophysical Journal, 219 46

Leech J. Isaak K. G. Papadopoulos P. P. Gao Y. & Davis G. R. 2010, A CO(3-2) survey of a merging sequence of luminous infrared galaxies, MNRAS, 406 1364–1378

Leroy A. K. Walter F. Brinks E. Bigiel F. de Blok W. J. G. Madore B. & Thornley M. D. 2008, THE STAR FORMATION EFFICIENCY IN NEARBY GALAXIES: MEASURING WHERE GAS FORMS STARS EFFECTIVELY, The Astronomical Journal, 136 2782–2845

Li Y. Mac Low M.-M. & Klessen R. S. 2005, Star Formation in Isolated Disk Galaxies. I. Models and Characteristics of Nonlinear Gravitational Collapse, ApJ, 626 823–843

Lin M.-Y. Davies R. I. Burtscher L. Contursi A. Genzel R. González-Alfonso E. Graciá-Carpio J. Janssen A. Lutz D. Orban de Xivry G. Rosario D. Schnorr-Müller A. Sternberg A. Sturm E. & Tacconi L. 2016, Thick discs, and an outflow, of dense gas in the nuclei of nearby Seyfert galaxies, MNRAS, 458 1375–1392

Lindberg J. E. Aalto S. Muller S. Martí-Vidal I. Falstad N. Costagliola F. Henkel C. van der Werf P. García-Burillo S. & González-Alfonso E. 2016, Evidence for a chemically differentiated outflow in Mrk 231, A&A, 587 A15

Lípari S. Díaz R. Taniguchi Y. Terlevich R. Dottori H. & Carranza G. 2000, Luminous Infrared Galaxies. III. Multiple Merger, Extended Massive Star Formation, Galactic Wind, and Nuclear Inflow in NGC 3256, The Astronomical Journal, 120 645–669

Lira P. Gonzalez-Corvalan V. Ward M. & Hoyer S. 2008, An infrared study of the double nucleus in NGC3256, MNRAS, 384 316–322

Lynds C. R. & Sandage A. R. 1963, Evidence for an Explosion in the Center of the

Galaxy M82., The Astrophysical Journal, 137 1005

Magorrian J. Tremaine S. Richstone D. Bender R. Bower G. Dressler A. Faber S. M. Gebhardt K. Green R. Grillmair C. Kormendy J. & Lauer T. 1998, The Demography of Massive Dark Objects in Galaxy Centers, AJ, 115 2285–2305

Maiolino R. Russell H. R. Fabian A. C. Carniani S. Gallagher R. Cazzoli S. Arribas S. Belfiore F. Bellocchi E. Colina L. Cresci G. Ishibashi W. Marconi A. Mannucci F. Oliva E. & Sturm E. 2017, Star formation inside a galactic outflow, Nature, 544 202–206

Mao R.-Q. Schulz A. Henkel C. Mauersberger R. Muders D. & Dinh-V-Trung. 2010, An Extragalactic ^{12}CO J = 3-2 Survey with the Heinrich Hertz Telescope, ApJ, 724 1336–1356

Marconi A. Moorwood A. F. M. Origlia L. & Oliva E. 1994, A prominent ionization cone and starburst ring in the nearby Circinus galaxy., The Messenger, 78 20–24

Mateos S. Alonso-Herrero A. Carrera F. J. Blain A. Watson M. G. Barcons X. Braito V. Severgnini P. Donley J. L. & Stern D. 2012, Using the Bright Ultrahard XMM-Newton survey to define an IR selection of luminous AGN based on WISE colours, MNRAS, 426 3271–3281

Matsushita S. Muller S. & Lim J. 2007, Jet-disturbed molecular gas near the Seyfert 2 nucleus in M 51, A&A, 468 L49–L52

Matsushita S. Trung D.-V. Boone F. Krips M. Lim J. & Muller S. 2015, Resolving the Bright HCN(1-0) Emission toward the Seyfert 2 Nucleus of M51: Shock Enhancement by Radio Jets and Weak Masing by Infrared Pumping?, ApJ, 799 26

McMullin J. P. Waters B. Schiebel D. Young W. & Golap K. 2007, in Astronomical Society of the Pacific Conference Series, Vol. 376 Astronomical Data Analysis

Software and Systems XVI ed. R. A. Shaw F. Hill & D. J. Bell, 127

McNamara B. R. & Nulsen P. E. J. 2007, Heating Hot Atmospheres with Active Galactic Nuclei, ARA&A, 45 117–175

Melnick J. & Mirabel I. F. 1990, NTT images of ultraluminous infrared galaxies, A&A, 231 L19–L22

Michiyama T. Iono D. Nakanishi K. Ueda J. Saito T. Ando M. Kaneko H. Yamashita T. Matsuda Y. Hatsukade B. Kikuchi K. Komugi S. & Muto T. 2016, Investigating the relation between CO (3-2) and far-infrared luminosities for nearby merging galaxies using ASTE, PASJ, 68 96

Michiyama T. Iono D. Sliwa K. Bolatto A. Nakanishi K. Ueda J. Saito T. Ando M. Yamashita T. & Yun M. 2018, ALMA observations of HCN and HCO+ outflows in the merging galaxy NGC 3256, ArXiv e-prints

Mihos C. 1999, Dynamics of Mergers, Ap&SS, 266 195–205

Mitchell G. F. 1983, The synthesis of hydrocarbon molecules in a shocked interstellar cloud, MNRAS, 205 765–772

Mo H. Van den Bosch F. & White S. 2010, Galaxy formation and evolution (Cambridge University Press)

Mo H. van den Bosch F. C. & White S. 2010, Galaxy Formation and Evolution

Morganti R. Frieswijk W. Oonk R. J. B. Oosterloo T. & Tadhunter C. 2013, Tracing the extreme interplay between radio jets and the ISM in IC 5063, A&A, 552 L4

Morganti R. Oosterloo T. Oonk J. B. R. Frieswijk W. & Tadhunter C. 2015, The fast molecular outflow in the Seyfert galaxy IC 5063 as seen by ALMA, A&A, 580 A1

Muraoka K. Kohno K. Tosaki T. Kuno N. Nakanishi K. Sorai K. Okuda T. Sakamoto S. Endo A. Hatsukade B. Kamegai K. Tanaka K. Cortes J. Ezawa H. Yamaguchi

N. Sakai T. & Kawabe R. 2007, ASTE CO (3-2) Observations of the Barred Spiral Galaxy M 83: I. Correlation between CO (3-2)/ CO (1-0) Ratios and Star Formation Efficiencies, PASJ, 59 43–54

Muraoka K. Takeda M. Yanagitani K. Kaneko H. Nakanishi K. Kuno N. Sorai K. Tosaki T. & Kohno K. 2016, CO(J = 3-2) on-the-fly mapping of the nearby spiral galaxies NGC 628 and NGC 7793: Spatially resolved CO(J = 3-2) star-formation law, PASJ, 68 18

Murphy E. J. Condon J. J. Schinnerer E. Kennicutt R. C. Calzetti D. Armus L. Helou G. Turner J. L. Aniano G. Beirão P. & et al. 2011, CALIBRATING EXTINCTION-FREE STAR FORMATION RATE DIAGNOSTICS WITH 33 GHz FREE-FREE EMISSION IN NGC 6946, The Astrophysical Journal, 737 67

Murphy Jr. T. W. Soifer B. T. Matthews K. & Armus L. 2001, Age Dating Ultraluminous Infrared Galaxies along the Merger Sequence, ApJ, 559 201–224

Narayanan D. Cox T. J. Kelly B. Davé R. Hernquist L. Di Matteo T. Hopkins P. F. Kulesa C. Robertson B. & Walker C. K. 2008, The Role of Galactic Winds on Molecular Gas Emission from Galaxy Mergers, ApJS, 176 331–354

Narayanan D. Cox T. J. Shirley Y. Davé R. Hernquist L. & Walker C. K. 2008, Molecular Star Formation Rate Indicators in Galaxies, The Astrophysical Journal, 684 996–1008

Narayanan D. Krumholz M. R. Ostriker E. C. & Hernquist L. 2012, A general model for the CO-H2 conversion factor in galaxies with applications to the star formation law, Monthly Notices of the Royal Astronomical Society, 421 3127–3146

Neff S. G. Ulvestad J. S. & Campion S. D. 2003, Radio Emission Associated with Ultraluminous X-Ray Sources in the Galaxy Merger NGC 3256, The Astro-

physical Journal, 599 1043–1048

Neugebauer G. Habing H. J. van Duinen R. Aumann H. H. Baud B. Beichman C. A. Beintema D. A. Boggess N. Clegg P. E. de Jong T. & et al. 1984, The Infrared Astronomical Satellite (IRAS) mission, The Astrophysical Journal, 278 L1

Newton R. D. A. & Kay S. T. 2013, A study of AGN and supernova feedback in simulations of isolated and merging disc galaxies, MNRAS, 434 3606–3627

Ohyama Y. Terashima Y. & Sakamoto K. 2015, INFRARED AND X-RAY EVIDENCE OF AN AGN IN THE NGC 3256 SOUTHERN NUCLEUS, The Astrophysical Journal, 805 162

Okuda T. & Iguchi S. 2008, Performance Measurements of 8-Gsps 1-bit ADCs Developed for Wideband Radio Astronomical Observations, PASJ, 60 315–325

Omont A. 2007, Molecules in galaxies, Reports on Progress in Physics, 70 1099–1176

Onodera S. Kuno N. Tosaki T. Kohno K. Nakanishi K. Sawada T. Muraoka K. Komugi S. Miura R. Kaneko H. Hirota A. & Kawabe R. 2010, Breakdown of Kennicutt-Schmidt Law at Giant Molecular Cloud Scales in M33, ApJ, 722 L127–L131

Pagel B. E. J. 1979, in Astrophysics and Space Science Library, Vol. 75 Stars and star systems ed. B. E. Westerlund, 17–31

Pan H.-A. Lin L. Hsieh B.-C. Xiao T. Gao Y. Ellison S. L. Scudder J. M. Barrera-Ballesteros J. Yuan F. Saintonge A. Wilson C. D. Hwang H. S. De Looze I. Gao Y. Ho L. C. Brinks E. Mok A. Brown T. Davis T. A. Williams T. G. Chung A. Parsons H. Bureau M. Sargent M. T. Chung E. J. Kim E. Liu T. Michałowski M. J. & Tosaki T. 2018, The Effect of Galaxy Interactions on Molecular Gas Properties, ApJ, 868 132

Papadopoulos P. P. 2007, HCN versus HCO^+ as Dense Molecular Gas Mass Tracers

in Luminous Infrared Galaxies, ApJ, 656 792–797

Papadopoulos P. P. van der Werf P. P. Xilouris E. M. Isaak K. G. Gao Y. & Mühle S. 2012, The molecular gas in luminous infrared galaxies - I. CO lines, extreme physical conditions and their drivers, MNRAS, 426 2601–2629

Park J. Smith R. & Yi S. K. 2017, Star Formation of Merging Disk Galaxies with AGN Feedback Effects, ApJ, 845 128

Pereira-Santaella M. Colina L. García-Burillo S. Combes F. Emonts B. Aalto S. Alonso-Herrero A. Arribas S. Henkel C. Labiano A. Muller S. Piqueras López J. Rigopoulou D. & van der Werf P. 2018, Spatially resolved cold molecular outflows in ULIRGs, A&A, 616 A171

Pettitt A. R. Egusa F. Dobbs C. L. Tasker E. J. Fujimoto Y. & Habe A. 2018, The changing GMC population in galaxy interactions, MNRAS, 480 3356–3375

Pettitt A. R. Tasker E. J. & Wadsley J. W. 2016, Gas and stellar spiral structures in tidally perturbed disc galaxies, MNRAS, 458 3990–4007

Pettitt A. R. Tasker E. J. Wadsley J. W. Keller B. W. & Benincasa S. M. 2017, Star formation and ISM morphology in tidally induced spiral structures, MNRAS, 468 4189–4204

Pettitt A. R. & Wadsley J. W. 2018, Bars and spirals in tidal interactions with an ensemble of galaxy mass models, MNRAS, 474 5645–5671

Piqueras López J. Colina L. Arribas S. & Alonso-Herrero A. 2013, VLT-SINFONI integral field spectroscopy of low-z luminous and ultraluminous infrared galaxies. II. 2D extinction structure and distance effects, A&A, 553 A85

Piqueras López J. Colina L. Arribas S. Alonso-Herrero A. & Bedregal A. G. 2012, VLT-SINFONI integral field spectroscopy of low-z luminous and ultraluminous infrared galaxies. I. Atlas of the 2D gas structure, A&A, 546 A64

Piqueras López J. Colina L. Arribas S. Pereira-Santaella M. & Alonso-Herrero

A. 2016, VizieR Online Data Catalog: Ionized gas maps of local U/LIRGs (Piqueras-Lopez+, 2016), VizieR Online Data Catalog, 359

Powell L. C. Bournaud F. Chapon D. & Teyssier R. 2013, Beyond the nuclear starburst? Clustered star formation in major mergers, Monthly Notices of the Royal Astronomical Society, 434 1028–1042

Querejeta M. Schinnerer E. García-Burillo S. Bigiel F. Blanc G. A. Colombo D. Hughes A. Kreckel K. Leroy A. K. Meidt S. E. Meier D. S. Pety J. & Sliwa K. 2016, AGN feedback in the nucleus of M 51, A&A, 593 A118

Read A. M. Ponman T. J. & Strickland D. K. 1997, ROSAT PSPC observations of nearby spiral galaxies – I. The data, Monthly Notices of the Royal Astronomical Society, 286 626–668

Renaud F. Bournaud F. Daddi E. & Weiß A. 2018, Three regimes of CO emission in galaxy mergers, arXiv e-prints

Rich J. A. Kewley L. J. & Dopita M. A. 2011, Galaxy-wide Shocks in Late-merger Stage Luminous Infrared Galaxies, ApJ, 734 87

Richings A. J. & Faucher-Giguère C.-A. 2018, The origin of fast molecular outflows in quasars: molecule formation in AGN-driven galactic winds, MNRAS, 474 3673–3699

Rieke G. H. & Low F. J. 1972, Infrared Photometry of Extragalactic Sources, The Astrophysical Journal, 176 L95

Rupke D. S. N. Veilleux S. & Baker A. J. 2008, The Oxygen Abundances of Luminous and Ultraluminous Infrared Galaxies, ApJ, 674 172–193

Saito T. Iono D. Ueda J. Espada D. Sliwa K. Nakanishi K. Lu N. Xu C. K. Michiyama T. Kaneko H. Yamashita T. Ando M. Yun M. S. Motohara K. & Kawabe R. 2018, Imaging the molecular outflows of the prototypical ULIRG NGC 6240 with ALMA, MNRAS, 475 L52–L56

Saito T. Iono D. Xu C. K. Ueda J. Nakanishi K. Yun M. S. Kaneko H. Yamashita T. Lee M. Espada D. Motohara K. & Kawabe R. 2016, Spatially resolved radio-to-far-infrared SED of the luminous merger remnant NGC 1614 with ALMA and VLA, PASJ, 68 20

Saito T. Iono D. Yun M. S. Ueda J. Nakanishi K. Sugai H. Espada D. Imanishi M. Motohara K. Hagiwara Y. & et al. 2015, ALMA MULTI-LINE OBSERVATIONS OF THE IR-BRIGHT MERGER VV 114, The Astrophysical Journal, 803 60

Sakamoto K. Aalto S. Combes F. Evans A. & Peck A. 2014, AN INFRARED-LUMINOUS MERGER WITH TWO BIPOLAR MOLECULAR OUTFLOWS: ALMA AND SMA OBSERVATIONS OF NGC 3256, The Astrophysical Journal, 797 90

Sakamoto K. Aalto S. Wilner D. J. Black J. H. Conway J. E. Costagliola F. Peck A. B. Spaans M. Wang J. & Wiedner M. C. 2009, P Cygni Profiles of Molecular Lines Toward Arp 220 Nuclei, ApJ, 700 L104–L108

Sakamoto K. Ho P. T. P. Iono D. Keto E. R. Mao R. Matsushita S. Peck A. B. Wiedner M. C. Wilner D. J. & Zhao J. 2006, Molecular Superbubbles in the Starburst Galaxy NGC 253, The Astrophysical Journal, 636 685–697

Salak D. Nakai N. Hatakeyama T. & Miyamoto Y. 2016, Gas Dynamics and Outflow in the Barred Starburst Galaxy NGC 1808 Revealed with ALMA, ApJ, 823 68

Salas P. Galaz G. Salter D. Herrera-Camus R. Bolatto A. D. & Kepley A. 2014, EXTENDED HCN AND HCO+EMISSION IN THE STARBURST GALAXY M82, The Astrophysical Journal, 797 134

Sanders D. B. Mazzarella J. M. Kim D.-C. Surace J. A. & Soifer B. T. 2003, TheIRASRevised Bright Galaxy Sample, The Astronomical Journal, 126

1607–1664

Sanders D. B. & Mirabel I. F. 1996, LUMINOUS INFRARED GALAXIES, Annual Review of Astronomy and Astrophysics, 34 749–792

Sanders D. B. Soifer B. T. Elias J. H. Madore B. F. Matthews K. Neugebauer G. & Scoville N. Z. 1988, Ultraluminous infrared galaxies and the origin of quasars, The Astrophysical Journal, 325 74

Sargent A. I. Sanders D. B. & Phillips T. G. 1989, CO(2-1) emission from the interacting galaxy pair NGC 3256, ApJ, 346 L9–L11

Schmidt M. 1959, The Rate of Star Formation., ApJ, 129 243

Scoville N. Faisst A. Capak P. Kakazu Y. Li G. & Steinhardt C. 2015, DUST ATTENUATION IN HIGH REDSHIFT GALAXIES: "DIAMONDS IN THE SKY", The Astrophysical Journal, 800 108

Scoville N. & Murchikova L. 2013, SUBMILLIMETER RECOMBINATION LINES IN DUST-OBSCURED STARBURSTS AND ACTIVE GALACTIC NUCLEI, The Astrophysical Journal, 779 75

Sekimoto Y. & Lmsa Working Group. 2001, in Astronomical Society of the Pacific Conference Series, Vol. 235 Science with the Atacama Large Millimeter Array ed. A. Wootten, 245

Shaver P. A. McGee R. X. Newton L. M. Danks A. C. & Pottasch S. R. 1983, The galactic abundance gradient, MNRAS, 204 53–112

Sliwa K. Wilson C. D. Iono D. Peck A. & Matsushita S. 2014, Around the Ring We Go: The Cold, Dense Ring of Molecular Gas in NGC 1614, ApJ, 796 L15

Solomon P. & Vanden Bout P. 2005, Molecular Gas at High Redshift, Annual Review of Astronomy and Astrophysics, 43 677–725

Springel V. Di Matteo T. & Hernquist L. 2005, Modelling feedback from stars and black holes in galaxy mergers, Monthly Notices of the Royal Astronomical

Society, 361 776–794

Springel V. & Hernquist L. 2003, Cosmological smoothed particle hydrodynamics simulations: a hybrid multiphase model for star formation, Monthly Notices of the Royal Astronomical Society, 339 289–311

Steinborn L. K. Hirschmann M. Dolag K. Shankar F. Juneau S. Krumpe M. Remus R.-S. & Teklu A. F. 2018, Cosmological simulations of black hole growth II: how (in)significant are merger events for fuelling nuclear activity?, MNRAS, 481 341–360

Stern D. Assef R. J. Benford D. J. Blain A. Cutri R. Dey A. Eisenhardt P. Griffith R. L. Jarrett T. H. Lake S. Masci F. Petty S. Stanford S. A. Tsai C.-W. Wright E. L. Yan L. Harrison F. & Madsen K. 2012, Mid-infrared Selection of Active Galactic Nuclei with the Wide-Field Infrared Survey Explorer. I. Characterizing WISE-selected Active Galactic Nuclei in COSMOS, ApJ, 753 30

Storey P. J. & Hummer D. G. 1995, Recombination line intensities for hydrogenic ions-IV. Total recombination coefficients and machine-readable tables for Z=1 to 8, Monthly Notices of the Royal Astronomical Society, 272 41–48

Tacconi L. J. Neri R. Genzel R. Combes F. Bolatto A. Cooper M. C. Wuyts S. Bournaud F. Burkert A. Comerford J. Cox P. Davis M. Förster Schreiber N. M. García-Burillo S. Gracia-Carpio J. Lutz D. Naab T. Newman S. Omont A. Saintonge A. Shapiro Griffin K. Shapley A. Sternberg A. & Weiner B. 2013, Phibss: Molecular Gas Content and Scaling Relations in z ˜ 1-3 Massive, Main-sequence Star-forming Galaxies, ApJ, 768 74

Tadhunter C. Morganti R. Rose M. Oonk J. B. R. & Oosterloo T. 2014, Jet acceleration of the fast molecular outflows in the Seyfert galaxy IC 5063, Nature, 511 440–443

Takeuchi T. T. Buat V. Heinis S. Giovannoli E. Yuan F.-T. Iglesias-Páramo J. Murata

K. L. & Burgarella D. 2010, Star formation and dust extinction properties of local galaxies from the AKARI-GALEX all-sky surveys . First results from the most secure multiband sample from the far-ultraviolet to the far-infrared, A&A, 514 A4

Tan J. C. 2000, Star Formation Rates in Disk Galaxies and Circumnuclear Starbursts from Cloud Collisions, ApJ, 536 173–184

Teyssier R. Chapon D. & Bournaud F. 2010, THE DRIVING MECHANISM OF STARBURSTS IN GALAXY MERGERS, The Astrophysical Journal, 720 L149–L154

Tielens A. G. G. M. 2005, The Physics and Chemistry of the Interstellar Medium

Toomre A. & Toomre J. 1972, Galactic Bridges and Tails, ApJ, 178 623–666

Torrey P. Cox T. J. Kewley L. & Hernquist L. 2012, The Metallicity Evolution of Interacting Galaxies, ApJ, 746 108

Tosaki T. Kohno K. Harada N. Tanaka K. Egusa F. Izumi T. Takano S. Nakajima T. Taniguchi A. & Tamura Y. 2017, A statistical study of giant molecular clouds traced by ^{13}CO, $C^{18}O$, CS, and CH_3OH in the disk of NGC 1068 based on ALMA observations, PASJ, 69 18

Tsai A.-L. Matsushita S. Kong A. K. H. Matsumoto H. & Kohno K. 2012, First Detection of a Subkiloparsec Scale Molecular Outflow in the Starburst Galaxy NGC 3628, ApJ, 752 38

Tsai A.-L. Matsushita S. Nakanishi K. Kohno K. Kawabe R. Inui T. Matsumoto H. Tsuru T. G. Peck A. B. & Tarchi A. 2009, Molecular Superbubbles and Outflows from the Starburst Galaxy NGC 2146, Publications of the Astronomical Society of Japan, 61 237–250

Ueda J. Iono D. Yun M. S. Crocker A. F. Narayanan D. Komugi S. Espada D. Hatsukade B. Kaneko H. Matsuda Y. Tamura Y. Wilner D. J. Kawabe R. &

Pan H.-A. 2014, Cold Molecular Gas in Merger Remnants. I. Formation of Molecular Gas Disks, ApJS, 214 1

Usero A. Leroy A. K. Walter F. Schruba A. García-Burillo S. Sandstrom K. Bigiel F. Brinks E. Kramer C. Rosolowsky E. Schuster K.-F. & de Blok W. J. G. 2015, Variations in the Star Formation Efficiency of the Dense Molecular Gas across the Disks of Star-forming Galaxies, AJ, 150 115

van der Tak F. F. S. Black J. H. Schöier F. L. Jansen D. J. & van Dishoeck E. F. 2007, A computer program for fast non-LTE analysis of interstellar line spectra. With diagnostic plots to interpret observed line intensity ratios, A&A, 468 627–635

van Dokkum P. G. 2005, The Recent and Continuing Assembly of Field Elliptical Galaxies by Red Mergers, AJ, 130 2647–2665

Veilleux S. Cecil G. & Bland-Hawthorn J. 2005, Galactic Winds, Annual Review of Astronomy and Astrophysics, 43 769–826

Veilleux S. Kim D.-C. & Sanders D. B. 2002, Optical and Near-Infrared Imaging of the IRAS 1 Jy Sample of Ultraluminous Infrared Galaxies. II. The Analysis, ApJS, 143 315–376

Veilleux S. Rupke D. S. N. & Swaters R. 2009, WARM MOLECULAR HYDROGEN IN THE GALACTIC WIND OF M82, The Astrophysical Journal, 700 L149–L153

Vila-Vilaró B. Cepa J. & Butner H. M. 2003, CO (3-2) Observations of Early-Type Galaxies with the Heinrich Hertz Telescope, ApJ, 594 232–246

Violino G. Ellison S. L. Sargent M. Coppin K. E. K. Scudder J. M. Mendel T. J. & Saintonge A. 2018, Galaxy pairs in the SDSS - XIII. The connection between enhanced star formation and molecular gas properties in galaxy mergers, MNRAS, 476 2591–2604

Vorontsov-Velyaminov B. A. 1959, in Atlas and catalog of interacting galaxies

(1959)

Vorontsov-Velyaminov B. A. 1977, Atlas of interacting galaxies, part II and the concept of fragmentation of galaxies., A&AS, 28 1–117

Vorontsov-Velyaminov B. A. Noskova R. I. & Arkhipova V. P. 2001, The catalogue of interacting galaxies by Vorontsov-Velyaminov, Astronomical and Astrophysical Transactions, 20 717–959

Wagner A. Y. Bicknell G. V. Umemura M. Sutherland R. S. & Silk J. 2016, Galaxy-scale AGN feedback - theory, Astronomische Nachrichten, 337 167

Walter F. Bolatto A. D. Leroy A. K. Veilleux S. Warren S. R. Hodge J. Levy R. C. Meier D. S. Ostriker E. C. Ott J. & et al. 2017, Dense Molecular Gas Tracers in the Outflow of the Starburst Galaxy NGC 253, The Astrophysical Journal, 835 265

Walter F. Brinks E. de Blok W. J. G. Bigiel F. Kennicutt R. C. Thornley M. D. & Leroy A. 2008, THINGS: THE H I NEARBY GALAXY SURVEY, The Astronomical Journal, 136 2563–2647

Walter F. Weiss A. & Scoville N. 2002, Molecular Gas in M82: Resolving the Outflow and Streamers, ApJ, 580 L21–L25

Wang Z. Fazio G. G. Ashby M. L. N. Huang J.-S. Pahre M. A. Smith H. A. Willner S. P. Forrest W. J. Pipher J. L. & Surace J. A. 2004, The Off-Nuclear Starbursts in NGC 4038/4039 (The Antennae Galaxies), ApJS, 154 193–198

Weiß A. Walter F. & Scoville N. Z. 2005, The spectral energy distribution of CO lines in M 82, A&A, 438 533–544

White S. D. M. 1978, Simulations of merging galaxies, MNRAS, 184 185–203

Wilson C. D. Petitpas G. R. Iono D. Baker A. J. Peck A. B. Krips M. Warren B. Golding J. Atkinson A. Armus L. Cox T. J. Ho P. Juvela M. Matsushita S. Mihos J. C. Pihlstrom Y. & Yun M. S. 2008, Luminous Infrared Galaxies with

the Submillimeter Array. I. Survey Overview and the Central Gas to Dust Ratio, ApJS, 178 189–224

Wilson C. D. & Scoville N. 1990, The properties of individual giant molecular clouds in M33, ApJ, 363 435–450

Wilson C. D. Warren B. E. Israel F. P. Serjeant S. Attewell D. Bendo G. J. Butner H. M. Chanial P. Clements D. L. Golding J. Heesen V. Irwin J. Leech J. Matthews H. E. Mühle S. Mortier A. M. J. Petitpas G. Sánchez-Gallego J. R. Sinukoff E. Shorten K. Tan B. K. Tilanus R. P. J. Usero A. Vaccari M. Wiegert T. Zhu M. Alexander D. M. Alexander P. Azimlu M. Barmby P. Brar R. Bridge C. Brinks E. Brooks S. Coppin K. Côté S. Côté P. Courteau S. Davies J. Eales S. Fich M. Hudson M. Hughes D. H. Ivison R. J. Knapen J. H. Page M. Parkin T. J. Rigopoulou D. Rosolowsky E. Seaquist E. R. Spekkens K. Tanvir N. van der Hulst J. M. van der Werf P. Vlahakis C. Webb T. M. Weferling B. & White G. J. 2012, The JCMT Nearby Galaxies Legacy Survey - VIII. CO data and the $L_{CO(3–2)}$-L_{FIR} correlation in the SINGS sample, MNRAS, 424 3050–3080

Wright E. L. Eisenhardt P. R. M. Mainzer A. K. Ressler M. E. Cutri R. M. Jarrett T. Kirkpatrick J. D. Padgett D. McMillan R. S. Skrutskie M. Stanford S. A. Cohen M. Walker R. G. Mather J. C. Leisawitz D. Gautier III T. N. McLean I. Benford D. Lonsdale C. J. Blain A. Mendez B. Irace W. R. Duval V. Liu F. Royer D. Heinrichsen I. Howard J. Shannon M. Kendall M. Walsh A. L. Larsen M. Cardon J. G. Schick S. Schwalm M. Abid M. Fabinsky B. Naes L. & Tsai C.-W. 2010, The Wide-field Infrared Survey Explorer (WISE): Mission Description and Initial On-orbit Performance, AJ, 140 1868–1881

Yamamoto T. 1985, Formation environment of cometary nuclei in the primordial solar nebula, A&A, 142 31–36

Yamamura I. Makiuti S. Ikeda N. Fukuda Y. Oyabu S. Koga T. & White G. J.

2010, VizieR Online Data Catalog: AKARI/FIS All-Sky Survey Point Source Catalogues (ISAS/JAXA, 2010), VizieR Online Data Catalog, 2298

Yang C. Gao Y. Omont A. Liu D. Isaak K. G. Downes D. van der Werf P. P. & Lu N. 2013, Water Vapor in nearby Infrared Galaxies as Probed by Herschel, ApJ, 771 L24

Yao L. Seaquist E. R. Kuno N. & Dunne L. 2003, CO Molecular Gas in Infrared-luminous Galaxies, ApJ, 588 771–791

Yun M. S. Reddy N. A. & Condon J. J. 2001, Radio Properties of Infrared-selected Galaxies in the IRAS 2 Jy Sample, ApJ, 554 803–822

Zensus J. A. 1997, PARSEC-SCALE JETS IN EXTRAGALACTIC RADIO SOURCES, Annual Review of Astronomy and Astrophysics, 35 607–636

Zhang Y. Arce H. G. Mardones D. Cabrit S. Dunham M. M. Garay G. Noriega-Crespo A. Offner S. S. R. Raga A. C. & Corder S. A. 2016, ALMA Cycle 1 Observations of the HH46/47 Molecular Outflow: Structure, Entrainment, and Core Impact, ApJ, 832 158

Ziurys L. M. Friberg P. & Irvine W. M. 1989, Interstellar SiO as a tracer of high-temperature chemistry, ApJ, 343 201–207

Zschaechner L. K. Walter F. Bolatto A. Farina E. P. Kruijssen J. M. D. Leroy A. Meier D. S. Ott J. & Veilleux S. 2016, The Molecular Wind in the Nearest Seyfert Galaxy Circinus Revealed by ALMA, ApJ, 832 142

Zubovas K. & Bourne M. A. 2017, Do AGN outflows quench or enhance star formation?, MNRAS, 468 4956–4967

Zubovas K. & Nayakshin S. 2014, Energy- and momentum-conserving AGN feedback outflows, MNRAS, 440 2625–2635

Zwicky F. Herzog E. & Wild P. 1968, Catalogue of galaxies and of clusters of galaxies